

Nanostructured back reflectors for improved light absorption in silicon thin film solar cells

Li, Zeyu

2018

Li, Z. (2018). Nanostructured back reflectors for improved light absorption in silicon thin film solar cells. Doctoral thesis, Nanyang Technological University, Singapore.

<https://hdl.handle.net/10356/83958>

<https://doi.org/10.32657/10220/46662>

**NANOSTRUCTURED BACK REFLECTORS FOR
IMPROVED LIGHT ABSORPTION IN SILICON THIN
FILM SOLAR CELLS**

LI ZEYU

**SCHOOL OF ELECTRICAL AND ELECTRONIC
ENGINEERING**

A thesis submitted to the Nanyang Technological University
in partial fulfilment of the requirement for the degree of
Doctor of Philosophy

2018

Acknowledgements

I would like to thank my supervisor, Assoc. Prof. Rusli, for offering me an opportunity to pursue a Ph.D degree in the field of solar cell. I have been extremely lucky to have a supervisor who cared so much about my research work and my life, and who provided strong support, valuable guidance and prompt feedback throughout my research period even when he has a tight schedule. His scientific and ethical standards encourage me to develop myself to be a better researcher and a better person.

I would like to thank my co-supervisor Prof. Pere Roca i Cabarrocas, for guiding my research work during the one-year period in LPICM, France. His immense knowledge, enthusiasm, motivation, and special humors during daily work have shaped my fruitful and fantastic research experience in LPICM. His guidance helped me in all time of research and writing of the thesis. I could not have imagined having a better advisor and mentor for my Ph.D study.

I would like to express my gratitude to Dr. Martin Foldyna for his guidance and knowledge in silicon thin film modelling topic. I would like to express my gratitude to Dr. Wanghua Chen and Dr. Junkang Wang for the sharing of their knowledge in silicon thin film manufacturing and characterizing techniques. I am also grateful to Dr. Pavel Bulkin and Dr. Rasha for their help with the oxygen plasma system.

Furthermore, I would like to thank the support provided by NTU Clean Room and Characterization Laboratory technicians, specifically Mr. M. Shamsul, Mr. Mak Foo Wah, Ms. Seet Lye Ping, Ms. Ngo Ling Ling, Ms. Yang Xiaohong and Mr. M. Fauzi. I would also like to thank the support provided by LPICM support teams, specifically Ms. Jaqueline Tran and Mr. Jerome Charliac.

I would also want to thank our group post-doc Dr. Wang Jianxiong, Dr. Ari Bimo Prakoso, and my group mates Dr. Alienor Togonal, Dr. Wang Hao, and Mr. Lu Chenjin for their kind support and discussions about my research project.

Last but not least, I would like to give my special appreciation to my family and my friends, from whom I received a lot of love, patience, understanding, and encouragement through my studies.

Abstract

The study on photovoltaic is an important topic in the sustainable and clean energy research field, driven by the deteriorating energy crisis and environmental pollutions due to fossil fuel shortage and combustion. Currently, crystalline silicon (c-Si) based solar cell dominates the photovoltaic market. However, its high material cost has weakened its competitiveness against fossil fuels. To reduce the material cost, silicon thin film based solar cell that uses less material is favourable. However, this will result in reduced optical absorption and consequently lower cell efficiency. To address the issue, nanostructures can be incorporated into the thin film solar cell for light trapping and to improve the optical absorption.

In this work, we study nanostructured back reflector (BR) for improved light absorption in hydrogenated amorphous silicon thin film solar cells. The nanostructured BRs are patterned and fabricated based on polystyrene sphere (PS) assisted lithography. We adopt “substrate” (n-i-p) structure and highly reflective Ag layer and optical spacer ZnO layer are deposited on glass substrate as the BR materials. The hydrogenated amorphous silicon thin films are grown on top of the BRs by the plasma enhanced chemical vapor deposition (PECVD) technique.

To improve the patterning capability and develop a well-controlled fabrication process for the BRs, we study the etching behavior of PS spheres in electron cyclotron resonance (ECR) oxygen plasma. By tuning the oxygen plasma

condition including plasma input power, etching mode, shielding of the ion flux with Faraday cage, we successfully isolated the effects of oxygen radical and of energetic ions on the etching behaviors of PS spheres. The reasons behind PS spheres melting and shape deformations are identified, and negative impacts during BR fabrication are avoided. As a result, we developed a well-controlled oxygen plasma etching process for PS spheres using the ECR plasma source. After etching, smaller PS sphere sizes are achieved, which enables us to control the dimensions of the nanostructures formed using the PS assisted lithography.

After that, we study light trapping in hydrogenated amorphous silicon thin film solar cells fabricated by the PECVD technique on various nanostructured BRs. The BRs are patterned using different PS sphere sizes without oxygen plasma etching step. We have investigated the correlation between the optical properties of the BRs and the performance of the corresponding fabricated solar cells. We have also introduced a mixture of two different sizes of PS spheres patterned BRs, and have obtained solid experimental evidence of improved light trapping performance of such BRs, as compared with those patterned using single size polystyrene spheres. Overall, we have achieved high performing nanostructured amorphous silicon solar cells with an initial power conversion efficiency of 8.79 %, and over 20 % enhancement of the short-circuit current compared with the reference flat BR solar cell without the nanostructures.

Due to the usage of Ag and ZnO material and Ag nanostructures in the BRs for light scattering and absorption enhancement, parasitic losses are also inevitably introduced in the device. In this thesis, we also study in detail through optical modelling, the parasitic losses and light trapping in hydrogenated amorphous silicon thin film solar cells fabricated by the PECVD technique on nanostructured BRs. The BRs are patterned using single PS sphere size with oxygen plasma etching step to reduce and control the dimension of the PS spheres. By using O₂ plasma etching of the PS spheres, we fabricated hexagonal nanostructured BRs. With the help of rigorous modeling, we study the parasitic losses in different BRs, in the non-active layers, and the light enhancement effect in the silicon absorber layer. Moreover, the simulation results have been compared and verified with experimental data. We have demonstrated hexagonal nanostructured amorphous silicon thin film solar cells with a power conversion efficiency of 7.7 % and around 34.7 % enhancement of the short-circuit current density, compared with flat amorphous silicon thin film solar cell.

In summary, nanostructured silicon thin film solar cells are fabricated, characterized and simulated. The etching behavior of polystyrene (PS) spheres under electron cyclotron resonance (ECR) generated oxygen plasmas are studied. Various nanostructured Ag/ZnO back reflectors (BRs) patterned by single or double PS sphere sizes are fabricated and their optical performance are characterized and correlated with the corresponding solar cell performance. Hexagonal nanostructured Ag/ZnO back reflectors and their corresponding nanostructured silicon thin film solar cells are simulated and

verified against experimental results. The parasitic losses in the device are investigated.

Table of Content

Acknowledgements	1
Abstract	3
Table of Content	7
List of figures and tables.....	10
Chapter 1. Introduction	13
1.1 Background and motivation	13
1.2 Objective	17
1.3 Major contributions of the thesis.....	18
1.4 Organization of the thesis.....	19
Chapter 2. Literature Review	21
2.1 Solar cell fundamentals	21
2.1.1 Solar cell operation principle	21
2.1.2 Solar cell electrical model, figure of merit and characterization techniques.....	23
2.2 Silicon, organic, organic/silicon hybrid and silicon thin film solar cells.....	30
2.2.1 Silicon solar cells.....	30
2.2.2 Organic solar cells.....	36
2.2.3 Organic/silicon hybrid solar cells	39
2.2.4 Silicon thin film solar cells	43
2.3 Nano-structuring techniques	45
2.4 Solar cell simulation methodologies	47
Chapter 3. Improved Polystyrene Sphere Assisted Lithography with Matrix Distributed Electron Cyclotron Resonance Oxygen Plasma	51
3.1 Introduction and objectives.....	52
3.1.1 PS sphere assisted lithography and its applications	52
3.1.2 Electron cyclotron resonance plasma	56
3.2 Fabrication process and conditions	60
3.2.1 PS sphere monolayer formation.....	60
3.2.2 Reactive ion etching by matrix distributed electron cyclotron resonance generated oxygen plasma	62
3.2.3 Patterning quality evaluation and PS sphere melting	65
3.3 Effect of etching conditions	67
3.3.1 Effect of etching power.....	67
3.3.2 Effect of etching mode	68

3.3.3 Effect of Faraday cage shielding	71
3.3.4 Effect of etching gas.....	78
3.4 Shape Evolution of PS Spheres	79
3.5 Conclusion	88
Chapter 4. Nanostructured Back Reflectors produced using Polystyrene Assisted Lithography for Enhanced Light Trapping in Silicon Thin Film Solar Cells	90
4.1 Introduction and objectives.....	91
4.1.1 Front scatterer and back reflector for silicon thin film solar cell.....	92
4.1.2 Nanostructured Ag/ZnO back reflector.....	94
4.2 Fabrication and characterization of nanostructured Ag/ZnO back reflectors and back reflector solar cells	96
4.2.1 PS sphere patterned back reflector.....	96
4.2.2 Silicon thin film solar cell	98
4.2.3 Characterization techniques.....	99
4.3 Optical characterization of PS sphere patterned back reflectors.....	100
4.3.1 Single sphere size patterned back reflector	102
4.3.2 Double sphere size patterned back reflector.....	104
4.4 PS sphere patterned back reflector solar cells performance	108
4.4.1 Single size PS sphere patterned back reflector solar cells.....	108
4.4.2 Double size PS sphere patterned back reflector solar cells	114
4.5 Conclusion	117
Chapter 5. Optical Study and Experimental Realization of Nanostructured Back Reflectors for Enhanced Light Trapping with Reduced Parasitic Losses in Silicon Thin Film Solar Cells	118
5.1 Introduction and objectives.....	119
5.2 Fabrication of hexagonal nanostructured Ag/ZnO back reflectors and back reflector solar cells.....	122
5.2.1 Hexagonal nanostructured Ag/ZnO back reflector	122
5.2.2 Silicon thin film solar cell	123
5.3 Optical characterization of flat and ASahi back reflectors	126
5.3.1 Total reflectance from flat and ASahi back reflectors.....	126
5.3.2 Bruggeman effective medium approximation simulation	130
5.4 Experiment and simulation results on hexagonal Ag/ZnO nanostructured back reflectors.....	135
5.4.1 Total and diffused reflectance of hexagonal Ag/ZnO nanostructured back reflectors.....	137

5.4.2 Simulated absorption of hexagonal Ag/ZnO nanostructured back reflectors	139
5.5 Experiments and simulation results of hexagonal Ag/ZnO back reflector solar cells	142
5.5.1 Parasitic losses and absorption enhancement analysis	144
5.5.2 Experiment results	148
5.6 Conclusion	151
Chapter 6. Conclusion and future works.....	153
6.1 Conclusion	153
6.2 Recommendation for future research	155
6.2.1 Fabrication of nanostructured microcrystalline silicon thin film solar cell	155
6.2.2 Fabrication of $\mu\text{c-Si:H/a-Si:H}$ tandem silicon thin film solar cell based on PS sphere assisted lithography	156
6.2.3 Simulation optimization of the silicon thin film solar cell for the best performing fabrication parameter	157
6.2.4 Nano-structuring technique by top down etching of silicon material.....	157
Reference	159
Author's publications	177

List of Figures and Tables

Figure 1.1: Solar PV generation capacity from 2007 to 2016 [1]	12
Figure 2.2: Photo-generation of carriers in solar cell resulting in current flow [2].	21
Figure 2.3: Solar cell equivalent circuit with R_s and R_{sh} [27]..	22
Figure 2.4: A typical J-V curve of a solar cell under illumination and several figures of merit.....	24
Figure 2.5: The effect of non-negligible R_s and R_{sh}	26
Figure 2.6: Schematic of standard solar cell performance measurement setup with standard illumination and temperature [27].	26
Figure 2.7: A typical monocrystalline and polycrystalline silicon solar cell, and simplified cross-section of a commercial monocrystalline silicon solar cell [28].	29
Figure 2.8: A typical PERL (left) and PERT (right) solar cell schematic [34].	30
Figure 2.9: A typical structure of n-type Si HIT solar cell [31].	31
Figure 2.10: IBC and HJ-IBC solar cells	32
Figure 2.11: Energy band diagram of a bulk heterojunction single junction organic solar cell.....	34
Figure 2.12: Different categories of OPV based on their structures [39].....	35
Figure 2.13: Bottom illuminated OPVs with (a) conventional device structure and (b) inverted device structure [42].	36
Figure 2.14: Chemical structures of PEDOT and PSS.	38
Figure 2.15: Device structure of a planar Si/PEDOT:PSS heterojunction hybrid solar cell.	39
Figure 2.16: The energy band diagrams of differently terminated silicon surface in contact with PEDOT:PSS layer [68].	40
Figure 2.17: Schematic sketch of a typical p-i-n thin-film silicon solar cell.....	41
Figure 2.18: Divided finite elements in 2D and 3D structures.	46
Figure 2.19: HFSS design flow chart.	47
Figure 3.1: PS assisted lithography process [22].	50
Figure 3.2: Schematic diagram of the fabrication process with top view (upper) and cross-sectional view (lower).....	51
Figure 3.3: (a) The circular or helical motion of an electron in a static and uniform magnetic field. (b) Continuous ac acceleration of the electron in a superimposed magnetic field and electric field.	55
Figure 3.4 (a) Schematic of an elementary plasma excitation unit [164]. (b) Cross-sectional view of a typical MDECR reactor [166].	56
Figure 3.5: Schematic of PS spheres monolayer formation on silicon.....	60
Figure 3.6: Validation of patterning capability of PS sphere arrays after oxygen plasma etching.	62
Figure 3.7: PS sphere melting with (a) $>90^\circ$ contact angle (b) $<90^\circ$ contact angle.....	63
Figure 3.8: SEM images of 600 nm PS spheres etched in a continuous plasma.....	64

Figure 3.9: SEM images of 600 nm PS spheres etched by cycling plasma.	66
Figure 3.10: SEM images of 800 nm PS spheres exposed to oxygen plasma for 2 min 45 sec under 1 kW plasma	67
Figure 3.11: SEM images of 400 nm PS spheres etched for 2 min under 1 kW continuous plasma.....	69
Figure 3.12: SEM images of 600 nm PS spheres etched for 3 min under 1 kW continuous plasma.....	70
Figure 3.13: SEM images of 600 nm PS spheres etched under 500 W continuous plasma.....	72
Figure 3.14: SEM cross section of 400 nm PS spheres etched inside metal cage.....	74
Figure 3.15: SEM images of 600 nm PS spheres etched for 5 min under 500 W continuous plasma inside metal cage.	76
Figure 3.16: Aspect ratio between largest and smallest width observed on top view SEM images as a function of oxygen plasma (500 W) etching time.....	77
Figure 3.17: Aspect ratio between largest and smallest width observed by top view SEM images as a function of PS sphere etched area in percentage under 500 W plasma.	78
Figure 3.18: SEM images of 600 nm PS spheres etched for 5 min under 500 W continuous plasma inside metal cage.	79
Figure 3.19: Top view SEM images of 800 nm PS spheres etched for 5 min 15 sec under cycling 500 W plasma.	79
Figure 3.20: SEM images of 800 nm PS spheres etched under cycling 500 W plasma.....	80
Figure 3.21: Cross section SEM image of 600 nm PS spheres etched for 3 min under cycling 500 W plasma power.	81
Figure 4.1: (a) Fabrication process for Ag nanostructure on glass. (b) Fabrication process for back reflectors.....	91
Figure 4.2: SEM image and schematic image of the cross section of a solar cell device.....	92
Figure 4.3: SEM images of 400, 600 and 800 Polystyrene Spheres assisted Patterned BRs.	94
Figure 4.4: (a) Total and diffused reflectance and (b) reflectance HAZE results of 400, 600 and 800PSP BRs.....	95
Figure 4.5: SEM images of double PS sphere monolayers and 4655 PSP BR	99
Figure 4.6: Diffused and total reflectance results of various double size PSP BRs.....	100
Figure 4.7: J-V, EQE and 1-R _{total} of flat, 400, 600 and 800 PSP BR solar cells.	103
Figure 4.8: J-V and 1-R _{total} results of flat, ASAHI and 800PSP BR solar cells.....	107
Figure 4.9: J-V, EQE and 1-R _{total} of 4891, 6855 and 4655 PSP BR solar cells.	109
Figure 4.10: J-V and 1-R _{total} , EQE results of 400, 600 PSP and 4655 PSP BR solar cells.....	110

Figure 5.1: (a) Fabrication process and (b) top view SEM images of hexagonal back reflectors (pitch = 607 nm) taken after the process steps shown in Fig.5.1(a).....	115
Figure 5.2: (a) Top view SEM image, taken after full device fabrication, and (b) schematic cross section of a hexagonal back reflector solar cell.	117
Figure 5.3: Total reflectance measured on a glass substrate coated with 200 nm Ag and various thicknesses of ZnO (0 – 160 nm).....	119
Figure 5.4: Total reflectance measured on ASAHI substrate coated with 200 nm Ag and with 0, 50 and 100 nm of ZnO.	121
Figure 5.5: (a) Bruggeman effective medium approximation model applied for the Ag/ZnO BR study; (b) & (c) Simulated total reflectance of 50 and 100 nm ZnO (layer 1) with 0 to 30 nm of Ag/ZnO interface (layer 2) thickness.	124
Figure 5.6: SEM images of hexagonal Ag/ZnO back reflectors obtained with 0, 60, 90 and 120 s of O ₂ plasma treatment of polystyrene spheres.....	128
Figure 5.7: (a) Total and (b) diffused reflectance of hexagonal Ag/ZnO BRs and ASAHI BR with 100 nm ZnO.....	129
Figure 5.8: Simulated hexagonal nanostructured back reflector, (a) HFSS unit cell in the simulation model and (b) corresponding cross sectional view.	131
Figure 5.9: (a) 0 sec etched BR measured absorption (top) compared with simulated absorption under 595 nm opening (D=595 nm) simulation condition. (b) 120 sec etched BR measured absorption (top) compared with simulated absorption under 400 nm opening (D=400 nm) simulation condition.....	132
Figure 5.10: (a) HFSS simulation model for hexagonal BR solar cell; (b) Simulated and measured absorption of the flat Ag/ZnO BR solar cell.	135
Figure 5.11: (a) ITO absorption; (b) p layer absorption; (c) n layer absorption; (d) Ag/ZnO BR absorption.	136
Figure 5.12: (a) Simulated intrinsic amorphous silicon absorption; (b) E field distribution of nanostructured and flat solar cell at 670 nm.....	137
Figure 5.13: (a) J-V and solar cell parameters of different solar cells; (b) EQE and absorption (1 – R _{total}) of flat and nanostructured Ag/ZnO BR solar cells.	139
Table 4.1: Photovoltaic parameters for various BR solar cells.....	101

Chapter 1. Introduction

1.1 Background and motivation

Ever since the taking off of industrial revolution from year 1840 onwards, enormous large quantities of fossil fuels have been used to power the economy growth and human society advancement. However, as a result of burning the fossil, large amounts of carbon dioxide are produced and emitted into the earth's atmosphere, which is recognised as the root cause of global warming and leads to disastrous outcomes including climate change and so on [1]. Moreover, it was predicted that at the current consumption rate, crude oil reserves might be depleted by the end of 21st century, natural gas and coal might be depleted by the end of 22nd century [2]–[4]. Due to above situations, the need for a clean and renewable energy source is one of the biggest problems that mankind is facing. Among all renewable energy sources, photovoltaic (PV) is widely accepted as the safest, cleanest and most sustainable energy, as solar radiation power that reaches the earth is so abundant and the sun will remain fairly stable for 4 billion years [5].

As the second most abundant element on earth, crystalline Silicon (c-Si) based solar cells, invented in 1954 [6], was industrially commercialized in large scale in the 1990s. The installation of solar panels in private houses or public facilities has been significantly boosted in the last 20 years [7]. c-Si based solar cells have reached its industrial maturity and the PV market, 90 %

of which is based on c-Si solar cells, is growing rapidly at an annual rate of 35-40%, with PV installation around 98 GW in 2017 [8].

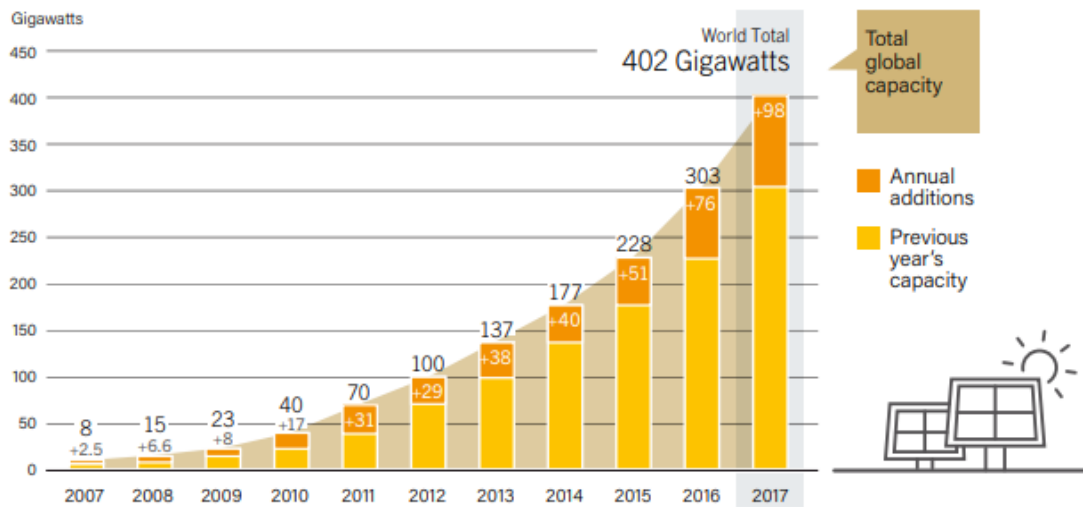


Figure 1.1: Solar PV global capacity and annual additions from 2007 to 2017 [9].

Figure 1.1 shows the rapid growth of PV industry for the past decade [9]. Concurrently, the performance of solar cells has also improved over the years. On 25 August 2017, Kaneka Corporation announced that it had achieved a conversion efficiency of 26.63% (cell area: 180 cm²) with its heterojunction back contact (HJ-IBC) solar cells [10], which marked the current world's highest energy conversion efficiency for c-Si based solar cells [11].

Despite all the merits of solar energy and c-Si based solar cells, solar energy contribution to global electricity production still remains rather low at 1.5% [12]. Its high material and process cost are some of the most critical obstacles that need to be addressed, to achieve lower PV Module Price per Watt and higher market share. In terms of material cost, silicon thin film solar cells are preferred due to their low material usage, contributing to just 2% as compared

to 50% of bulk solar cell module cost [13]. Silicon thin film solar cells fabricated by low temperature plasma enhanced chemical vapor deposition (PECVD) are one of the best candidates, due to their merits, including lesser material usage, compatible with roll-to-roll processes on flexible substrates, robustness in controlling the device shape and material properties, etc. Since the early 1980s, continuous roll-to-roll manufacturing technology for the production of a-Si:H solar cells has been developed and commercialized. In recent years, multi junction a-Si:H solar cells can be manufactured simultaneously on six coils of 130 μm thick, 0.36 m wide, 2.6 km long stainless-steel substrate at 1 cm/s, leading to a 30 MW per year machine productivity [14]. Hyet Solar seeks production capacity expansion in India with a capacity of over 200 MW solar power plant was reported recently as well.

Compared to other thin film solar cell technologies which rely on less abundant and in some cases toxic materials, such as CdS, silicon thin film technologies are preferred from the perspective of a sustainable industrial development and an environmental friendly solar energy conversion process. There are two forms of thin film silicon solar cells: hydrogenated amorphous silicon solar cells (a-Si:H) and hydrogenated microcrystalline silicon solar cells ($\mu\text{c-Si:H}$). However, as an indirect band gap material, to achieve an efficient light absorption, silicon solar cells require at least 200 μm in active silicon thickness. Moreover, due to the short free carrier diffusion length of a-Si:H and $\mu\text{c-Si:H}$ materials, the thickness of silicon thin film is limited to only a few hundreds of nanometers for a-Si:H and a few micrometers for $\mu\text{c-Si:H}$ solar cells. To improve the performance, effective light trapping mechanisms were

extensively researched during the last decade [15], [16]. Various nanostructures applied to silicon thin film solar cells have produced strong localized light resonance modes and increased optical paths, which contributed to the improved light absorption hence photocurrent generation [17], [18]. Depending on the location of the nanostructure with respect to incident light, the most typical classes of nanostructured solar cells use front scatterers or back reflectors (BRs) [19]. Aiming at its best performance, a typical front scatterer utilizes metallic nanostructures, which induce a plasmonic near field enhancement effect [20]. In contrast, a typical BR utilizes metallic or metal/dielectric nanostructures, which produce a far field scattering effect [21].

Polystyrene (PS) sphere assisted lithography, which is also known as one of the colloidal lithography or natural lithography techniques [22], [23], is a promising cost-effective fabrication tool for producing regular and homogenous arrays of nanostructures with different sizes [24]. This technique is not as precise as standard photolithography techniques, such as deep Ultra-Violet (UV) or extreme UV lithography [25], [26]. However, it allows one to fabricate periodic nanostructures, which are regulated up to a few hundreds of micrometers, with a much lower cost and simpler process steps. PS sphere assisted lithography can be used for BRs fabrication as demonstrated by previous studies [27].

1.2 Objective

In this thesis, silicon thin film solar cells produced by PECVD have been deposited on nanostructured BRs. The scope of this research work includes the design, fabrication, simulation, and characterization of silicon thin film solar cells with various nanostructures. The objectives of this study are summarized as follows:

- i. Investigate the oxygen plasma etching behavior of PS sphere arrays in an electron cyclotron resonance (ECR) plasma source. By using different etching conditions, the roles of oxygen radicals and oxygen ions during oxygen plasma etching of the PS spheres are isolated. The root causes of the melting of the PS spheres are studied. Optimized oxygen plasma etching conditions for an improved PS sphere assisted lithography patterning capability in ECR plasma is investigated and developed.
- ii. Fabricate and characterize optical properties of nanostructured Ag/ZnO BRs patterned using single size PS sphere arrays and double size PS sphere arrays. Fabricate and characterize nanostructured silicon thin film solar cells using different BRs. Investigate the correlation between the BR patterning features and the corresponding solar cell performance to achieve best light trapping performance.
- iii. Fabricate and characterize optical properties of hexagonal nanostructured Ag/ZnO BRs with different oxygen plasma etching times. Simulate the hexagonal nanostructured BR and the corresponding solar cells to

investigate the parasitic losses in the device. Fabricate and characterize the optical properties of the hexagonal nanostructured BR solar cell. Verify and cross compare between simulation and experimental results.

1.3 Major contributions of the thesis

- i. We studied the etching behavior of PS sphere arrays in ECR generated oxygen plasmas. By using fine-tuned plasma conditions, we found that PS sphere melting behavior is dominated by energetic ion bombardment and PS sphere material removal, i.e. etching, is dominated by reactive oxygen radicals. By using cycling plasma etching mode, we successfully etched the PS spheres to less than 10% of their initial diameter, while avoiding melting of the spheres, hence retaining their patterning capability. This enables many other applications like point contact solar cells, which require dimensions of less than 100 nm.
- ii. We studied the light trapping performance of silicon thin film solar cells deposited on different nanostructured Ag/ZnO BRs. We found that nanostructured BRs patterned using mixtures of two PS spheres can effectively improve the light scattering properties, as compared to single PS spheres patterned BRs. As a result, silicon thin film solar cells deposited on 400 and 600 nm PS spheres mixture patterned nanostructured BRs have achieved an initial power conversion efficiency of 8.79 % and over 20 % enhancement of the short-circuit current as compared to the reference flat solar cell.

- iii. We also studied the parasitic losses of the hexagonal nanostructured Ag/ZnO BRs. By using Bruggeman Effective Medium Approximation, we found that absorption at rough Ag/ZnO interfaces is the main reason for optical losses in BRs. By using electromagnetic simulation, we further identified that ZnO absorption enhanced by the Ag nanostructures contributes mostly to the parasitic losses of hexagonal BRs. We also simulated the performance of the solar cells and verified with the experimental results. A good agreement was found between simulation and experimental performance.

1.4 Organization of the thesis

This thesis consists of six chapters and is organized as follows:

Chapter 1: Background, motivation, objectives and major contributions of the thesis are presented.

Chapter 2: The fundamental principles of solar cell operation are presented. A literature review on commercial silicon solar cells, organic solar cells, organic/silicon hybrid solar cells and silicon thin film solar cell is presented.

Chapter 3: The etching behavior of PS sphere arrays in oxygen plasmas generated by ECR source is presented. The effect of the etching power, etching mode (continuous or cycling), Faraday cage shielding and etching

gases are studied. The roles of oxygen radicals and ions during PS sphere etching are isolated and presented.

Chapter 4: The study on light trapping performance in hydrogenated amorphous silicon thin film solar cells fabricated by PECVD on various PS sphere assisted lithography patterned nanostructured BRs is presented. The optical performances of different BRs are correlated with their corresponding solar cell device performance.

Chapter 5: The study on parasitic losses of hexagonal nanostructured BRs and the corresponding solar cell devices are presented. Bruggeman effective medium approximation (BEMA) simulation results, as well as rigorous finite element method (FEM) based electromagnetic field simulation results are presented. Comparison and verification between the simulation and experimental results are carried out. Light resonances modes and light trapping effects are analyzed and presented.

Chapter 6: A general summary of the work done and recommendations for future work are presented.

Chapter 2. Literature Review

This chapter reviews the literature on solar cell fundamentals, recent developments of different categories of solar cells, nano-structuring techniques for light trapping, and last but not least, simulation studies for solar cell light absorption enhancement. The chapter starts by introducing solar cell operation principle, solar cell electrical model, figures of merit and device characterization techniques. Subsequently, various categories including commercial high efficiency mono/multi-crystalline silicon solar cells, organic solar cells, organic/silicon hybrid solar cells and silicon thin film solar cells are presented in terms of the state of the art device fabrication processes, operation physics, and their corresponding strengths and weaknesses. After that, we present different nano-structuring techniques and the devices performance improvement resulting from nanostructures incorporated into the solar cell. Reports on simulation studies and investigation of different light absorption mechanisms are summarized in the last part of this chapter.

2.1 Fundamental of solar cell

2.1.1 Solar cell operation principle

A photovoltaic device or solar cell is a semiconductor device which generates electrical energy directly from solar energy by the photovoltaic effect. Figure 2.1 shows a schematic of a solar cell under illumination. When photons are incident on the semiconductor through the gaps between the top metal

contact, those with energy greater than the bandgap of the semiconductor will be absorbed to excite electrons from their chemical bonds, resulting in the formation of electron-hole pairs. Those excited electrons and holes will be temporarily mobile and can move freely in the semiconductor's conduction band and valence band respectively. Due to the diffusion induced internal built-in electric field near the interface of the p-n junction, electron/hole pairs are separated and move in opposite directions towards the top and bottom metal electrodes, resulting in electric current [13].

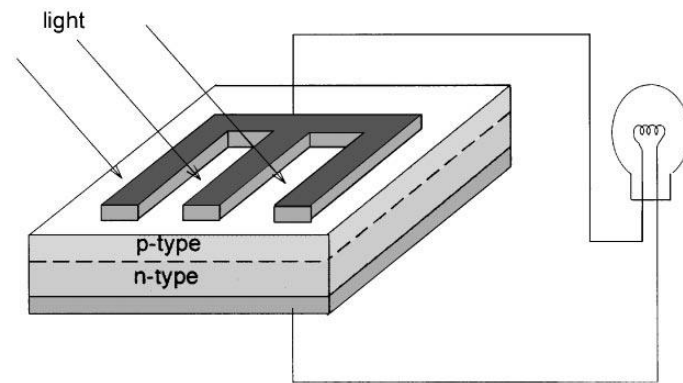


Figure 2.1: A schematic of a solar cell under illumination [1].

The p-n junction is the most basic cornerstone for photovoltaic effect. As shown in Fig. 2.2, when n-type and p-type semiconductors are put together, the Fermi levels in both semiconductors are aligned under no electric field applied, resulting in a built-in electric field developed over the depletion region. Thermal equilibrium is achieved due to the balance between excess carriers' diffusion and carriers drift driven by the internal built-in electric field. When light is incident on the cell, photons with energy greater than the band gap of the material will excite electrons from the valence band to the conduction band, leading to the generation of electron-hole pairs. The internal

built-in electric field will separate the electrons and holes, resulting in drift in opposite directions, and hence giving rise to an electric current [28].

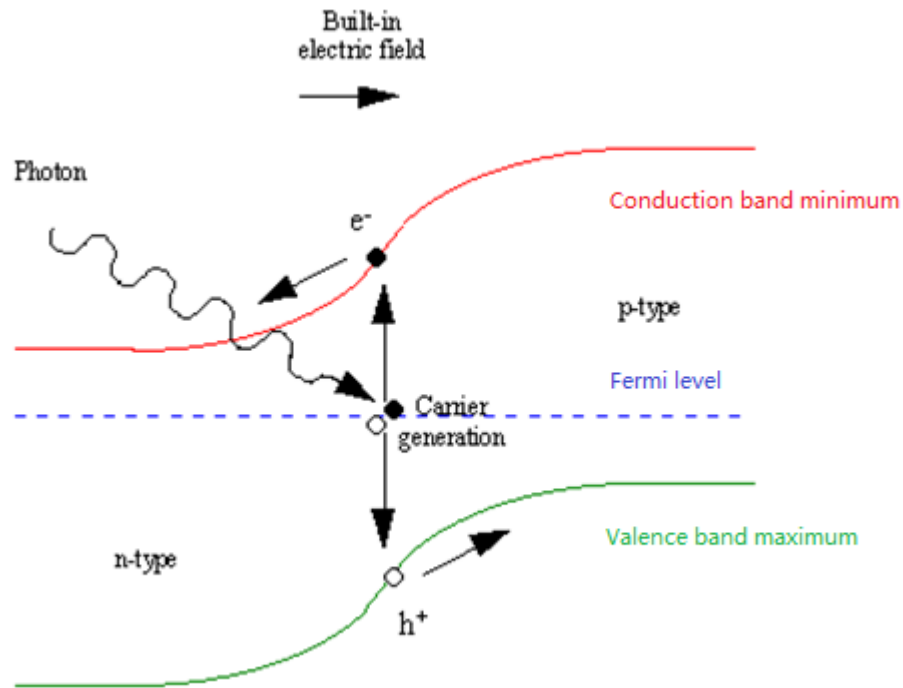


Figure 2.2: Photo-generation of carriers in solar cell resulting in current flow [2].

2.1.2 Solar cell electrical model, figure of merit and characterization techniques

To model a solar cell electrically, we discuss the current density-voltage (J - V) characteristic of a solar cell in the dark. Without any light, the characteristic of a solar cell is similar to a p-n junction, i.e. a diode. Under forward bias, it experiences an exponential increase in current with voltage, while under reverse bias, only a small amount of current flows. The J - V characteristics of the solar cell in the dark can be described by the diode equation:

$$J(V) = J_0 \left(e^{\frac{qV}{nkT}} - 1 \right) \quad (2.1)$$

where J_0 is the saturation current density, q is the elementary charge, n is the diode ideality factor, k the Boltzmann constant and T the temperature in Kelvin.

When the solar cell is exposed to light, the photo-generated current density J_L flows in opposed direction to the forward bias direction, leading to the illuminated J - V characteristic,

$$J(V) = J_0 \left(e^{\frac{qV}{nkT}} - 1 \right) - J_L \quad (2.2)$$

The power generated at each operating point on the J - V curve can be calculated as follows,

$$P(V) = J(V) \times V = \left(J_0 \left(e^{\frac{qV}{nkT}} - 1 \right) - J_L \right) V \quad (2.3)$$

To include parasitic resistance for a more realistic solar cell model, a solar cell equivalent circuit with series and shunt resistances is shown in Fig. 2.3 [29].

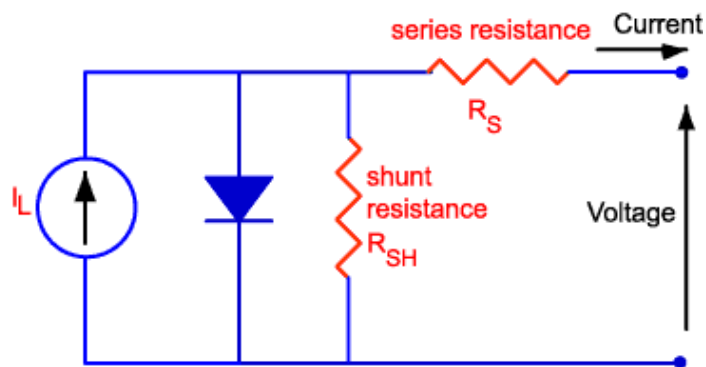


Figure 2.3: Solar cell equivalent circuit with R_s and R_{sh} [30].

A constant current source component with value J_L represents the photocurrent density generated by light absorption and charge separation at the p-n junction. Since both series and shunt resistances contribute to the light conversion efficiency reduction by power dissipation through heat, the J - V characteristic can be described by a more general formula as follows,

$$J(V)A = J_L A - J_0 A \left(e^{\frac{q(V - J(V)AR_s)}{nkT}} - 1 \right) - \frac{V - J(V)AR_s}{R_{sh}} \quad (2.4)$$

where A is the solar cell area. The series resistance R_s comes from different sources: i) resistance from the semiconductor bulk material, ii) resistance between the semiconductor bulk material and external metal contacts, and iii) resistance of the metal contact itself. The shunt resistance R_{sh} typically comes from the leakage current of the device, including defects or pin holes.

To characterize the effect of series or shunt resistance on the solar cell device performance, we first characterize the J - V curve of a solar cell and introduce several figures of merit. Fig.2.4 shows a schematic of typical J - V curve under illumination and several figures of merit for a solar cell, which are the short circuit current density J_{sc} , open circuit voltage V_{oc} , fill factor FF and power conversion efficiency (PCE).

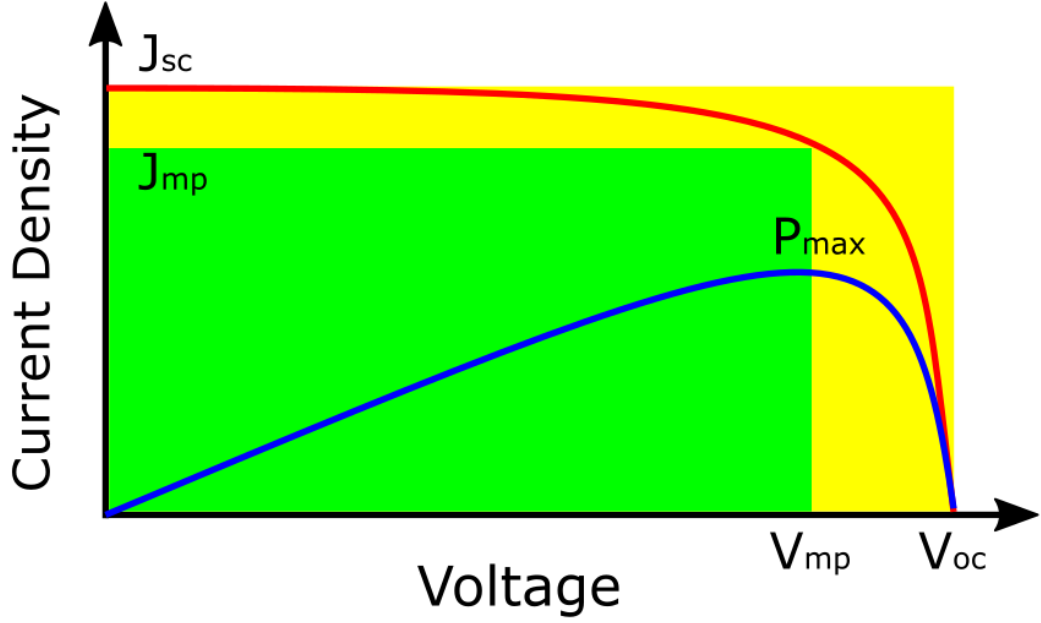


Figure 2.4: A typical J - V curve of a solar cell under illumination and several figures of merit.

Short circuit current J_{sc} is the maximum current that can be extracted from the solar cell when it is short circuited. It is given by,

$$J_{sc} = q \int (P(E)\eta(EQE))\delta E \quad (2.5)$$

where $P(E)$ is the spectral irradiance of the light source, typically the standard AM1.5G solar spectrum. $\eta(EQE)$ is the external quantum efficiency, which is the ratio of the number of charge carriers collected by the solar cell to the number of incident photons at a given incident photon energy E . Essentially J_{sc} depends on the number of photo-generated carriers that can be collected by the junction. When there is no current flow through the device, the corresponding voltage is the open circuit voltage V_{oc} . Based on equation (2.2), the relationship between J_{sc} and V_{oc} can be described as follows,

$$V_{oc} = \frac{nkT}{q} \ln \left(\frac{J_{sc}}{J_0} + 1 \right) \quad (2.6)$$

As the illuminated J - V curve is not squarish, the maximum power P_{max} that solar cell generates will always be less than the product of V_{oc} and J_{sc} . The ratio of P_{max} to $V_{oc} \times J_{sc}$ is called the fill factor FF, which describes the squareness of the J - V curve:

$$FF = \frac{P_{max}}{V_{oc} \times J_{sc}} \quad (2.7)$$

The most important parameter that characterizes a solar cell is the power conversion efficiency (PCE), which is defined as the ratio of output electrical power to input light power.

$$PCE = \frac{P_{max}}{P_{in}} = \frac{V_{oc} \times J_{sc} \times FF}{P_{in}} \quad (2.8)$$

With reference to the series and shunt resistances and the equivalent circuit shown in Fig.2.3, at open-circuit voltage point, R_s does not affect the device performance since there is no current flow under open-circuit condition. However, near open-circuit voltage point where the current is low, the J - V curve is strongly affected by R_s . A low R_{sh} in the device causes power losses by providing an alternative path for the photocurrent. Such effect directly

reduces the amount of photocurrent that can be extracted from the device.

Fig.2.5 shows the effect of non-negligible R_s and R_{sh} respectively.

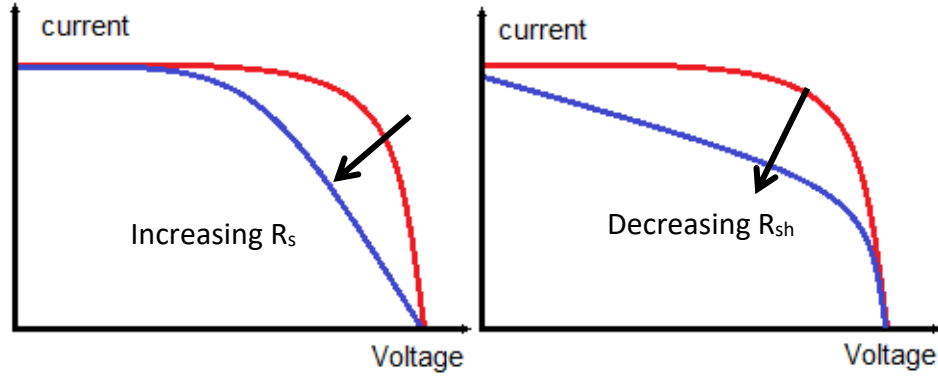


Figure 2.5: The effect of non-negligible R_s and R_{sh} .

To characterize the J - V curve of a solar cell, a schematic of standard measurement system or a solar simulator is shown in Fig.2.6 [30].

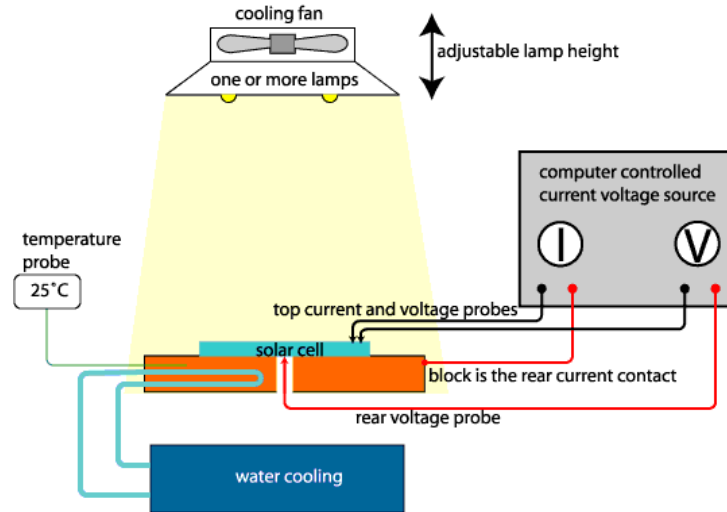


Figure 2.6: Schematic of standard solar cell performance measurement setup with standard illumination and temperature [30].

The input light power P_{in} is provided by a lamp and an optical filter system that deliver an air mass 1.5 (AM1.5) spectrum with a power intensity of 0.1 W/cm^2 .

The cell is placed on a temperature controlled plate to maintain its

temperature at 25 °C. The J - V curves are measured by a computer controlled I - V source with four probes connected to the solar cell sample.

Other than the J - V characteristics, the external quantum efficiency (EQE) measurement is also a fundamental characterization indicator for solar cells. The EQE measurement allows one to quantify how good a solar cell can convert the solar energy to electrical energy as a function of wavelength. It is defined by the ratio of the number of charge carriers collected by the solar cell to the number of incident photons at a given wavelength. The EQE is determined from Eq.(2.8),

$$EQE(\lambda) = \frac{I_{ph}(\lambda)}{q\phi_{ph,\lambda}} \quad (2.9)$$

where $I_{ph}(\lambda)$ is the photocurrent generated at a wavelength λ , and $\phi_{ph,\lambda}$ is the rate of photon incident on the solar cell at that wavelength. The measurements are performed in the spectral range of 350 to 1200 nm. Ideally, if all the photons of a certain wavelength are absorbed and the resulting charge carriers are successfully generated and collected by the external circuit, then the EQE at that particular wavelength is 100 %. However, the EQE will be below 100 % for almost all types of solar cells due to the presence of optical and electrical losses, for example, parasitic absorption, bulk recombination losses etc.

The spectrophotometry measurement is also a commonly used characterization technique for the optical properties of a solar cell. With the reflectance and transmittance measured in an integrating sphere, the absorptance of a device can be calculated by,

$$Absorptance(\lambda) = 1 - Reflectance(\lambda) - Transmittance(\lambda) \quad (2.10)$$

Such measurement allows one to quantify how good a solar cell can absorb light as a function of wavelength. With tungsten-halogen/deuterium light source and PbS light detector, one can measure the reflectance or transmittance data with a range of 170 to 3300 nm and a resolution as low as 1 nm. Typically, absorptance data are cross compared with EQE on the same device. The difference between the absorptance and EQE quantifies the optical losses such as parasitic absorption by the non-active layers and also the electrical losses such as recombination.

2.2 Silicon, organic, organic/silicon hybrid and silicon thin film solar cells

2.2.1 Silicon solar cells

Despite the availability of different materials that are available for photovoltaic technology, the crystalline silicon based solar cell, mono-crystalline (c-Si) or multi-crystalline (mc-Si), took up to 93 % of the PV market share in 2016 [31]. This is due to the abundant material availability, compatibility with the current Si microelectronics industry which provides well established manufacturing technology expertise. Commercially available crystalline silicon solar cells

usually have an efficiency around 18%. Fig.2.7 shows a typical monocrystalline and polycrystalline silicon solar cell, and simplified cross-section of a commercial monocrystalline Si solar cell [32].

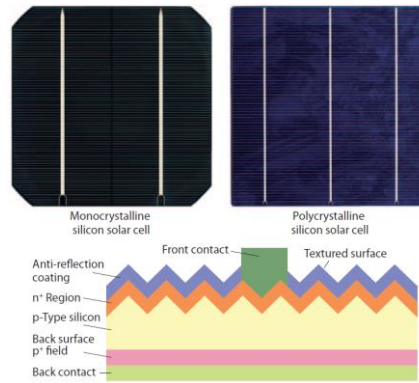


Figure 2.7: A typical monocrystalline and polycrystalline silicon solar cell, and simplified cross-section of a commercial monocrystalline silicon solar cell [32].

Standard commercial crystalline silicon solar cells are produced using boron doped p-type silicon wafers, either monocrystalline substrate that is grown by the Czochralski (CZ) process or polycrystalline substrate that is cut from polycrystalline ingots grown in quartz crucibles. Using a strong alkaline solution, the front surface of the wafer is etched into micrometer size pyramid structures to reduce reflection of incident light. Highly phosphorus doped n++ type silicon is formed by high temperature furnace (800 to 1000°C) diffusion process under POCl_3 gas environment. Using chemical vapour deposition technique, a thin layer of anti-reflective coating (ARC), typically silicon nitride (SiN_x), is deposited to further reduce the reflection losses. The photo generated carriers are collected by the back and front contacts formed by firing of screen-printed aluminum paste and silver paste respectively. The front silver contact can penetrate through ARC layer during the firing process,

forming a good electrical contact with the n^+ region, and the back surface p^+ field (BSF) is formed as well to suppress recombination of minority carriers.

Mono-crystalline silicon solar cells with 26.7 % PCE have been achieved by Photovoltaic & Thin Film Device Research Laboratories, Kaneka Corporation [33]. High efficiency Si solar cells can be produced using various approaches and techniques. Some of the high efficiency Si solar cells include Passivated Emitter and Rear Locally/Totally diffused solar cells (PERL/PERT) [34], Heterojunction with Intrinsic Thin layer solar cells (HIT) [35], Interdigitated Back-Contact (IBC) solar cells [36], Heterojunction Interdigitated Back Contact (HJ-IBC) solar cells [37] etc.. A typical PERL and PERT solar cells are shown in Fig.2.8 [38].

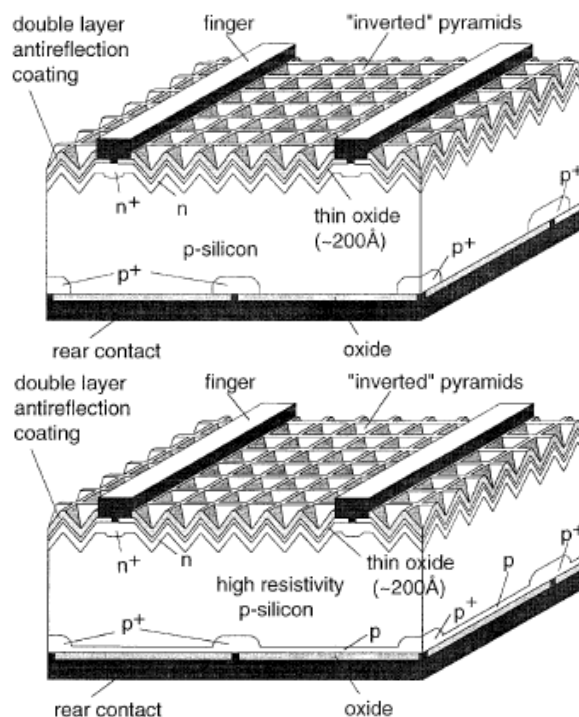


Figure 2.8: A typical PERL (left) and PERT (right) solar cell schematic [38].

PERL technology can achieve a very high open-circuit voltage as most of the cell surface areas are passivated with high quality trichloroethane grown SiO_2 . Both front and rear metal contact area are also passivated by heavily doped layers by diffusion. As a good light trapping structure, the inverted pyramid front surface also offers additional short-circuit current. To reduce the current crowding effect, PERT cell structure was introduced. It is done by having an additional diffusion step of a light boron doped layer along the entire rear surface of the cell, while other features of PERL cell remain.

A typical structure of an n-type Si HIT solar cell is shown in Fig.2.9. An intrinsic hydrogenated amorphous silicon (a-Si:H) layer, a doped amorphous-Si layer and a Transparent Conductive Oxide (TCO) layer are deposited on both sides of a crystalline-Si substrate. Grid electrodes are also fabricated on both sides of the cell.

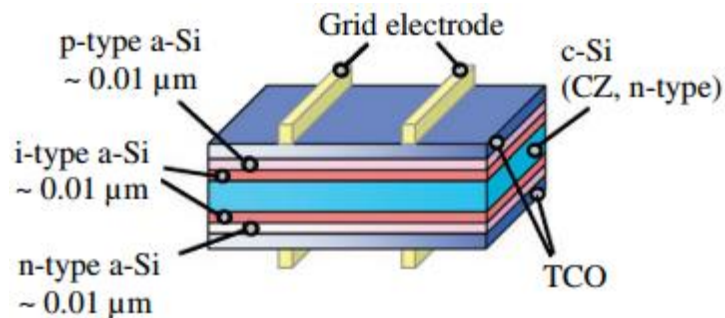


Figure 2.9: A typical structure of n-type Si HIT solar cell [35].

The HIT solar cell uses high quality and very thin hydrogenated amorphous Si (a-Si:H) layers to form the heterojunction. In addition, a high quality intrinsic a-Si:H layer can effectively passivate the surface of the crystalline silicon

substrate. As a result, this cell can achieve a high open circuit voltage of more than 0.7V.

Typical structure of an IBC solar cell [36] and a HJ-IBC solar cell [37] are shown in Fig.2.10 (a) and (b) respectively.

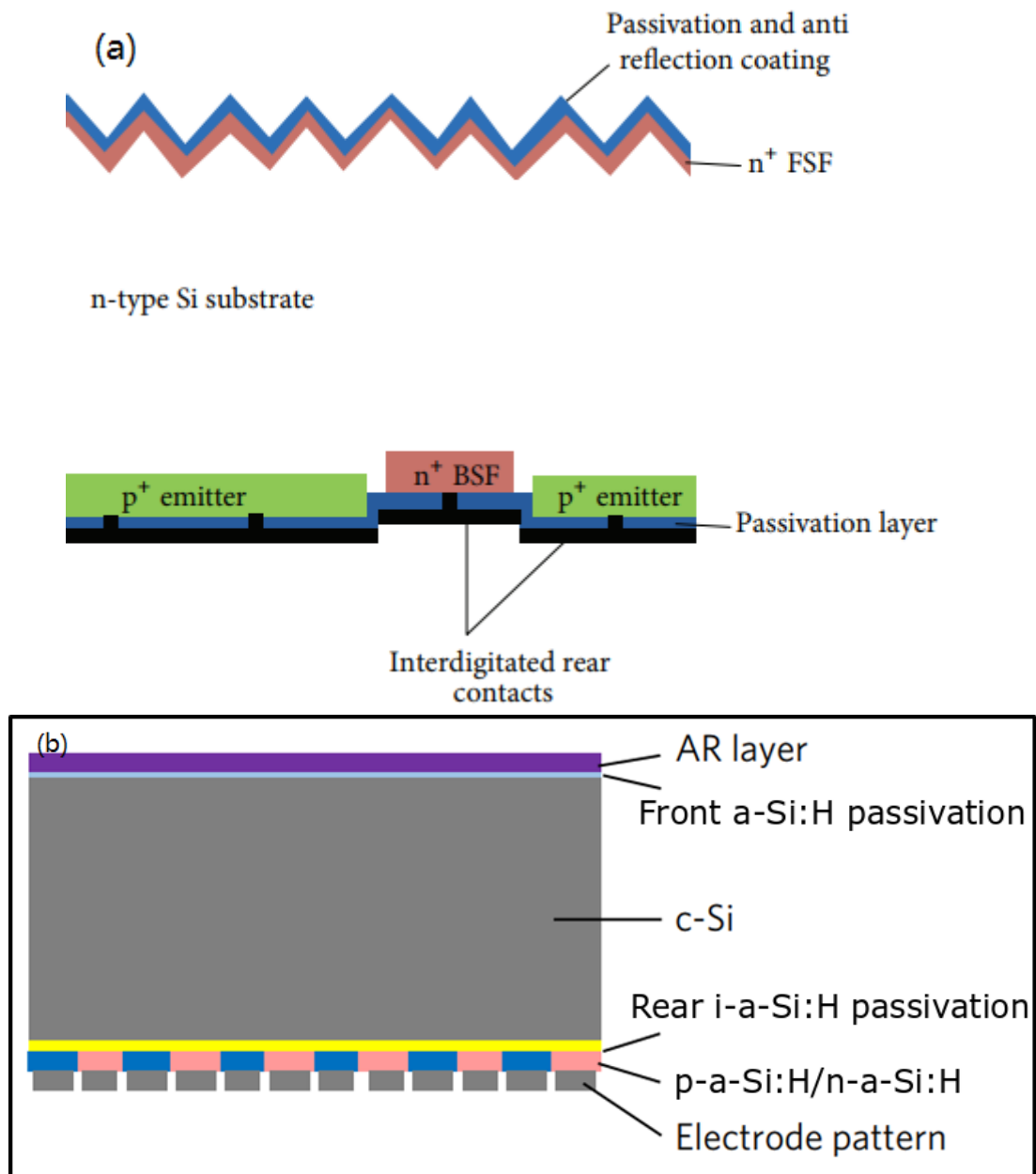


Figure 2.10: IBC and HJ-IBC solar cells.

Such IBC designs have higher absorption of light because of the removal of the front side electrode shading losses. With high quality intrinsic a-Si:H passivation, a current world record of 26.7% power conversion efficiency was achieved by Photovoltaic & Thin Film Device Research Laboratories, Kaneka Corporation using the HJ-IBC design [33].

With the introduction of the above mentioned advanced technologies and manufacturing processes, the advantages of the n-type monocrystalline silicon substrates may soon outweigh the currently dominating p-type monocrystalline silicon substrates in the field of crystalline silicon solar cell [39]. As predicted by ITRPV 2017, market share of n-type monocrystalline silicon will increase from 5% in 2014 to around 30% in 2027 [40]. Theoretically, both n-type and p-type silicon substrates can be used for solar cell fabrication. Historically, solar cell research was initially started in satellites applications and development. The superior resistance against cosmic radiation of p-type silicon promoted the research and development of p-type silicon solar cell technologies. Other than that, due to the high boiling point of B_2O_3 , it remains in liquid form during diffusion process. The uniformity of the diffused boron concentration was hard to control. Besides, to achieve the same sheet resistance for a phosphorus doped emitter, boron-doped emitter requires longer diffusion time at higher temperature. Hence, to have a p⁺ doped emitter on n-type silicon substrate was difficult. With the recent developments of the manufacturing technologies, technical problems mentioned above have been solved. Without the concern on cosmic radiation on earth, the advantages of n-type silicon solar cells, including longer minority carrier life

time, and no light degradation, has revealed more potential for higher efficiency and better stability than p-type silicon solar cells. Even though crystalline silicon solar cells have dominated the photovoltaic market for decades, their high temperature and hence high process cost, has encouraged researchers to look for alternative photovoltaic devices that are low cost and yet with good performance.

2.2.2 Organic solar cells

Recently, organic materials have attract great attention for photovoltaic applications due to their advantages in the manufacturing process, including solution based, low temperature, low cost, large area etc. [41][42]. Organic solar cells, also called organic photovoltaic (OPV), have made many breakthroughs with recent PCE of $11.2\pm0.3\%$ [11]. Organic solar cell operation principles are different from those of inorganic solar cell. For organic materials with long chain of carbon conjugate system, where carbon atoms are connected with alternating single and double covalent bonds, and the carbon nuclear surrounding electron p_z orbitals delocalized forming a delocalized bonding π orbital with a π^* antibonding orbital. The delocalized π orbital is the highest occupied molecular orbital (HOMO), and the π^* orbital is the lowest unoccupied molecular orbital (LUMO), which is similar to the conduction band and valence band respectively for inorganic semiconductor material. Figure 2.11 illustrates the energy band diagram of a bulk heterojunction single junction organic solar cell. When incident light shines on the organic heterojunction, excitons are generated, which are similar to

electron-hole pairs in inorganic solar cell devices. The generated excitons are then separated into electrons and holes to generate electric current.

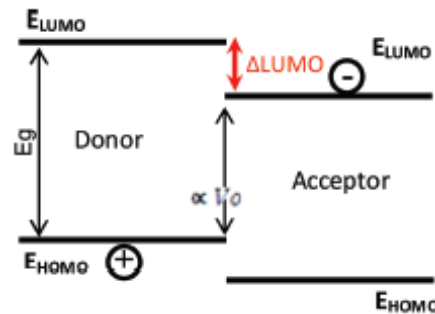


Figure 2.11: Energy band diagram of a bulk heterojunction single junction organic solar cell.

Figure 2.12 shows different categories of organic photovoltaic (OPV) based solar cells on their structures [43]. Figure 2.12 (a) shows a single layer of organic material sandwiched between two electrodes. Typically material like indium tin oxide (ITO work function ~ 4.5 eV [44]) is used for cathode and lower work function material like Al (~ 4.28 eV)/Mg (~ 3.66 eV) is used for anode. The difference in the work functions will induce a weak internal built-in electric field. As this kind of OPV suffers from low exciton separation rate and high recombination loss, its PCE is typically very low.

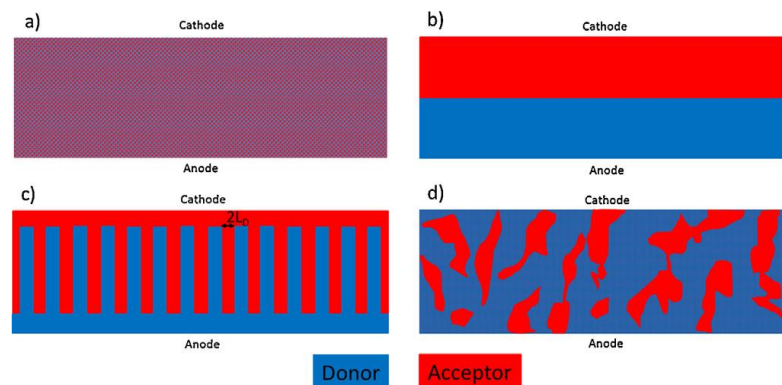


Figure 2.12: Different categories of OPV based on their structures [45].

Figure 2.12 (b) shows a bilayer junction OPV. Its junction is formed between two types of organic materials: a donor with higher LUMO and HOMO levels, and an acceptor with lower LUMO and HOMO levels. The internal built-in electric field, formed due to the energy level difference between the donor and acceptor, can separate the excitons more efficiently than the single layer OPV. However, the exciton separation is effective only at the interface between the donor and acceptor. For excitons generated far away from the interface, they will recombine before reaching the junction interface because the diffusion length is only of the order of 10nm [46]. To overcome this problem, bulk heterojunction OPV has been developed. Figure 2.12 (c) shows an ideal morphology of a bulk heterojunction solar cell and Fig.2.12 (d) depicts a typical morphology of a solution processed device. By using a bulk heterojunction structure, more excitons can diffuse to the donor/acceptor interface and be separated, resulting in higher cell performance. To address the oxygen and moisture diffusion induced degradation problem, the inverted device structure has been developed [47]. Fig.2.13 (a) and (b) shows the conventional device structure and inverted device structure respectively.

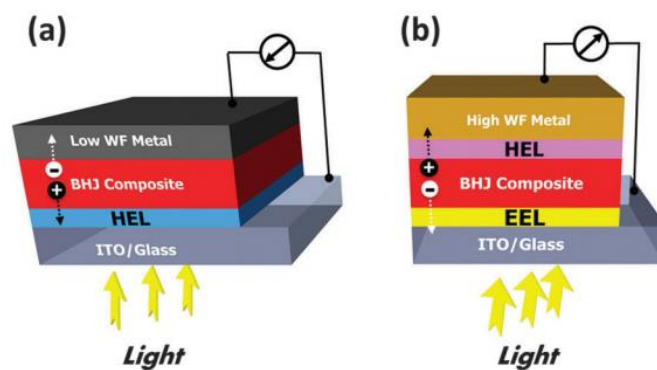


Figure 2.13: Bottom illuminated OPVs with (a) conventional device structure and (b) inverted device structure [48].

The ITO (work function ~ 4.5 eV [44]) or Fluorine doped ITO (FTO) on glass is acting as the cathode and the higher work function such as Au (~ 5.1 eV), or Cu (~ 4.65 eV) can act as the top anode. With such design, oxygen or moisture induced degradation can be effectively mitigated by the thick metal layer, as Au, or Cu metal films are relatively stable in ambient environment.

Since 2009, the emerging organic-inorganic hybrid perovskite solar cell performance has progressed rapidly from the initial PCE of 3.8 % to 22.1 % in just 8 years [11], now rivalling the efficiency of highly efficient solar cells. The excellent material properties such as strong optical absorption, direct bandgap, long carrier lifetime and diffusion length and high electron/hole mobility in crystalline state contribute to the performance boost of perovskite solar cells [49]–[53]. Future research direction in this field involves i) improving the stability of the material, ii) removing lead in the active material for an environmental friendly fabrication process, iii) also scaling up and solving the technical issue in cell to grid conversion, for example depositing flat, uniform and fully covered perovskite thin-films by industrial available approaches [54], [55].

2.2.3 Organic/silicon hybrid solar cells

Despite all the breakthroughs and improvements that organic solar cells have achieved, there are still many inherent disadvantages that organic solar cells

possess. Compared with inorganic solar cells, organic solar cells have lower PCE due to shorter carrier life time and lower carrier mobility. They also suffer from stability issues due to oxygen and water vapour induced degradation of organic materials in atmospheric ambient [56]. To combine the advantages of inorganic solar cells, such as their long carrier life time and high carrier mobility, and the advantages of organic solar cells, such as their solution based, low cost, low temperature and large scale manufacturing process, the idea of hybrid solar cell has emerged. Typical hybrid solar cells consist of organic donor material, acting as hole transport medium, and an inorganic acceptor material, acting as electron transport medium.

When choosing the organic materials, it is important to consider those with appropriate energy band structure and hole transport capability. Traditionally, poly (3-hexylthiophene-2,5-diyl) (P3HT), PTB7 and PDTTTPD have been used due to their relatively low band gap (around 1.6 eV) which favours solar radiation absorption and provides excellent hole mobility, etc.[57]. In recent years, Poly(3,4-ethylenedioxythiophene):Polystyrene sulfonate (PEDOT:PSS) has been actively researched in the field of both organic solar cells, as well as hybrid solar cells [58]. PEDOT:PSS is the most successful conducting polymer in terms of practical applications, owing to its aqueous dispersion, transparency in visible light range, spontaneous charge transfer with fast kinetics induced by its superior conductivity and high work function [59], etc.. Figure 2.8 shows the chemical structures of PEDOT and PSS [59]. As for inorganic material, various types including CdSe, CdS, CdTe, Si, PbS, TiO₂, ZnO, ZnS, etc can be considered [57]. Among these Si is attractive due to its appropriate energy band gap for solar light absorption [60], mature

manufacturing process, abundant material supply, etc. Due to above reasons, Si/PEDOT:PSS based inorganic/organic solar cells have been actively studied [61], [62], [71]–[74], [63]–[70] and tremendous progress and break-through has been made with the highest PCE of 13.9% [72] (front PEDOT:PSS design) and 20.6% [75] (back PEDOT:PSS design) reported to date. Figure 2.10 shows a typical device structure of the planar Si/PEDOT:PSS heterojunction hybrid solar cell.

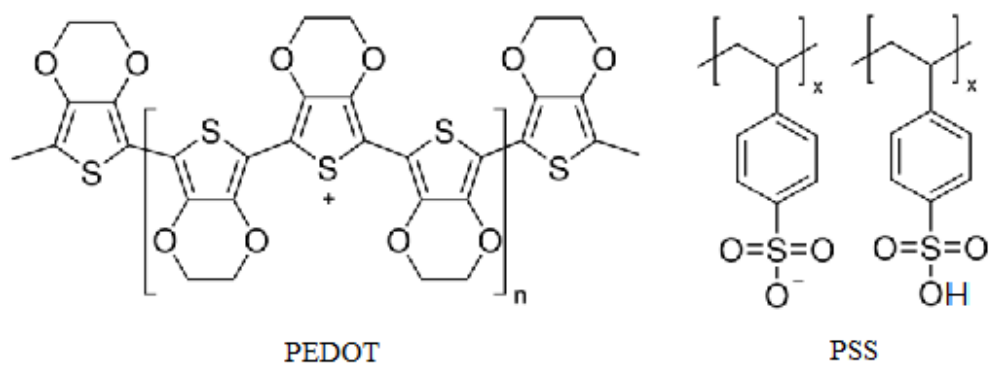


Figure 2.14: Chemical structures of PEDOT and PSS.

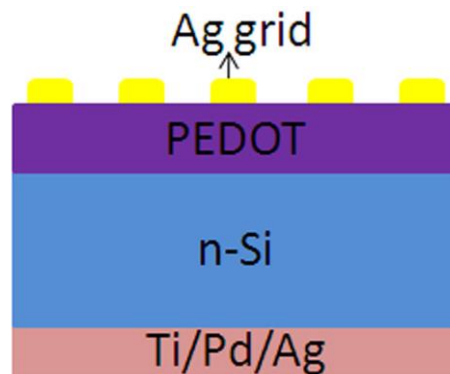


Figure 2.15: Device structure of a planar Si/PEDOT:PSS heterojunction hybrid solar cell.

Silicon dioxide (SiO_2) is well known as an excellent passivation material on bare Si substrates [68], [76]. The termination of dangling Si bondings with SiO_2 can significantly reduce the surface recombination velocity by minimizing

the defective silicon surface. He et al. reported that well controlled and optimized naturally formed SiO_x layer on n-type silicon substrate acts as a band bending layer that favours the hole injection towards PEDOT:PSS layer [77]. Figure 2.16 illustrates the energy band diagrams of the different Si/PEDOT:PSS with the Si surface terminated with hydrogen and SiO_2 , where it can be seen that the latter provides a favourable band bending for hole collection at the PEDOT:PSS. In fact, not only the thickness but also the quality of the SiO_2 interfacial layer plays an important role in high efficiency hybrid solar cells [78]. As the quality of the naturally formed native SiO_x layer is sensitive to the environmental conditions including temperature, humidity, etc., leading to the variations in surface defect density, hydrophilicity, surface topography, and oxide thickness and, thus, the discrepancies in the PCE values of the solar cells [79].

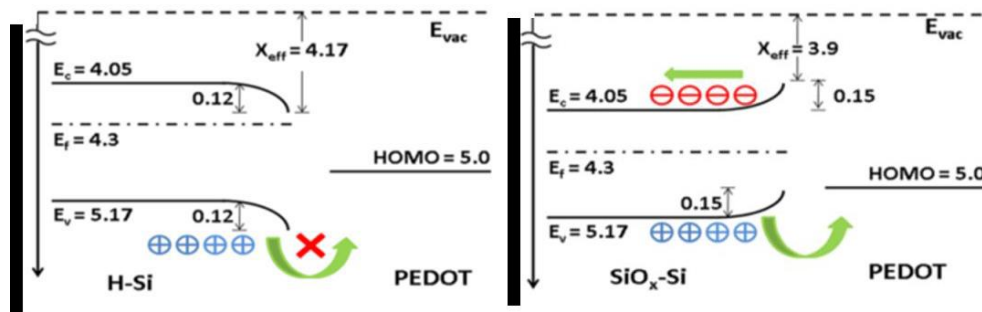


Figure 2.16: The energy band diagrams of differently terminated silicon surface in contact with PEDOT:PSS layer [77].

Due to the aqueous dispersion property of PEDOT:PSS, different co-solvents and surfactants' effects on the wetting behaviour of PEDOT:PSS solution on Si substrate have also been studied. Those studies were typically carried out with different interfacial SiO_x conditions, spin caster speed, etc. [68], [80].

2.2.4 Silicon thin film solar cells

The first hydrogenated amorphous silicon (a-Si:H) film was accidentally deposited by R. Chittick in 1969 [81] when he was experimenting with silane (SiH_4) plasma. Since then W. E. Spear et al. were the first to systematically study plasma-enhanced chemical vapor deposited (PECVD) a-Si:H films based on silane plasmas and optional doping gases, e.g. silane mixed with PH_3 for n-type films and silane mixed with B_2H_6 for p-type films. In 1977, the p-i-n type a-Si:H solar cell was introduced by D. Carlson et al. at RCA laboratories, Princeton, New Jersey, USA [82]. The classical p-n type diode, similar to crystalline silicon solar cells, was not adopted. This is because, firstly, the n/p doped layers are highly defective with additional silicon dangling bonds introduced, which are the main recombination centers in this material, due to the incorporation of foreign atoms like boron or phosphorus. Secondly, due to the short minority carrier diffusion length ($\sim 0.1 \mu\text{m}$ for undoped and $\sim 1 \text{ nm}$ for doped material), as compared to $200 \mu\text{m}$ in crystalline silicon wafers, it becomes impossible to collect photo-generated carriers by diffusion only. Hence, drift assisted carriers separation is also introduced by the internal electric field built by the n and p layers over the intrinsic layer sandwiched in between, as shown in Fig. 2.17.

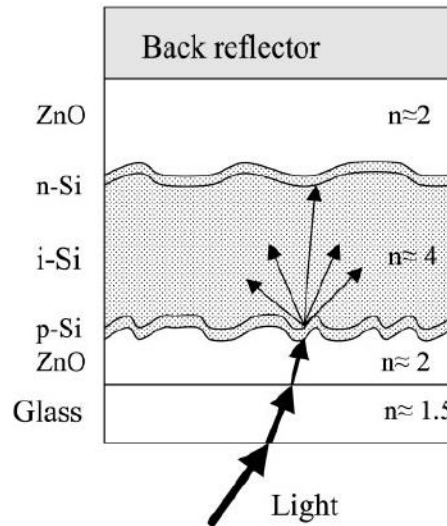


Figure 2.17: Schematic sketch of a typical p-i-n thin-film silicon solar cell.

Only 5 years after the first report, a-Si:H solar cells with efficiencies over 10% had been obtained in 1982 [83]. However, light-induced degradation effect (the Staebler-Wronski effect [84]) leads to stabilized efficiency lower than the initial values of such solar cells. Even though it is reversible upon thermal treatment at temperature around 100 °C, the complete prevention of light induced degradation of a-Si:H solar cell has not yet been achieved.

Microcrystalline silicon thin film ($\mu\text{c-Si:H}$) is a variant of a-Si:H, produced under higher plasma input power and higher hydrogen dilution ratio ($R=[\text{H}_2]/[\text{SiH}_4]$) [85]. It is a two-phase material consisting of crystalline grains and amorphous tissue. Since the first study about the deposition of $\mu\text{c-Si:H}$ using PECVD as reported by Usui et al in 1979 [86], research activities on this material including its application on solar cell field grew continuously. In 1996, an efficiency of 7.7% p-i-n type fully microcrystalline silicon thin film solar cell reported by J. Meier et al. at Neuchatel University marked the first well performing $\mu\text{c-Si:H}$ solar cell [87]. Unlike a-Si:H solar cells, these $\mu\text{c-Si:H}$

solar cells generally do not suffer from a pronounced Staebler-Wronski effect. From then onwards, with the aim of developing high efficiency devices, the focus of development has been shifting from single junction to a-Si:H/ μ c-Si:H double/triple junction tandem solar cells. To date, world record efficiency of 14.0% has been achieved by AIST with an a-Si:H/nc-Si:H/ μ c-Si:H triple junction structure [88], efficiency of 16.3% has been reported by USSC with a-Si:H/a-SiGe:H/ μ c-Si:H triple junction structure [89].

2.3 Nano-structuring techniques

Despite all the advantages of silicon as the light absorbing material in solar cells, due to its indirect band gap, it has low absorption coefficient. In order to effectively absorb the solar radiation, the active silicon layer thickness has to be at least 200 μ m for a commercial crystalline silicon solar cell. On the other hand, the use of a thinner active material in a solar cell is advantageous. It not only saves the material cost, but also offers the added advantage of efficient charge-carrier transport. To overcome the poor light absorption of the thin silicon active layer, surface texturing techniques have been actively applied in solar cell device fabrication.

As the current industrial standard, sodium hydroxide (NaOH) or potassium hydroxide (KOH) dissolved in water is normally used for both saw damage removal and surface texturing. Such strong alkaline etching process has different etch rates for different crystalline orientations. As a result, small pyramids with a square base are randomly distributed over the wafer surface

for monocrystalline silicon wafers with a (100) surface orientation. With such texture, the surface reflectivity can be reduced from 35 % to 12 % [90]. In recent years, black silicon technology has also been implemented in solar cell mass production lines [91]. Black silicon refers to silicon surfaces covered by a layer of nano- or fine micro-structures, which effectively suppresses reflection, while simultaneously enhancing the scattering and absorption of light. As a consequence, the silicon wafers appear black, instead of the slightly blue typical of planar silicon wafers [92]. Black silicon can be fabricated by various techniques including electrochemical etching [93], metal assisted chemical etching [94], reactive ion etching [95], [96], etc. Black silicon technology provides excellent antireflection properties; reduced material cost from lesser waste silicon material during etching process and reduced fabrication cost from no additional antireflection coating needed. However, due to the fine nanostructures produced during wet etching, a larger number of defects are introduced on the silicon surface. Effective surface passivation is required for a well performing device [97].

In academia, recent studies on various nanostructures based silicon solar cells have shown great improvements in terms of light absorption enhancement [98]–[100]. Typical nanostructures include array of silicon nanowires (SiNWs) [101]–[109], silicon nanoholes (SiNHs) [110]–[112], silicon nanocones (SiNCs) [113], silicon nanoconical frustums [114], silicon nanotubes [115], silicon inverted nanocones [116], silicon inverted nanopyramids [117], silicon nanofunnels [118], etc. The reason for absorption enhancement is due to enhanced scattering of light by the nanostructures, which extends the optical diffusive path length of light and results in a stronger

light absorption. High surface recombination rate in nanostructured silicon solar cell remains a critical issue as this will lead to a lower external quantum efficiency (EQE) over shorter wavelength range and hence poorer J_{sc} and V_{oc} [12], [13].

PS sphere assisted lithography, which is also known as one of the colloidal lithography or natural lithography techniques [22], [23], is a promising cost-effective fabrication tool for producing regular and homogenous arrays of nanostructures with different sizes [121]–[123]. Due to the high manufacturing cost involved in deep ultraviolet (DUV) and nano-imprint lithography technologies, in this work we have chosen the cost-effective PS sphere assisted lithography for the fabrication of the nanostructures. A detailed study on the application of this technique in our work will be present in chapter 3.

2.4 Solar cell simulation methodologies

By applying Maxwell's equations based on numerical methods, we could simulate how light interacts with silicon nanostructures. The simulation results are useful in terms of guiding the nanostructure design by optimizing the geometry dimensions and also providing physical insight into the absorption enhancement process. There are different numerical methods, such as finite element method (FEM) [124]–[130] and finite difference time domain (FDTD) method [118], [131]–[134], transfer matrix method (TMM) [111], [135], [136], rigorous coupled-wave analysis (RCWA) method [137]–[139], etc. Different structures have been simulated previously, including SiNW [109], [124], [125],

[135], [136], [140], SiNH [126], [128], [129], [132], [133], [138]. Typical design variables include the diameter D of the nanostructures, periodicity P , height H , film thickness t , filling ratio f or D/P ratio and special dimensions according to the structure requirement. The reflectance (R) and transmittance (T) of the nanostructures are calculated by the numerical method chosen, and the absorption (A) is given by $A = 1 - R - T$. Assuming that each and every photon absorbed is used to produce one electron hole pair, i.e. the internal quantum efficiency is 100%, the photo-generated current I_{sc} of the device can be expressed as:

$$I_{sc} = \int_{300}^{1100} \frac{E_g P(\lambda) A(\lambda)}{E(\lambda)} d\lambda \quad (2.10)$$

where E_g is the band gap of silicon, $E(\lambda)$ and λ are the photon energy and wavelength of incident sunlight respectively, $A(\lambda)$ is the absorption spectrum of the active material and $P(\lambda)$ is the spectral irradiance of standard AM1.5G solar spectrum. The wavelength range for the integration is from 300 nm to 1100 nm, which covers the main part of the solar spectrum. By calculating the I_{sc} , the effectiveness of different nanostructures can be compared and the nanostructures can be optimized.

In this work, FEM is selected as the simulation method to study the optical properties of nanostructures due to its flexibility to handle any type of geometry and material inhomogeneity without a need to alter the formulation or the computer code (geometrical fidelity) [141]. The FEM is implemented using the software High Frequency Structure Simulator (HFSS) [142]. The FEM method is a numerical technique for obtaining approximate solutions to boundary-value problems of mathematical physics [143]. Before solving, the

structure is divided into many smaller domains called finite elements or meshes. For those finite elements, triangular elements are used for two dimensional structures and tetrahedral elements for three dimensional structures, as shown in Fig. 2.18. After domain discretization, the Maxwell equations will be set up and solved for each of the elements within the boundary. In general, the HFSS design flow can be divided into 3 stages: pre-processing, solution and post-processing. When the solution converges, results like reflection/transmission coefficient, field distribution etc. can be extracted from the solution obtained. The HFSS design flow chart is summarized in Figure 2.19.

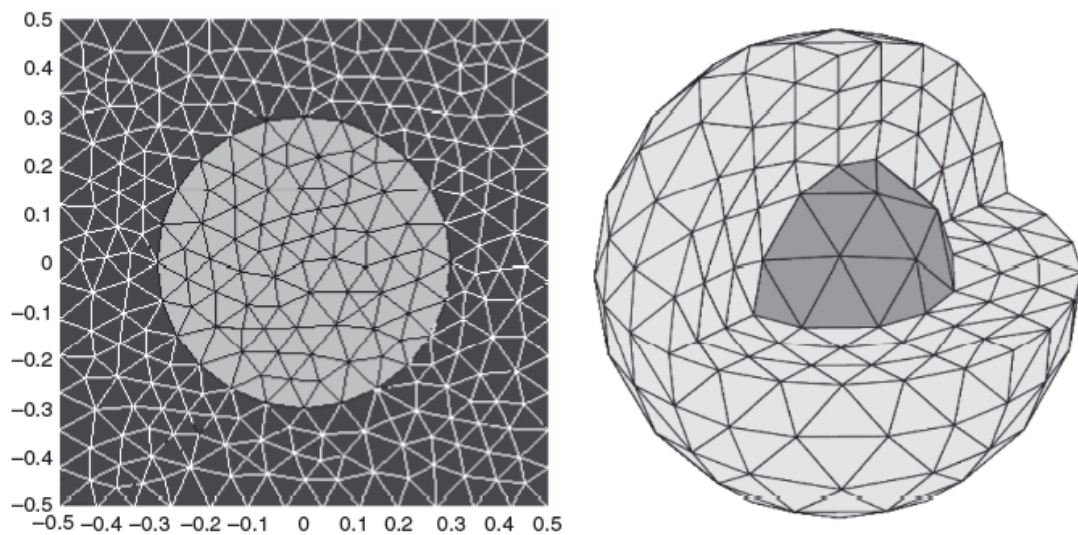


Figure 2.18: Divided finite elements in 2D and 3D structures.

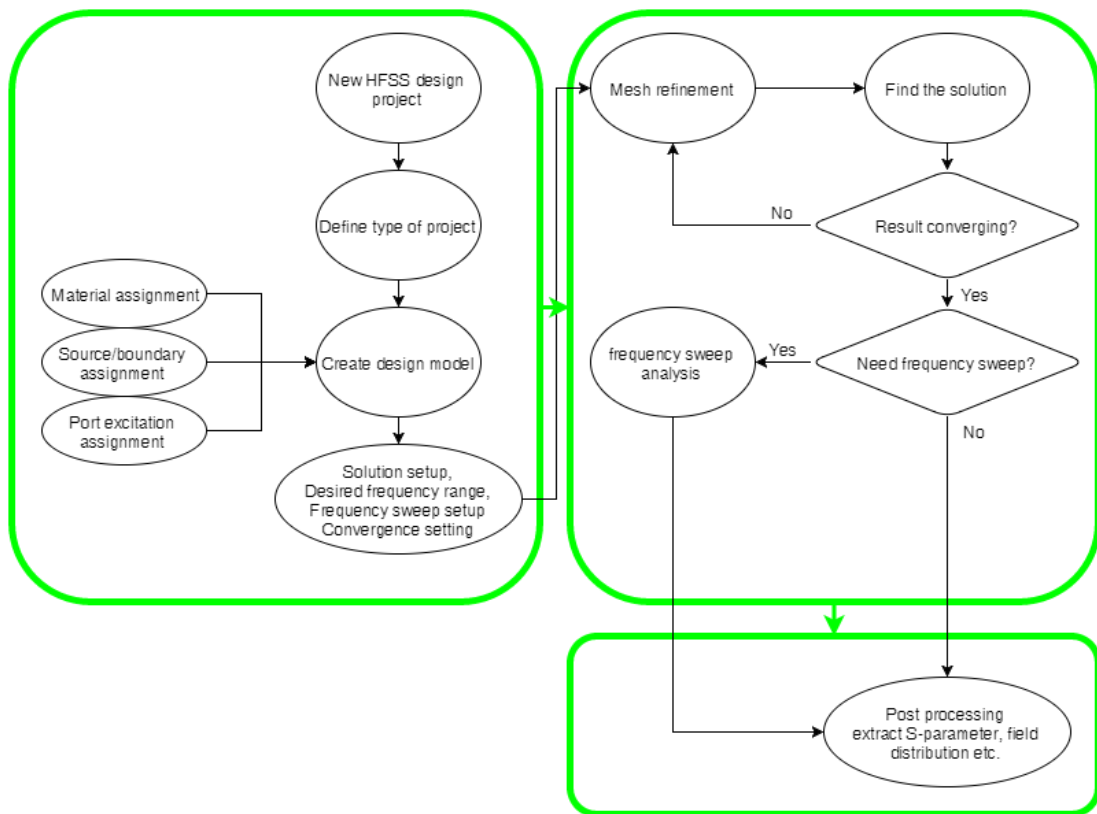


Figure 2.19: HFSS design flow chart.

Chapter 3. Improved Polystyrene Sphere Assisted Lithography with Matrix Distributed Electron Cyclotron Resonance Oxygen Plasma

In this chapter, we study the use of a matrix distributed electron cyclotron resonance (MDECR) oxygen plasma source to etch a monolayer of closely packed Polystyrene Spheres (PS). We aim at improving the patterning capability and overcoming the limitations of the existing PS sphere assisted lithography with a fine-tuned MDECR oxygen plasma source and various innovative etching conditions. Firstly, we introduce the PS sphere assisted lithography and its applications, together with a review of previous works on thin film deposition and reactive ion etching by ECR. Subsequently, the fabrication process and designed etching conditions will be introduced. After that, the effects of various etching parameters are discussed in detail. From the experimental results obtained, we summarize the morphology evolution of PS spheres under ECR oxygen plasma. Following that the conclusions drawn regarding the improvements of our innovative PS sphere lithography methodology and significance of this work will be presented.

3.1 Introduction and objectives

3.1.1 PS sphere assisted lithography and its applications

PS sphere assisted lithography (PSAL), which is also known as one of the colloidal lithography or natural lithography techniques [22], [23], is a promising cost-effective fabrication method for producing regular and homogenous arrays of nanostructures of different sizes [24]. This is not as precise as standard photolithography techniques, such as deep Ultra-Violet (UV) or extreme UV lithography [25], [26]. However, it allows one to fabricate periodic nanostructures, which are regular and up to a few hundreds of micrometer, at a much lower cost and using simpler process steps.

In general, PSAL is divided into two parts: firstly, formation and transfer of the PS monolayer or simply mask preparation; secondly, deposition of the material of interest through the opening of the ordered spheres and subsequently removal of the spheres. Figure 3.1 shows the overall process steps [24].

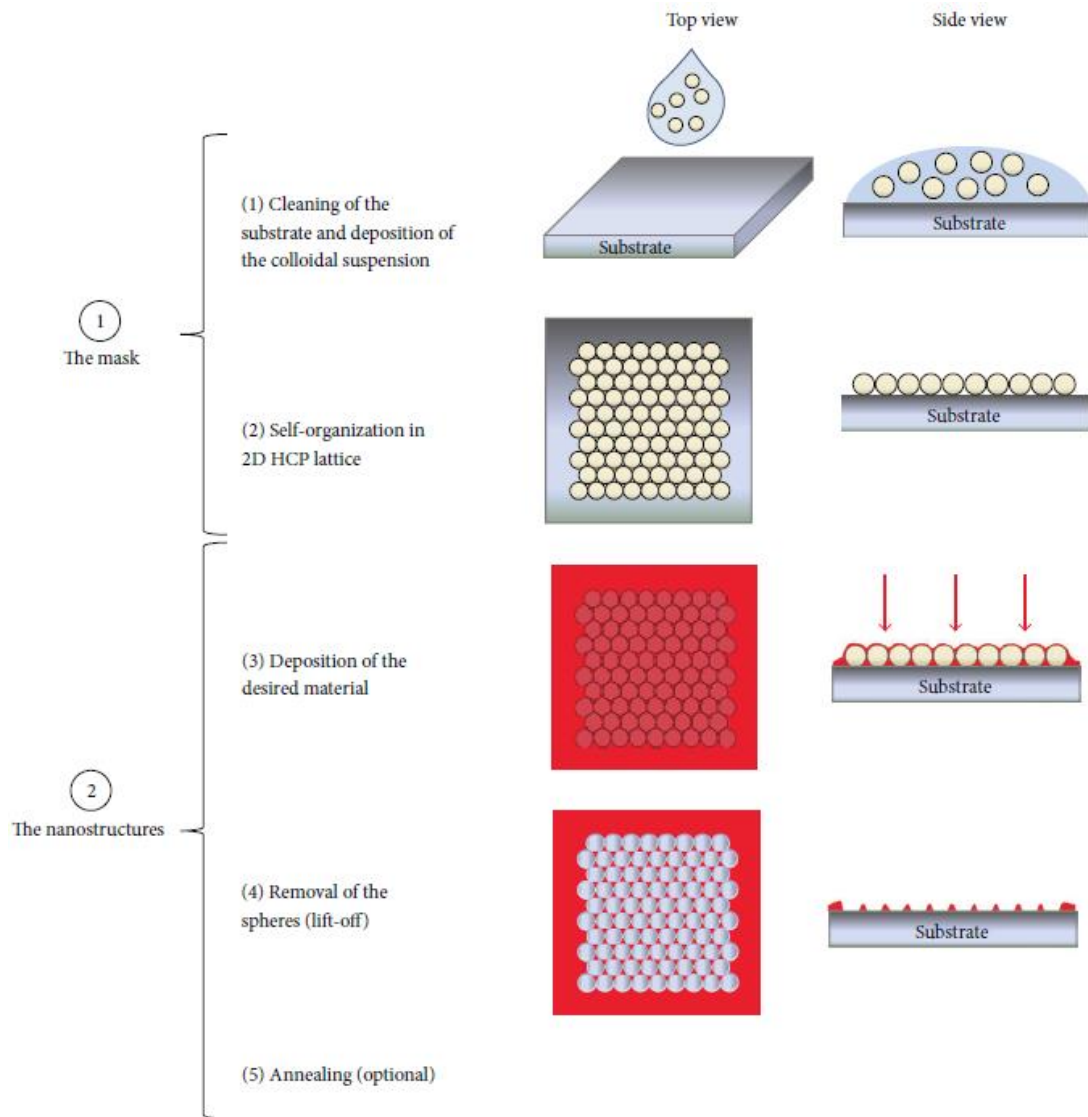


Figure 3.1: PS assisted lithography process [24].

In addition to the mask preparation step, PS sphere size reduction by oxygen plasma etching is often implemented by researchers for fabrication of different nanostructures, such as silicon nanoholes first demonstrated by *C. Haginoya et al* in 1997 [144], as shown in Fig.3.2.

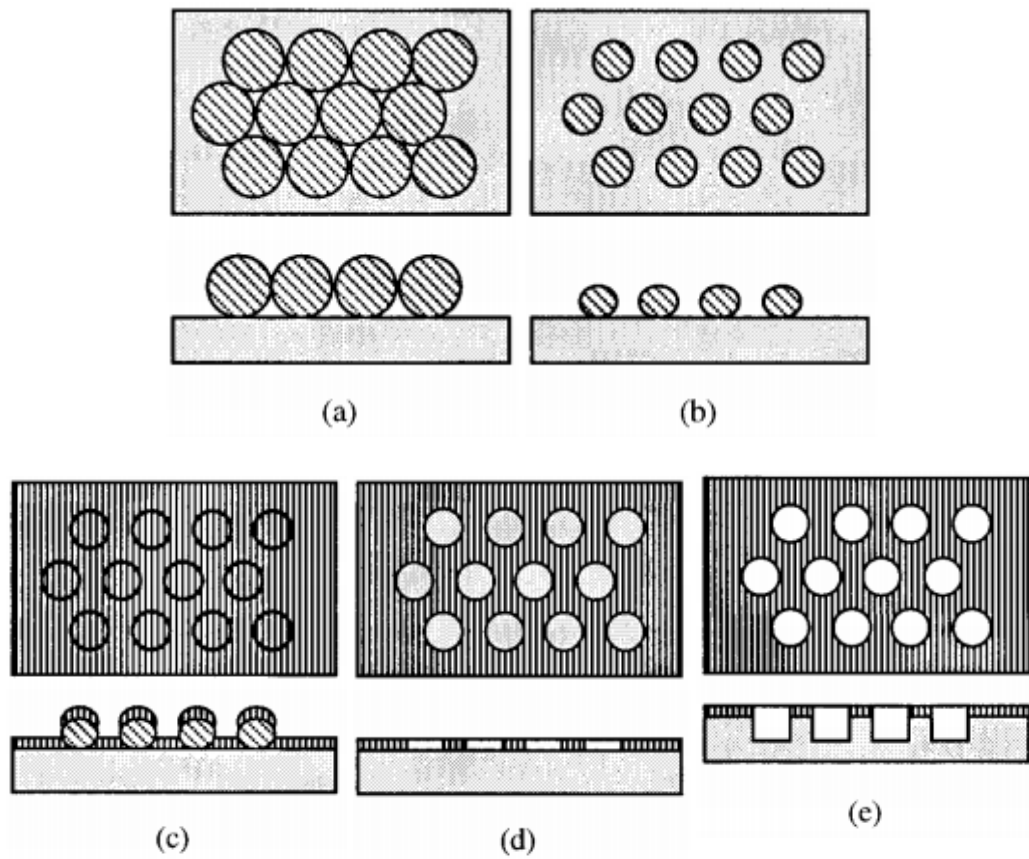


Figure 3.2: Schematic diagram of the fabrication process with top view (upper) and cross-sectional view (lower) [144]. (a) Formation of a monolayer of PS spheres on silicon. (b) PS sphere size reduction by reactive ion etching (RIE) in a oxygen plasma. (c) Sputter deposition of Pt–Pd. (d) Removal of PS spheres. (e) Formation of silicon nanohole array by RIE with CF_4 plasma.

As we can see, the periodicity of the silicon nanoholes is defined by the initial PS sphere size before oxygen plasma etching. The diameter of the silicon nanoholes is defined by the final PS sphere size after oxygen plasma etching. By combining similar processing steps with other experimental designs, 1-Dimensional [145], 2-D [146], [147] even 3-D nanostructures [148] can be fabricated. The robustness of PSAL in terms of nanostructuring of different materials has also been demonstrated [149]. As a result, formation of different

structures, like chemical vapor deposited (CVD) ZnO [150], silicon [151] and carbon nanotubes [152], dry etching based silicon nanocones [153] and nanoholes [144], wet etching based silicon nanopillars [154] and nanoholes [155], inverted silicon nanopyrimid [156], and so on, have been reported. Different applications like field emitters [157], photonic crystals [158], enhanced photocatalytic activity [159], antireflection coating [160], self-cleaned highly hydrophobic surfaces [161], solar cell back point contact formation [162], mold for nanoimprint lithography [163], etc. are enabled by PSAL.

However, PSAL has its own limits when small dimensions (less than 100 nm) are required. On the one hand, with smaller PS sphere size being used, the patterning periodicity will be difficult to be maintained. This will end up with smaller periodically packed domains. On the other hand, as a polymer, polystyrene will tend to be heated and softened after long time exposure to oxygen plasma. After a even longer oxygen plasma etching time, a rough surface with tiny frustrations will develop. Melting will result from an excessive heating due to physical bombardment by energetic ions and chemical reactions from the oxidation process. These effects will end up with an irregular shape of PS spheres after oxygen plasma etching [164]. Moreover, if a PS sphere is melted to certain degree, the patterning capability will be totally lost. In the later part of this chapter, we will demonstrate some cases where certain experimental conditions can lead to bad patterning quality. In our work, we used a modified electron cyclotron resonance (ECR) generated

oxygen plasma system to solve the above problem, which will be introduced in the next part.

3.1.2 Electron Cyclotron Resonance Plasma

ECR plasma is a kind of high density plasma with the excitation source in the microwave range. To obtain a resonant condition for the electrons, one can achieve it by setting the microwave frequency to be synchronous with the gyration frequency of the electrons. The gyration frequency of the electron is defined by the magnetic field intensity [165]. Under the condition of a uniform and static magnetic field B , due to the Lorentz force, electrons will have a circular or helical motion along the magnetic field, as shown in Fig.3.3 (a). The angular frequency ω_c of electron rotation is given by,

$$\omega_c = \frac{qB}{m} \quad (3.1)$$

and a radius r_c given by,

$$r_c = \frac{mv}{qB} \quad (3.2)$$

where v is the electron velocity perpendicular to the magnetic field. However, there won't be any energy gain of these electrons in circular or helical motion, even in vacuum under no collisions. However, if we apply a microwave electric field with an angular frequency ω on the magnetic field, as shown in Fig.3.3 (b), the path of the electron motion will be modified. A resonance effect would occur if the condition $\omega = \omega_c$ is satisfied. The electrons will be accelerated continuously and move in phase with the electric field. Above effect is commonly described as the ECR effect. For the commonly used 2.45

GHz microwave excitation, when magnitude of the magnetic field is set at the 875 Gauss, the resonance effect occurs for the electrons [166].

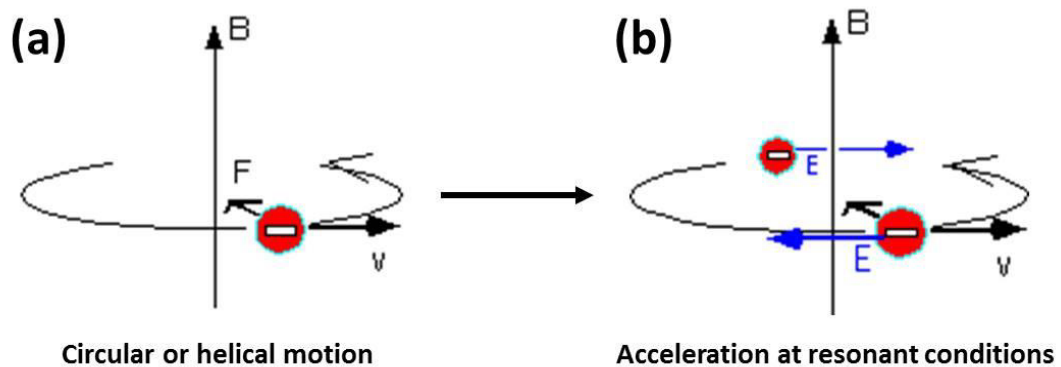


Figure 3.3: (a) The circular or helical motion of an electron in a static and uniform magnetic field. (b) Continuous ac celeration of the electron in a superimposed magnetic field and electric field [165].

Under ECR resonant condition, the electrons in the coupling region will be continuously accelerated. Ionization and momentum transfer will occur inside the plasma due to energy loss during collision between fast electrons and neutral particles [165]. Since essentially ECR plasmas operate at very low pressures (lower than 10 mTorr) and the mean free path is long, the electrons can gain enough kinetic energy at a very short time, high ionization efficiency and high plasma density can be achieved. Since the middle of 1970s and early 1980s, ECR plasmas for surface processes were extensively researched, and they have been applied to various plasma-enhanced chemical vapour deposition (PECVD) processes, like the deposition of silicon (and its alloys) [167], [168], carbon coating [169], metal oxides and dielectric materials [170], as well as passivation coatings [171]. ECR plasma based etching processes have been developed as well, due to its high plasma

density and higher ionization efficiency, hence a faster etching rate, shorter process time and higher through-put. Its etching characteristics of organic photoresist [172], semiconductor Si [173], GaN [173], dielectric film SiN_x [174], SiC [175], etc. have been widely studied.

In our work, a more recent concept of the ECR plasma source – the matrix distributed ECR (MDECR), which has been developed by *Lacoste et al* [176] in the early 2000s, is used. In the MDECR design, the excitation source is multiple elementary microwave applicators which arranged in an array form.

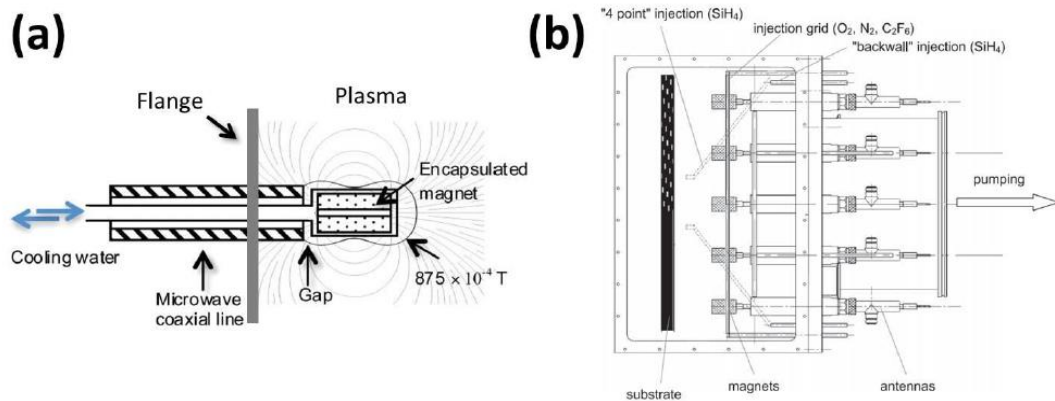


Figure 3.4 (a) Schematic of an elementary plasma excitation unit [177]. (b) Cross-sectional view of a typical MDECR reactor [178].

As shown in Fig.3.4 (a), there are two main parts in each of the microwave applicator: a coaxial microwave feedthrough with an azimuthal symmetry around along its axial direction and a cylindrical permanent magnet at the rod end [177]. A metallic envelope is used to encapsulate the magnet completely, and water cooling systems are used to keep the magnet cool. With an adjustable insertion depth mechanics, they are inserted inside the vacuum chamber. Strong ECR coupling can occur in the region close to each

separated magnet or in between two magnets next to each other and operated at opposite polarities [177]. An example of such design is shown in Fig.3.4 (b), where in a 5 by 5 array arrangement are configured for the 25 microwave applicators [178]. The substrates are placed at the other side of the process chamber. With the plasma species diffused from the source region to the target region, the surface processing can be realized. Several advantages of the MDECR plasma source over the conventional ECR plasma sources are summarized as follows: i) fabrication scaling-up can be simply achieved by inserting additional units due to the simple design of the elementary microwave applicator; ii) different fabrication conditions, especially on plasma distribution and sample surface shape, can be achieved due to the freedom to adjust the insertion depth of the elementary unit into the vacuum; iii) the absorption of the microwaves by the plasma before reaching the target ECR region is not likely to occur, since the applicator are shielded with coaxial feedthrough configuration [166], [178]. Those advantages lead to fast electron confinement, so that to sustain stable plasma, considerably lower power is required. In addition, this design can greatly reduce microwave interferences between different sources, which are achieved by reducing microwaves propagation towards the adjacent elementary units.

3.2 Fabrication Process and Conditions

3.2.1 PS sphere monolayer formation

The PS spheres used in this work had nominal diameters of 425 ± 10 nm, 607 ± 15 nm and 784 ± 23 nm, and were obtained as an aqueous monodispersive suspension of 5 w.t.% (microParticles GmbH). For simplicity, these will be referred to as 400 nm, 600 nm and 800 nm spheres. The suspension was diluted by mixing it with an equal volume of ethanol as a spreading agent prior to use. We use crystalline silicon (c-Si) wafers (100 orientated) as the substrate for the preparation of PS monolayers. Prior to use, the substrates were cleaned with acetone, isopropanol (IPA) and de-ionized (DI) water. To deposit a compact monolayer of PS spheres on the c-Si substrates, different approaches were investigated: spin coating [179], dip coating [180], solvent evaporation [181], etc. In our work, the floating-transfer method was used for the deposition of a PS sphere monolayer onto the c-Si substrates. It is a repeatable and well controlled method for large area PS sphere monolayer (more than 20 cm^2) transfer [182], [183]. On top of this method, we further improve the overall process with the use of diluted Tween-20 surfactant. The process flow is described in detail below.

A glass petri dish with an inner diameter of 15 cm and height 3 cm was first cleaned with acetone, IPA and DI water, followed with a UV ozone treatment for 15 min to achieve a hydrophilic surface. The petri dish was filled to halfway with DI water prior to adding the PS spheres. A 1 mL volume syringe, capped with 25 g needle, containing 0.5 mL of the diluted PS sphere suspension was

then put in contact at the inner sidewall of the petri dish, around 1 cm above the water surface. With a slow and steady injection of the PS sphere suspension, due to the spreading effect of ethanol, the solution firstly flowed down and spread over the inner sidewall of the petri dish, and then further spread across the water surface. During this process, the PS spheres were floated and spread on the wafer surface as well. With the capillary force acting between the hydrophobic PS spheres, a self-assembled, hexagonally closely packed monolayer of PS spheres was formed. After most of the water surface was covered by the floating PS sphere film, a few drops of 1 : 200 water diluted Tween-20 surfactant solution was added to the water surface from the sidewall of the petri dish. PS sphere film was pushed to the opposite direction of the petri dish from the place where Tween-20 entered the water surface. A compact continuous PS sphere monolayer film was finally formed on the water surface. Such “pushing effect” by the surfactant has been reported with different species like sodium dodecyl sulfate (SDS) [184]. As a non-ionic surfactant, Tween-20 offers a stronger pushing effect hence resulting in a more compact and disturbance resistant PS sphere monolayer film. For a hydrophilic surface, a 15 min UV ozone treatment was applied to c-Si substrates as well, prior to film transfer process. During the PS sphere transfer process, the c-Si substrate was firstly wetted with water and immersed below the water surface, under the PS spheres monolayer. The substrates were then lifted upward slowly so that the PS sphere monolayer was transferred onto the substrate surface. After removing the substrates from the petri dish and with PS spheres monolayer on top, they were dried in air for around one hour. Fig.3.5 shows the schematic of the overall process.

After the PS spheres monolayer deposition on the c-Si substrates, oxygen plasma etching was carried out using the MDECR process under different etching conditions.

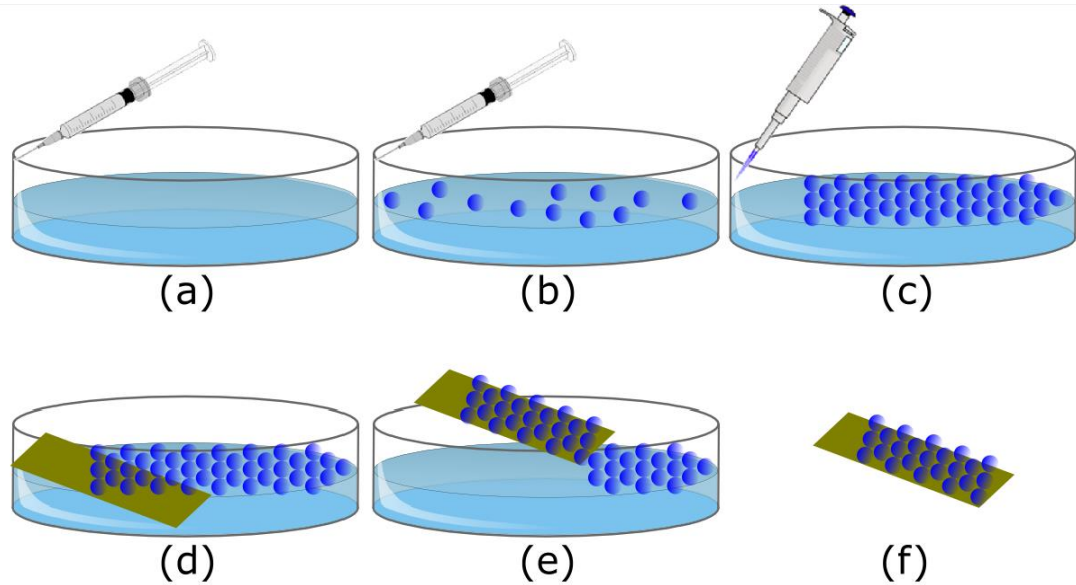


Figure 3.5: Schematic of PS spheres monolayer formation on silicon. (a) Petri dish half filled with DI water. (b) Floating of PS spheres. (c) Packing of the PS spheres with pushing effect of diluted Tween-20 surfacant. (d) Insertion of the substrate under the water surface. (e) Substrate lift-up. (f) Drying of the substrates in air.

3.2.2 Reactive Ion Etching by Matrix Distributed Electron Cyclotron Resonance generated Oxygen Plasma

The etching process was performed using an MDECR reactor. The microwave discharge, excited at 2.45 GHz, was sustained by a set of sixteen water-cooled antennas, each terminated by a permanent rare-earth magnet. To power the microwave antennas, two magnetrons generating up to 2000 W were used, with each one supplying power to eight antennas [178]. For the reactive etching plasma, the following conditions were used: 40 sccm of O₂,

pressure of 2 mTorr, and microwave power set at either 500 W or 1 kW (in either continuous or cycling mode). For the non-reactive plasma, 40 sccm of Ar, 2 mTorr pressure and 500 W power were used. The 210 mm diameter substrate holder is positioned at 100 mm downstream from the end-plane of the antenna matrix.

Recently, Li et al. studied the etching of polystyrene sphere in oxygen plasma [185]. They considered that the plasma flow contained ions, electrons, excited neutrals, radicals, and UV radiation. These highly reactive and energetic species led to the chain scission of the PS molecules, generating low-molecular-weight fragments. Early work done by Guruvenket et al. [186] concluded that an oxygen plasma can react with the polymer surface to produce a variety of atomic oxygen functional groups, including C-O, C=O, O-C=O and CO₃ at the surface. This process gave rise to volatile reaction products. During the exposure of PS sphere to oxygen plasma, two processes occur simultaneously. Firstly is the etching of the polymer surface through the reaction of atomic oxygen with the surface carbon atoms. Secondly is the physical bombardment by the energetic ions which leads to chain scission. The low-molecular-weight fragments will be more easily etched by atomic oxygen. The balance of these two processes depends on the conditions of a given etching process.

In our work, by controlling the etching power, etching mode (both in continuous and cycling mode), and using different etching gases (both oxygen and argon) and with a Faraday cage to shield the ion bombardment, not only

we could isolate the role of ions from that of oxygen radicals in the oxygen plasma, but we also improved the patterning quality of the PS sphere assisted lithography.

3.2.3 Patterning Quality Evaluation and PS sphere melting

To validate the patterning quality after PS sphere etching, a 50 nm thin Al layer is thermally evaporated on top of the substrates. To remove the PS sphere and to complete the nanostructured Al nanomesh, the substrates were immersed in toluene solution and a 10 min low power ultrasonic bath was applied. As a strong organic solvent, toluene would dissolve the PS spheres and the Al film attached to the PS sphere would be peeled off under ultrasonic bath. Fig.3.6 shows two cases where the patterning was successful (upper SEM images) and not successful (lower SEM images).

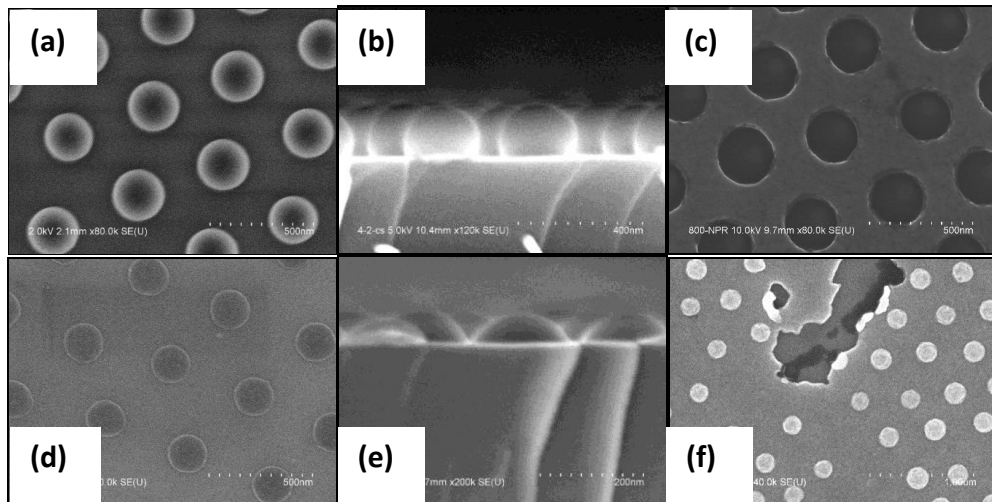


Figure 3.6: Validation of patterning capability of PS sphere arrays after oxygen plasma etching. (a) Top view of PS spheres array after etching which maintained good patterning capability. (b) Side view of (a). (c) Al nanomesh after Al film evaporation and PS sphere removal. (d) Top view of PS spheres array after etching which lost its patterning capability. (e) Side view of (d). (f) A failed case in the fabrication of the Al nanomesh.

From Fig.3.6(d-f), we can see the PS spheres were not removed due to the perfect coverage of Al on the spheres and substrate. After oxygen plasma, melting of the PS spheres on the substrates is observed in Fig.3.6(e). To characterize it, we used the contact angle concept from the wetting of the liquid on a solid surface. Fig. 3.7 shows two schematics generalized from Fig.3.6 (b) and (e).

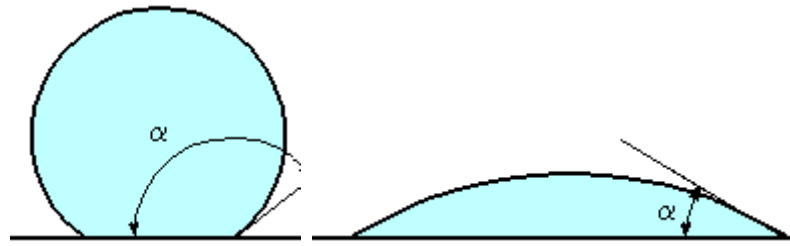


Figure 3.7: PS sphere melting with (a) $>90^\circ$ contact angle (b) $<90^\circ$ contact angle.

Successful PS sphere removal will only occur when the contact angle is greater than 90° . As for the counter case, toluene will not get in contact with the PS spheres that are encapsulated by the Al film, and hence PS spheres will not be dissolved in toluene. The melting of the PS spheres is selected as one of the most important parameters for us to justify the quality of the oxygen plasma etching conditions. To retain the patterning capability, PS sphere melting and sticking to the substrate should be avoided for a successful PS sphere removal.

3.3 Effect of Etching Conditions

In this section, we present the PS sphere etching behavior under different plasma conditions. The effects of the etching microwave power, etching mode (both continuous and cycling mode), using different etching gases (oxygen and argon) and with a Faraday cage to shield the ion bombardment, are discussed in detail.

3.3.1 Effect of etching power

In order to study the effect of the microwave input power on PS sphere etching, 500 W and 1 kW input power were used, while kept 40 sccm of O₂ flow rate 2 mTorr of process chamber pressure. Fig. 3.8 (a) and (b) shows top and cross section SEM images of the 600 nm PS sphere arrays after 3 min of 500 W etching power; and Fig. 3.8 (c) and (d) shows top and cross section SEM images after 2 min of 1 kW etching power.

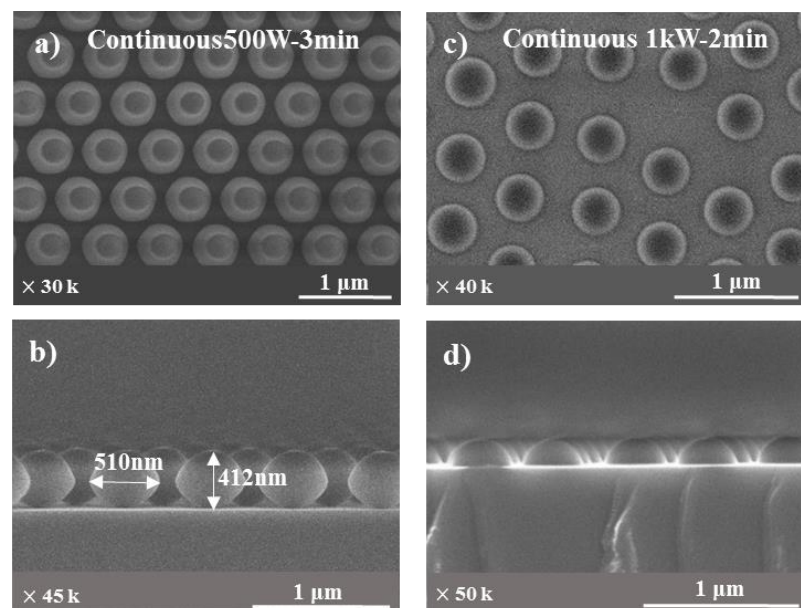


Figure 3.8: SEM images of 600 nm PS spheres etched in a continuous plasma. 3 min under 500 W (a) top (b) cross section, and 2 min under 1 kW (c) top (d) cross section.

After 3 min exposure under 500 W continuous plasma power, from the top and cross section SEM images as shown in Fig. 3.8(a) and (b), we see that the PS spheres maintained their shape and did not melt. The etched spheres end up with a slightly hexagonal shape, and have been etched to around 80% of their initial diameter. However, after 2 min exposure under 1 kW continuous plasma power, the PS spheres were completely melted, as shown in Fig. 3.8(c) and (d) that they appear rounded from the top SEM image and semispherical from cross section SEM image. The PS spheres have been reduced to 63% of their initial diameter. In both cases, PS spheres are successfully etched and their periodic arrangements are still retained. However, if the PS spheres are melted and stick to the substrate, they might lose the patterning capability, as discussed in Section 3.2.3. In order to avoid the PS sphere melting and yet attain a reasonable etching rate, alternative etching methodologies were investigated in this work.

3.3.2 Effect of etching mode

To resolve the plasma heating during etching which leads to the melting of the PS spheres, a cycling mode was used. In the cycling mode, the overall plasma etching process was divided into multiple cycles. Each of the etching cycle will have a 15 sec of plasma turned on phase and a 30 sec of plasma

turned off phase. The plasma input power applied and the total duration of the plasma turned on phase were designed to be the same with respect to the continuous mode. Both 600 nm and 800 nm PS sphere arrays formed on a c-Si substrate were used for the experiment. The SEM images of the 600 nm PS sphere array after exposure to the cycled plasma with different etching powers are shown in Fig.3.9.

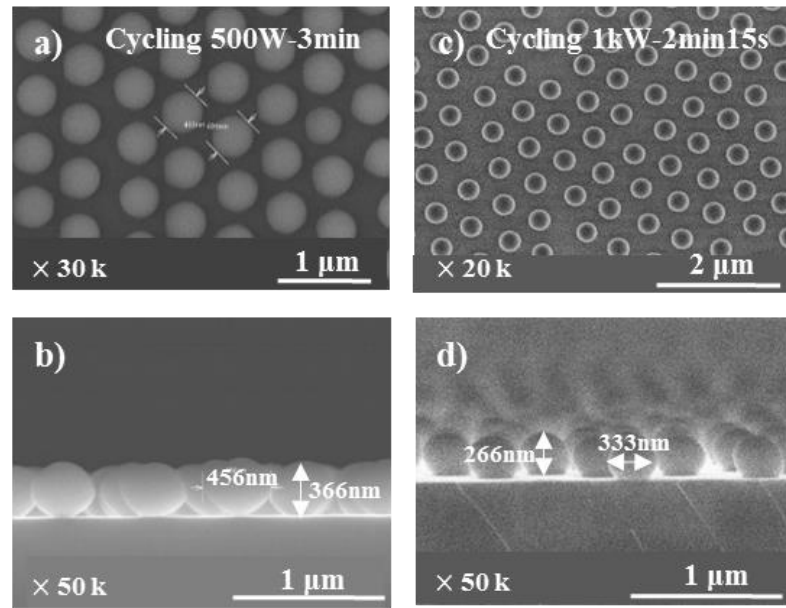


Figure 3.9: SEM images of 600 nm PS spheres etched by cycling plasma. 3 min under 500 W (a) top (b) cross section. 2 min 15 sec under 1 kW, (c) top (d) cross section.

From Fig. 3.9(a), we observed that the PS spheres exposed to the 3 min under 500 W cycling plasma are not strictly round, and have been etched to 77% of their initial diameter. On the other hand, the PS spheres exposed to 2 min 15 sec under 1 kW cycling plasma have maintained a round shape and have been reduced to 58% of their initial diameter. Surprisingly, the etch rate of the PS spheres under the cycling plasma is higher for both 500 W and 1 kW power compared to the continuous plasma as shown in Fig.3.8. This

might due to under the cycling plasma, the exposure time to oxygen radicals is longer. Comparing between Fig.3.9(d) and Fig.3.8(d), we observed that even though the PS spheres in Fig.3.9(d) are not completely melted and stick to the substrate, we do observed a larger area that is in contact with the substrate. We can conclude that the cycling plasma can mitigate the melting of the PS spheres.

To better demonstrate the effect of cycling plasma mode, we have carried out another set of experiments. The 800 nm PS spheres are exposed to oxygen plasma for 2 min 45 sec under 1 kW plasma power, applying both continuous and cycling mode. The top and cross section SEM images are shown in Fig.3.10.

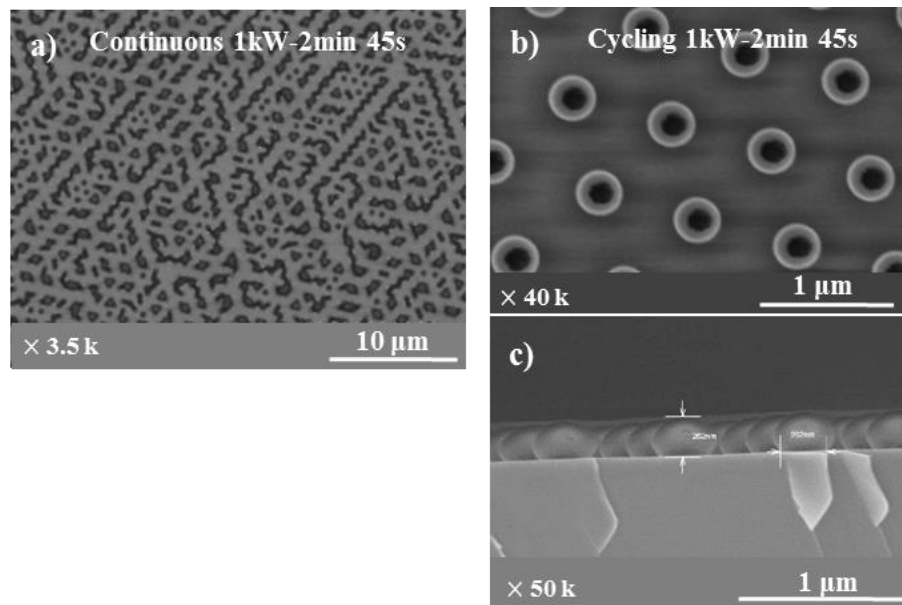


Figure 3.10: SEM images of 800 nm PS spheres exposed to oxygen plasma for 2 min 45 sec under 1 kW plasma. (a) continuous plasma, (b) cycling plasma top (c) cross section.

We observed that in Fig.3.10(a) the 800 nm PS spheres have melted and fused together, indicating a serious melting issue for the continuous plasma condition. In contrast, for the cycling plasma condition, the PS spheres were separated and maintained their round shape as shown in Fig.3.10(b), and were etched to 63% of their initial diameter. However, from the cross section SEM images as shown in Fig.3.10(c), PS spheres were still partially melted to the substrate and shown a contact area (around 200 nm wide) with the substrate. In order to better understand and further gain control over PS sphere melting/softening, the effect of different species, such as ions and oxygen radicals, in the oxygen plasma during PS sphere etching are next investigated.

3.3.3 Effect of Faraday cage shielding

In order to study the effect oxygen radicals independent of oxygen ions the during etching, as well as to better understand the reason behind the PS sphere melting, a stainless steel metal cage was used to reduce the ion flux towards the samples. The metal cage has a mesh transparency of 78 % and each metal wire is separated with a distance of 1 mm. Such etching set up using Faraday cage was previously studied by Byeong-Ok et al. [187]. In his work, the etching profile was greatly modified by the usage of the Faraday cage. To quantify the effect on the ion flux reduction, we firstly characterize the ion flux in a standard Ar plasma.

We carried out the measurement of the ion flux for a standard Ar plasma inside and outside the metal cage using a flat Langmuir probe with an area of 1 cm^2 [188]. The Ar plasma conditions were kept at 2 mTorr process chamber pressure and 500 W or 1 kW input plasma power. At 1 kW power, the ion current density generated by the probe outside the cage was 1.32 mA/cm^2 , while inside the cage ion current density dropped to 0.06 mA/cm^2 . At 500 W power, ion current density dropped from 0.6 mA/cm^2 to 0.03 mA/cm^2 when placing the probe from outside the cage to inside. The floating potentials were +3 V and +8 V for 500 W and 1kW power. From the results, we estimated that the metal cage can reduce the ion flux by around 95 %. Other than that, the radical flux is expected to be reduced by less than 20 %, which is deduced from the 78 % mesh transparency of the Faraday cage.

Subsequently, set of experiments was then carried out by placing PS sphere arrays inside and outside the metal cage, and exposing them to different oxygen plasma conditions. Fig.3.11 shows the SEM images of the 400 nm PS spheres on c-Si samples placed inside and outside the cage (continuous plasma for 2 min under 1 kW power).

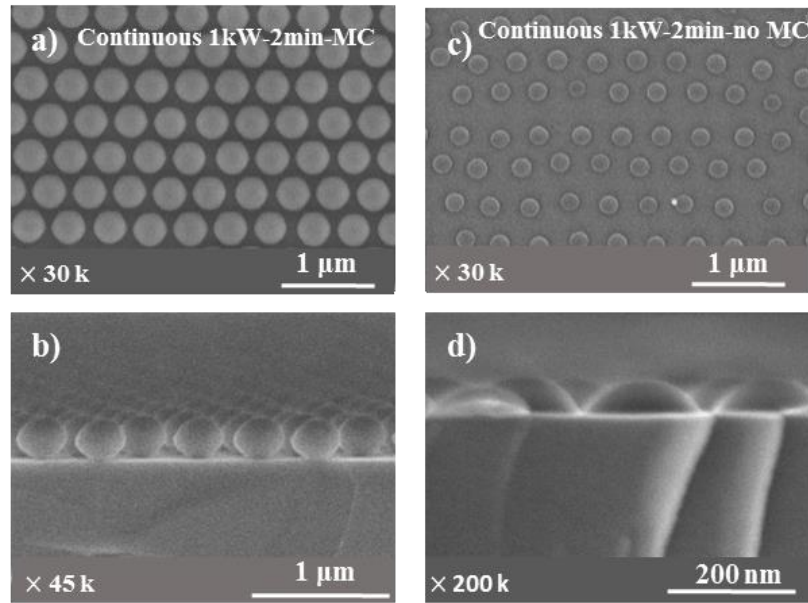


Figure 3.11: SEM images of 400 nm PS spheres etched for 2 min under 1 kW continuous plasma. Inside the cage (a) top (b) cross section. Outside the cage (c) top (d) cross section.

We observed from Fig. 3.11 that the PS spheres placed inside the cage are not melted, but PS spheres placed outside the cage are completely melted. Furthermore, from the top SEM images shown in Fig 3.11(a) and (c), the PS spheres placed inside the cage have a hexagonal shape after etching, and have been etched to 74% of their initial coverage area, while due to complete melting those on the outside of the cage have a round shape and have been etched to 24% of their initial coverage area.

We observed that, under the Faraday cage shielding, the etching rate of the PS spheres is greatly reduced. We repeated same experiment on 600 nm PS spheres, with a longer etching time. Firstly, we applied a 1 kW plasma power, continuously for 3 minutes inside the metal cage. The SEM images for the 1 kW experiment are shown in Fig.3.12.

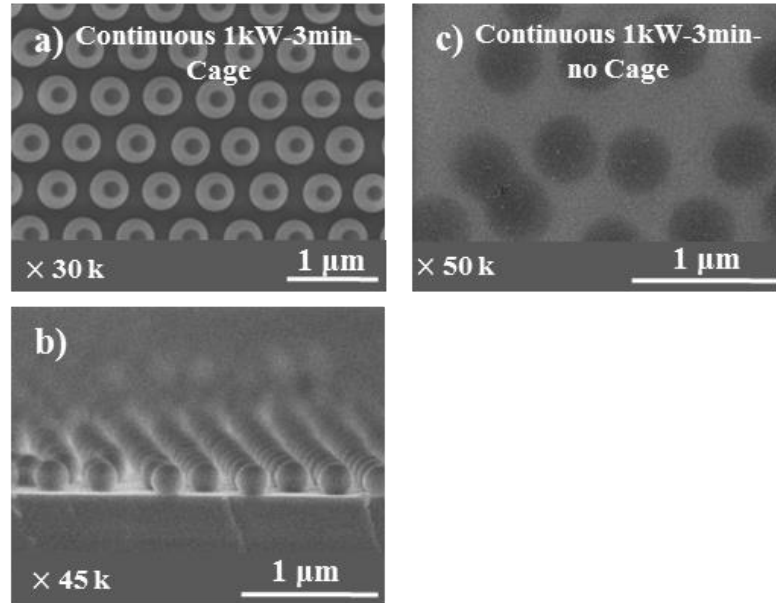


Figure 3.12: SEM images of 600 nm PS spheres etched for 3 min under continuous 1 kW plasma power. Inside the cage (a) top (b) cross section. Outside the cage (c) top.

From Fig.3.12, we observed that the PS spheres placed outside the cage are completely etched away, and PS spheres placed inside the cage are etched and not melted. PS spheres remain spherical and have been etched to 50% of their initial coverage area. From Fig.3.12(b), we observed that even though when PS spheres placed inside the cage they are not melted, the contact area between the PS spheres and substrates seems become larger, indicating a softening of the spheres during the process.

To further improve and to avoid such softening behavior, we reduced the etching power to 500 W and repeated the experiment. Other than the 3 min etching time as we did for the 1 kW etching power, we also tested 5 min etching time for 500 W under Faraday cage. As the lower plasma power will result in a slower etching rate, a longer etching time is preferred for an

observable etching process and hence better comparison. Fig.3.13 shows the SEM images for 600 nm PS spheres etched for 3 min and 5 min under continuous 500 W plasma power.

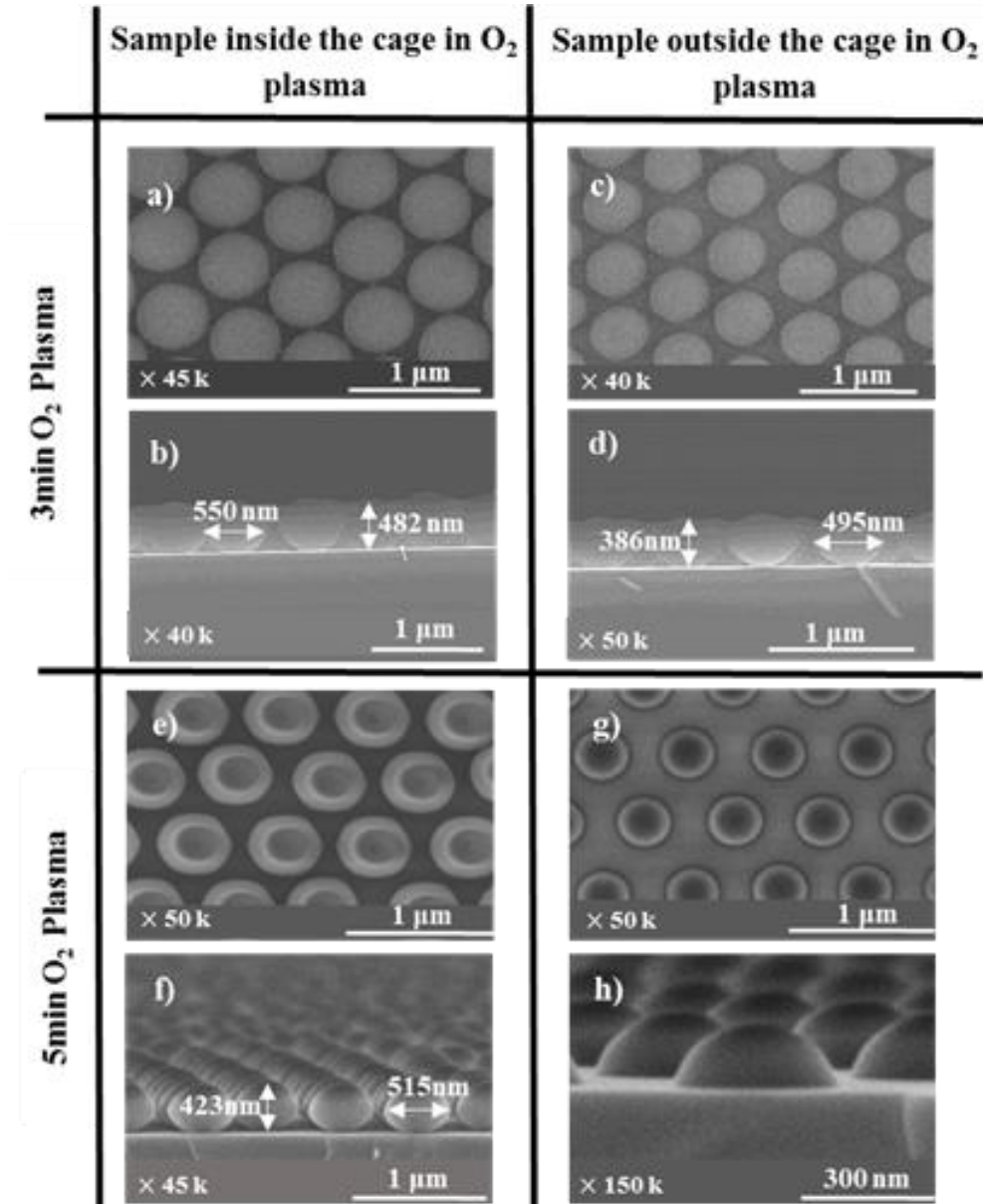


Figure 3.13: SEM images of 600 nm PS spheres etched under 500 W continuous plasma. 3 min plasma for sample inside cage (a) top (b) cross section, and for sample outside cage (c) top (d) cross section. 5 min plasma for sample inside cage (e) top (f) cross section, and outside cage (g) top (h) cross section.

We observed that for a decreased plasma power from 1 kW, as shown previously in Fig.3.12, to 500 W and etching time kept constant at 3 min, no melting is observed regardless of placing the sample inside or outside the metal cage, shown in Fig.3.13(a), (b), (c) and (d). However, we observed a decreased the etch rate. From Fig.3.13(a) and (c), we observed that the PS spheres inside the cage are etching to only 80 % of their original coverage area (comparing to 50 % reduction of the 1 kW case, as shown in Fig.3.12), and 65% for the spheres outside the cage. In addition, from the cross section SEM images, shown in Fig. 3.13(b), (d), and (f), we observe that the etch rate of the PS spheres in the vertical direction is faster than that in the lateral direction. This leads to in an oblate spheroidal shape of the PS spheres. We can observe such shape slightly more clearly outside the metal cage. The height of the spheres (now oblate spheroid) inside the cage is 482 nm (~80% of the original 600 nm height), whereas it is 386 nm (~64% of the original 600 nm height) outside the cage. In order to validate if the Faraday cage shielding can prevent the melting at 500 W plasma power even for a longer etching time, the plasma etching time was further increased to 5 min. Figure 3.13(e), (f), (g), and (h) show the SEM images. It is seen that the PS spheres placed inside the cage are not melted and have been reduced to 74 % of the initial coverage area. On the contrary, PS spheres placed outside the metal cage have melted and have been reduced to 58 % of the initial diameter.

Based on the SEM images and analysis above, we can draw some conclusions on the role of oxygen radicals during the etching process. Using a

metal cage prevents the PS spheres from melting, but at the cost of a reduced etch rate. We observed that by using the Faraday metal cage shielding, the vertical and lateral etching rate of the PS spheres are reduced by around 43 % and 49 % respectively. The observation is consistent with the conditions we applied: by using Faraday cage shielding, the total amount of etching radicals that will arrive on the sample is expected to be reduced by 20 % (78 % transparency of the cage) and 95 % fewer ions would arrive. We can conclude that the sample etching mainly comes from the oxygen radicals that arrive on the PS spheres.

Further experiments were carried out with the combination of cycling the plasma was then combined and the use of metal cage. 400 nm PS spheres were exposed to continuous or cycling plasma at different power levels: 3 min under 500 W and 2 min under 1 kW. The SEM images are shown in Fig.3.14.

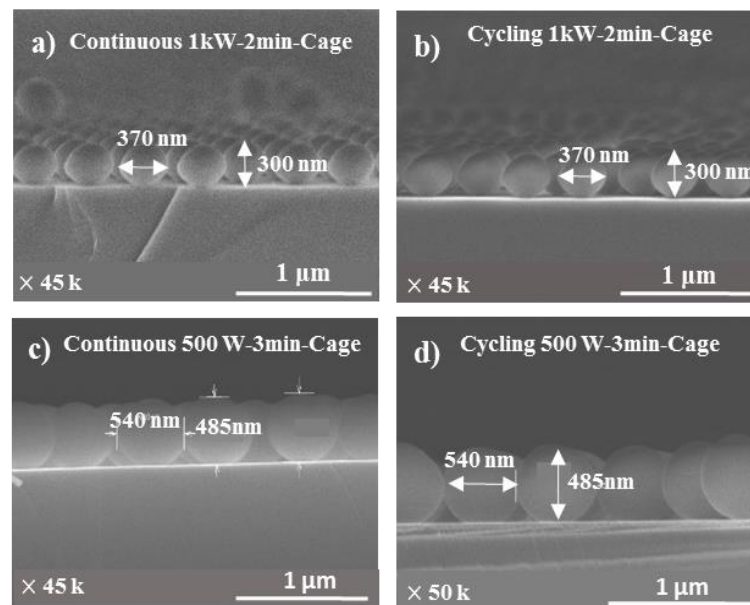


Figure 3.14: Cross section SEM images of 400 nm PS spheres etched inside metal cage. For 2 min under 1 kW plasma power, (a) continuous and (b)

cycling mode, and for 3 min under 500 W plasma power, (c) continuous and (d) cycling mode.

By comparing Fig.3.14(a) and Fig. 3.14(b), as well as Fig.3.14(c) and Fig.3.14(d), no significant difference in the etch rates is observed between the cycling and continuous modes, regardless of the input power. However, from section 3.3.2, we concluded that etching rate of the PS spheres under the cycling mode is faster compared to the continuous mode. This difference is probably due to the large metallic surface area provided by the metal cage that is placed closely with the sample induced an enhanced recombination of the oxygen radicals. Hence a fast drop of the oxygen radical concentration in the plasma-off phase will occur, which leads to less difference between the etching rate of cycling mode and continuous mode.

3.3.4 Effect of etching gas

In order to investigate the role of ions on PS sphere melting during the etching process, Ar plasma was applied after a moderate oxygen plasma etching process. Firstly, the PS spheres were slightly etched using oxygen plasma. Fig.3.15(a) and (b) show the top and cross section SEM images of the PS spheres after oxygen plasma etching. Secondly, we applied an additional 5 min Ar plasma at 500 W and placed the samples outside the metal cage. SEM images of the final samples are shown in Fig.3.15(c) and (d).

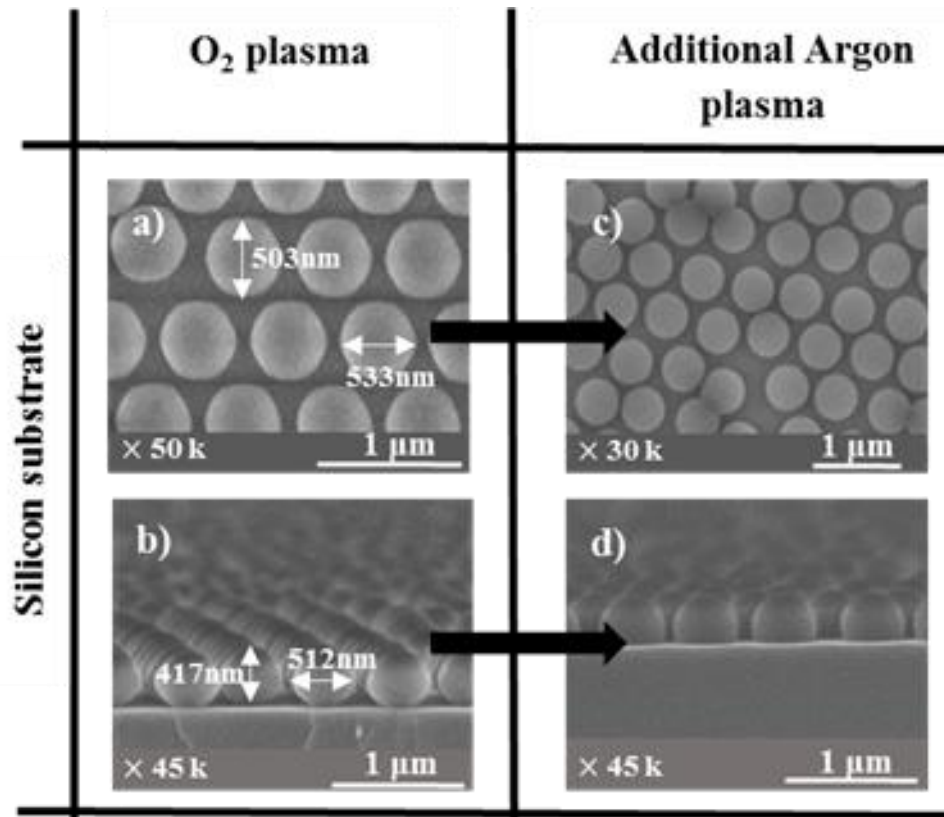


Figure 3.15: SEM images of 600 nm PS spheres etched for 5 min under 500 W continuous plasma inside metal cage. (a) top and (b) cross section. SEM images after additional Ar plasma for 5 min under continuous 500 W plasma power outside metal cage (c) top (d) cross section.

From Fig.3.15, although the PS spheres are not further etched by the additional Ar plasma, PS spheres are further melted and have a larger contact area with the silicon substrate, as shown in Fig.3.15(d). Some of the adjacent PS spheres have fused together, as shown in Fig.3.15(c). This further proves that the ions are the main cause for the PS spheres heating, which can eventually end up with PS softening and even melting.

3.4 Shape Evolution of PS Spheres

In this section, the shape evolution of PS spheres during oxygen plasma etching is described in detail. We described different characteristic shapes that observed from the SEM images.

At the early stage of oxygen etching, a hexagonal shape is observed from the top view, both inside and outside the Faraday metal cage. This shape is presumably due to a “shadowing effect” by adjacent PS spheres, i.e. at the point of the PS spheres which is in contact with another, the arrived oxygen radical flux is lower, and at the point of the PS spheres which is far from another, the arrived oxygen radical flux is higher. By plotting the aspect ratio (ratio of the largest width to smallest width when viewed from top SEM images), we quantify such evolution for all 600 nm PS spheres as a function of oxygen plasma etching time, as shown in Fig.3.16, and PS sphere etching percentage, as shown Fig.3.17. It should be noted that if the PS spheres take an ellipsoid shape, a large value of aspect ratio will also be present in the result. We have indicated the different shapes on the figures with highlights.

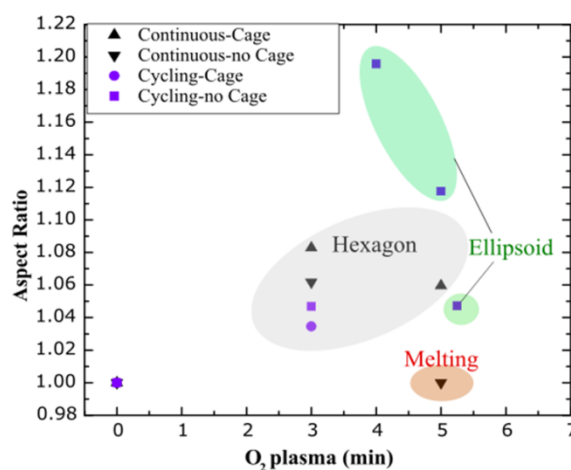


Figure 3.16: Aspect ratio between largest and smallest width observed on top SEM images as a function of oxygen plasma etching time under 500 W plasma power

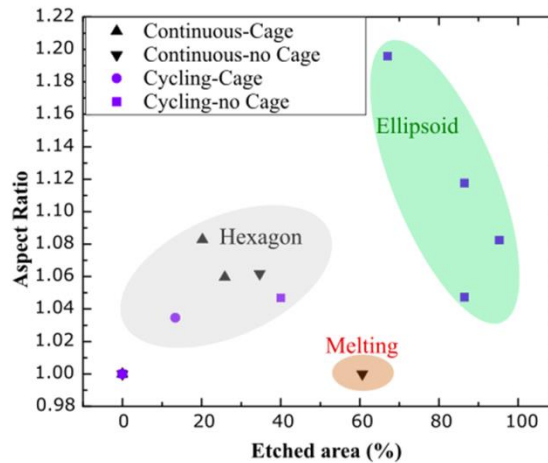


Figure 3.17: Aspect ratio between largest and smallest width observed by top view SEM images as a function of PS sphere etched area in percentage under 500 W plasma power.

We observed that for all cases, when a 500 W plasma power is applied (irrespective of continuous or cycled mode, in the presence or absent of cage), the hexagonal shape eventually disappears after a long etching time (> 3 minutes). Such observation is consistent with the proposed “shadowing effect”. After the PS spheres are been etched and to a point that are sufficiently away from each other, the shadowing effect becomes negligible.

We also carried out two sets of experiments performed on 600 nm and 800 nm PS spheres to investigate the origin of the ellipsoid shape and the condition minimized such shape. For these two sets of experiments, we use

500 W oxygen plasma power in cycling mode, with the plasma etching time up to 5 min 30 sec. The top SEM images for the 600 nm PS spheres are shown in Fig.3.18 (a) to (d), and for the 800 nm PS spheres are shown in Fig.3.19 (a) and (b).

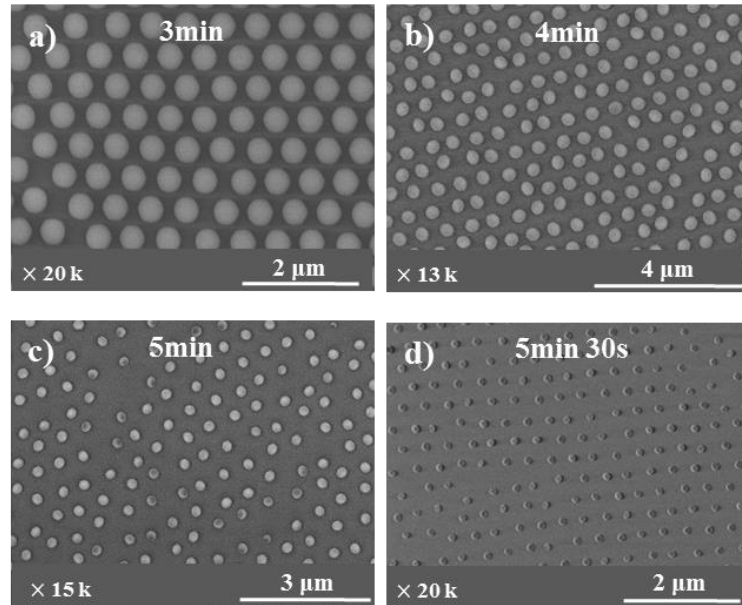


Figure 3.18: Top view SEM images of 600 nm PS spheres etched under cycling 500 W plasma. For (a) 3 min, (b) 4 min, (c) 5 min, and (d) 5 min 30 sec.

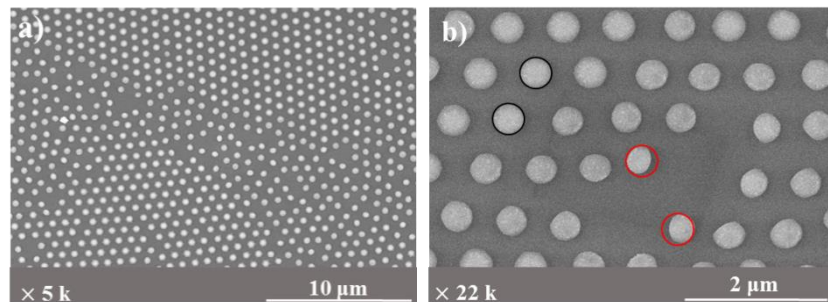


Figure 3.19: Top view SEM images of 800 nm PS spheres etched for 5 min 15 sec under cycling 500 W plasma. At (a) low magnification and (b) high magnification.

From the above figures, we observed both spherical and ellipsoid shapes. Such ellipsoid shapes have been previously reported [149], [189]. They were attributed to PS spheres shifting position after toppling over. In Fig.3.19 (b), we can see that the ellipsoid shapes (marked in red, while spherical shapes are marked in black) are more likely to appear at the gap between two domains of periodical arranged PS spheres. This might due to asymmetric etching of the PS spheres under a denser flux of oxygen radicals between the gaps of two ordered domains. Such asymmetric flux could disturb the balance of a standing PS sphere; hence the toppling over of PS spheres are more like to occur.

To further investigate the toppling of the PS spheres, we repeated the etching process with the same conditions on 800 nm PS spheres, but for a slightly shorter etching time (4 min and 5 min 15 sec). Fig.3.20 shows the SEM images of the etched samples.

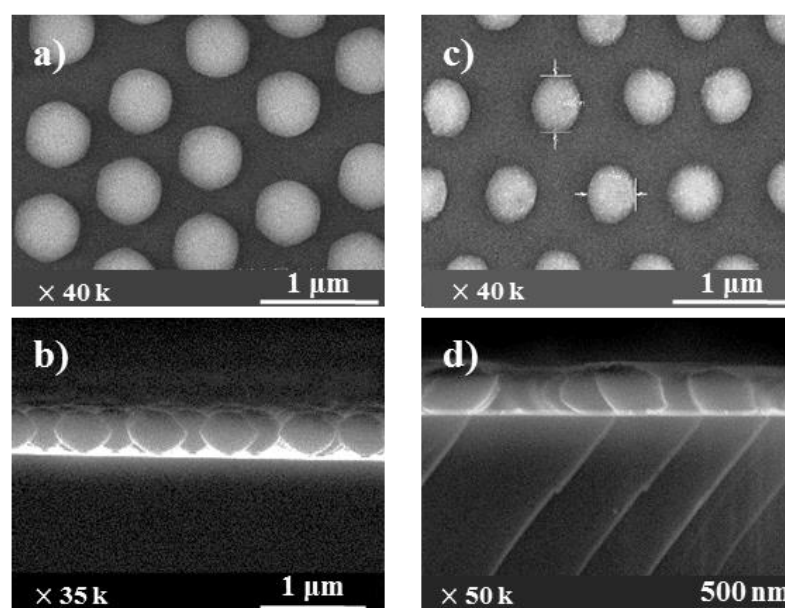


Figure 3.20: SEM images of 800 nm PS spheres etched under cycling 500 W plasma. For 4 min (a) top (b) cross section, and for 5 min 15 sec (c) top and (d) cross section.

After 4 min of oxygen plasma, the PS spheres have adopted a hexagonal shape, as shown in Fig.3.20 (a), and a diamond-like shape with small contact area with the substrate, as shown in Fig.3.20 (b). From Fig.3.20 (c) and (d), we observed that some of the PS spheres topple over after an extended etching time (5 min 15 sec). This toppling of a PS sphere is more likely to occur under a long plasma etching time as the footprint of the diamond-like shape becomes very small. The balance of the standing PS spheres will be disturbed. The electrostatic force between the charged PS spheres and the grounded silicon substrate will become more significant. As the result, toppling over of the PS spheres is more likely to happen.

We didn't expect to observe diamond-like shape of the PS spheres, as shown in Fig.3.20 (b). Such shape appeared even more distinguishable when the monolayer of PS spheres array were formed on a c-Si substrate covered with ~120 nm of thermally grown SiO₂. A side view SEM image is shown in Fig.3.21.

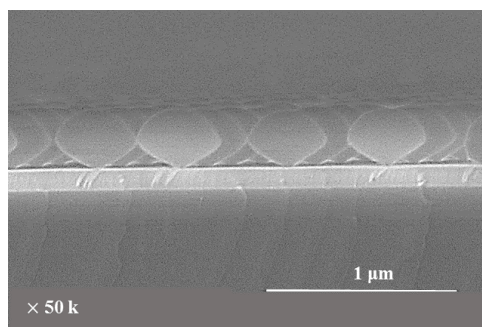


Figure 3.21: Cross section SEM image of 600 nm PS spheres etched for 3 min under cycling 500 W plasma power.

The formation of such diamond-like shape might be explained as follows. During the plasma turned on phase, the PS spheres have reached their glass transition temperature, softened and are pulled up towards the plasma due to electrostatic forces. During the plasma turned off period, due to release of the heat to the ambient, the temperature of the PS spheres will drop below to the glass transition temperature and PS spheres solidify again. The reason behind the electrostatic force acting on the PS spheres might be due to, the negatively charged PS spheres are pulled by the electric field in the plasma sheath region, or due to repulsion between the PS spheres and the substrate as both of them have become negatively charged under active plasma. The cycling plasma mode can effectively prevent the PS spheres to approach their glass transition temperature, hence softening of the PS spheres are effectively avoided and such diamond-like shape are formed.

To summarize the effect of different plasma conditions in shaping the PS spheres during etching, we showed that cycling plasma mode enabled almost complete etching of the PS spheres without any melting effect, and hence retained the patterning capability of the sphere array. We therefore challenged the limits of the smallest size obtainable under such etching configuration. For applications such as point contact solar cells, where an extremely small openings are needed [190], it is important to push the limit of the final PS spheres size to an extreme and yet retain their periodicity and

patterning capability. A cycling oxygen plasma at 500 W was used for the etching process. The results of 400, 600 and 800 nm PS spheres etched area with respect to the etching time are presented in Fig.3.22.

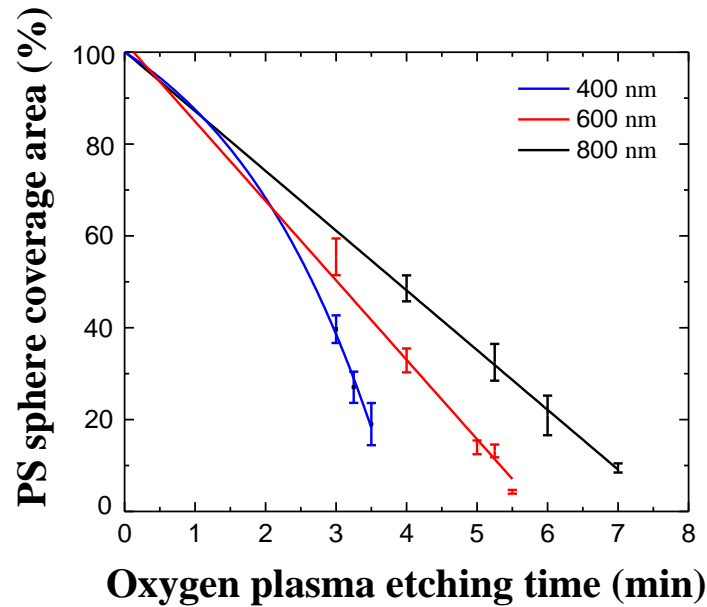


Figure 3.22: Coverage area of PS spheres of 400, 600 and 800 nm PS spheres as a function of etching time at cycling 500 W plasma power.

As observed in Fig.3.22, we successfully reduced the covered area of the 400, 600 and 800 nm PS spheres down to 19 %, 4 %, and 9 % of their initial coverage area, respectively, without any melting. In terms of the value in diameter, the 425, 607 and 784 nm PS spheres were etched to the diameters of 185 ± 21 nm 125 ± 17 nm, and 241 ± 13 nm, respectively. The SEM images of the etched PS spheres are shown in Fig.3.23.

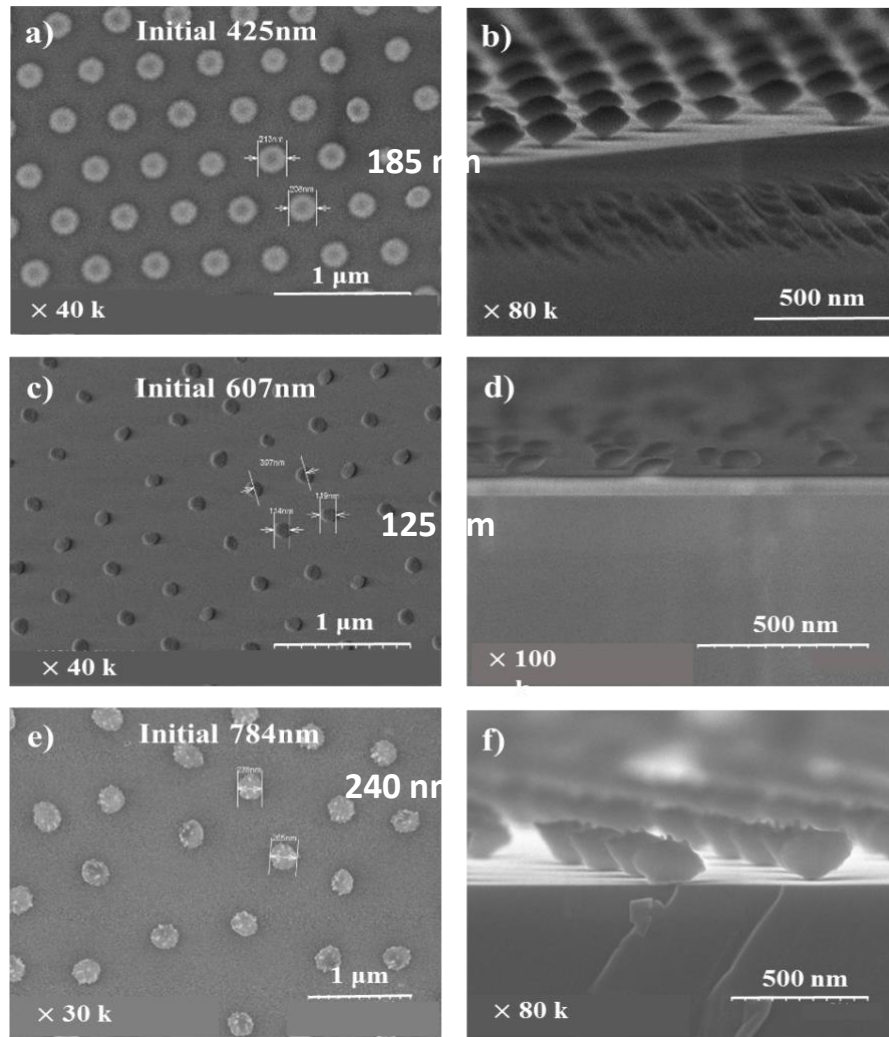


Figure 3.23: SEM images (a), (b) of 400 nm PS spheres etched to 43.6% of their initial diameter, (c), (d) 600 nm PS spheres to 20%, and (e), (f) 800 nm PS spheres to 30%.

In Figure 3.23, we observed spherical shapes of the final PS spheres after etching from the SEM top view images. For the 800 nm PS spheres after etching, the top surface of the spheres appeared rough, as shown in Fig.3.23 (e) and (f). Such rough surfaces are expected after a long plasma treatment. This is due to the the etch rates are different for the amorphous and crystalline phases of polystyrene, as studied in [191]. Even with different plasma etching conditions and sources proposed by other research groups,

the PS sphere surface roughness will be present [144], [149], [192]. From the side view SEM images, the 400 nm PS spheres have adopted a standing diamond-like shape, and the 600 and 800 nm PS spheres have adopted a toppled over ellipsoid shape.

3.5 Conclusion

The etching of PS spheres using MDECR oxygen plasma has been presented in this chapter. The PS spheres are melted and wetted on the silicon substrate under continuously applied high plasma power of 1 kW. This effect could be mitigated by reducing the plasma power, using plasma cycling mode, or by using a Faraday cage for ion shielding. We concluded that the energetic ion bombardment is the main reason for PS spheres heating and melting.

A hexagonal shape was observed from top view SEM images at the early stage of the etching process, regardless of the deployed plasma conditions. This is due to the “shadowing effect” of oxygen radical diffusion. An oblate spheroidal shape was also observed from the SEM side view images, which aroused due to higher vertical etching rate comparing with horizontal etching rate. We concluded that the oxygen radical is the main reason for PS spheres etching.

For longer etching time under cycling plasma mode, which can effectively prevent complete PS melting, a PS sphere toppling effect was observed,

leading to the regularity of the periodic array of PS spheres being distorted. By first applying a short duration of the etching process that will partially melt or soften the PS spheres, followed by a longer duration of the etching process that will prevent PS spheres from melting, we can effectively avoid toppling of the PS spheres. As a result, diamond-like shapes of the PS spheres as seen from the side are more likely to be formed.

Last but not least, we successfully reduced the areal coverage down to between 4 to 19 % of the initial covered area using 400, 600 and 800 nm PS spheres by using the optimized etching condition: 500 W plasma power with cycling mode. This was achieved without losing the patterning capability of the PS sphere arrays. By pushing the limit of the smallest PS spheres obtainable, and also with the added controllability of the periodicity of the PS spheres, various applications using PS spheres patterning can benefit from our research results, e.g. point contact solar cell.

In terms of route to scale up for a successful integration of nano-structuring technique into the mass production favored roll-to-roll process, PS sphere assisted lithography might not be the best choice. However, PS sphere assisted lithography have the potential to scale-up by applying Langmuir Blodgett system. But in terms of the roll-to-roll process, nano spray of the PS solution onto the substrate, formation of the single sphere packed thin aquatics film, followed by low temperature fast drying could be a solution.

Chapter 4. Nanostructured Back Reflectors produced using Polystyrene Assisted Lithography for Enhanced Light Trapping in Silicon Thin Film Solar Cells

In this chapter, we study light trapping in hydrogenated amorphous silicon thin film solar cells fabricated by plasma-enhanced chemical vapor deposition on various nanostructure back reflectors. The back reflectors are patterned using polystyrene assisted lithography. We aim to improve the light trapping performance of the solar cell with different nanostructured back reflectors. Firstly, we will introduce the front scatterer and back reflector concepts in silicon thin film solar cell. Previous studies on different nanostructured Ag/ZnO back reflectors for silicon thin film solar cells will be summarized in detail. Subsequently, fabrication process of our polystyrene sphere patterned back reflectors will be introduced. After that, the optical properties of single and double sphere sized patterned back reflectors will be discussed. We will also present the solar cell performance based on different back reflectors. By mixing two sizes of different PS spheres during the patterning step, we further improve the power conversion efficiency (PCE) by introducing more randomized Ag nanostructures in the BRs. An initial 8.79 % PCE has been achieved with only ~230 nm of a-Si:H active layer. Lastly, conclusions regarding the silicon thin film solar cell light trapping improvements with our polystyrene sphere patterned back reflector will be presented.

4.1 Introduction and objectives

Photovoltaic devices fabricated by plasma-enhanced chemical vapor deposition (PECVD) of hydrogenated amorphous silicon thin films at low temperatures (around 150°C) on various nanostructured back reflector (BR) substrates will be discussed. There are two forms of silicon thin film solar cells: hydrogenated amorphous silicon solar cells (a-Si:H) and hydrogenated microcrystalline silicon solar cells (μ c-Si:H). Compared to wafer based crystalline silicon solar cells, such photovoltaic devices possess advantages including lesser material usage, compatible with roll to roll processes on flexible substrates, robustness in controlling the device shape and material properties, etc. Compared to other thin film solar cell technologies which rely on the less abundant and in some cases toxic materials, such as CdS, silicon thin film technologies are preferred from the perspective of a sustainable industrial development and an environmental friendly solar energy collection process.

However, due to their short minority carrier diffusion length, the thickness of silicon thin film is limited to a few hundreds of nanometers for a-Si:H and a few micrometers for μ c-Si:H solar cells. To improve the performance, effective light trapping mechanisms have been extensively researched during the last decade [193], [194]. Various nanostructures incorporated into silicon thin film solar cells have shown great enhancement in light absorption. With nanostructures being incorporated into the device, extended light travelling path were introduced into the active layers by additional wave guide mode and far field scattering due to the nanostructures' geometrical arrangement

and material properties, as well as by near field scattering due to localized surface plasmonic effect of the metallic nanostructures. The combined effect allows enhanced light absorption, hence improved photocurrent collection. Traditional nanostructures were created based on naturally grown surface nanostructures of transparent conductive oxide (TCO) [195], e.g. sputtered ZnO, or chemically etched TCO surface structures [196], e.g. commercial ASahi substrate. Depending on the location of the nanostructure with respect to incident light, recent literatures in this field of study could be roughly divided into two categories, front scatterers or back reflectors (BRs) [19].

4.1.1 Front scatterer and back reflector for silicon thin film solar cell

Aiming at its best performance, a typical front scatterer utilizes metallic nanostructures, which induces a plasmonic near field enhancement effect [20]. A typical back reflector utilizes metallic or metal/dielectric nanostructures, which produce a far field scattering effect [21]. For front scatterers, nanostructures or nanoparticles (NPs) are placed at the front side of the solar cells for the purpose of forward light scattering into the active material below. Surface nanostructures like silver/gold NPs [197][198], SiO₂ nanospheres [199], TiO₂ nanostructures [200], Si nanowires [102], etc. were intensively researched and the experimental results obtained have proven to be effective in enhancing light trapping performance. For back reflectors, nanostructures are placed at the back side of the solar cells for the purpose of backward light scattering into the active material above [201], [202]. Under the context of Si thin film solar cell, both metal/dielectric photonic periodic nanostructured BRs

[193], [203], [212], [204]–[211], as well as metal/dielectric random nanoparticle or random nanoscale rough surface induced diffusive BRs [21], [201], [213]–[218] are the two main research directions for the back reflectors.

Among the above two methods, metallic or metallic/dielectric nanostructures are of intense research interest due to their pronounced plasmonic enhancement effect [3], [4], [28]–[33]. Such plasmonic enhancement is achieved through various mechanisms falling under three main categories: near field enhancement, far-field scattering, and charge carrier or resonant energy transfer [19]. Due to limited publication and knowledge, the third category will not be discussed in this work. A near field enhancement of metallic nanostructures refers to an intensive electromagnetic field generation at the metallic surface after the incident photon metal interaction. Such effect is often referred as localized surface plasmon resonance (LSPR) [197], [207] generation. However due to their exponentially decayed field intensity, such enhanced field intensity can only extend several tens of nanometres from the surface. To utilize the near field enhancement effect, the light absorbers are usually in direct contact with the metallic nanostructures for maximized absorption enhancement. Hence most of the publication on near field enhancement falls under front scatterer structures. On the other hand, depending on the particle size (typically >50nm) and its geometry, metallic or metallic/dielectric nanostructures can effectively backward scatter the incident photon as well [198], [223], [224]. The absorption enhancement of such method arises from multiple scattering events when photons travel within the absorber and interact with the nanostructures. The effective light travelling

path is significantly increased, hence more likely those lower energy photons will be absorbed. Due to above mechanism, this scattering effect is often referred to far field effect [225], [226], which falls under the category of back reflector structures. To utilize the plasmonic enhancement effectively, one needs to take special care of the parasitic absorption of the nanoparticles. The trade-off between maximized scattered photons and minimized optical losses of the metallic or metallic/dielectric nanoparticles should always be considered and the nanostructures should be carefully designed to achieve this. Regardless of which method is being deployed, for a light trapping mechanism to be effective, certain criteria must be first met. It should be able to enhance all photon absorption across the entire wavelength range where the solar cell is active and should be effective at different angle of incidence. In the perspective of manufacturing capability, it should be compatible with the existing solar cell fabrication processes, low cost and offer additional improvements over the existing methods.

4.1.2 Nanostructured Ag/ZnO back reflector

In this work, we study a-Si:H solar cells fabricated by PECVD, incorporating different semi-periodic nanostructured back reflectors (BRs). The BRs are fabricated by applying polystyrene (PS) sphere assisted lithography [227] to pattern Ag nanostructures, followed by sputtered Ag and ZnO:Al as the reflective layer and optical spacer respectively, hereafter referred as polystyrene sphere patterned (PSP) BRs. The use of BRs instead of front scatterers prevents metallic contamination and the cost effective PS sphere

assisted lithography allows better controllability of the Ag nanostructure formation. Besides, it also bypasses the high temperature annealing step that is usually required for the formation of top surface Ag nanostructures starting from a thin Ag film. Hence it is fully compatible with the low temperature PECVD fabrication process.

4.2 Fabrication and characterization of nanostructured Ag/ZnO back reflectors and back reflector solar cells

4.2.1 PS sphere patterned back reflector

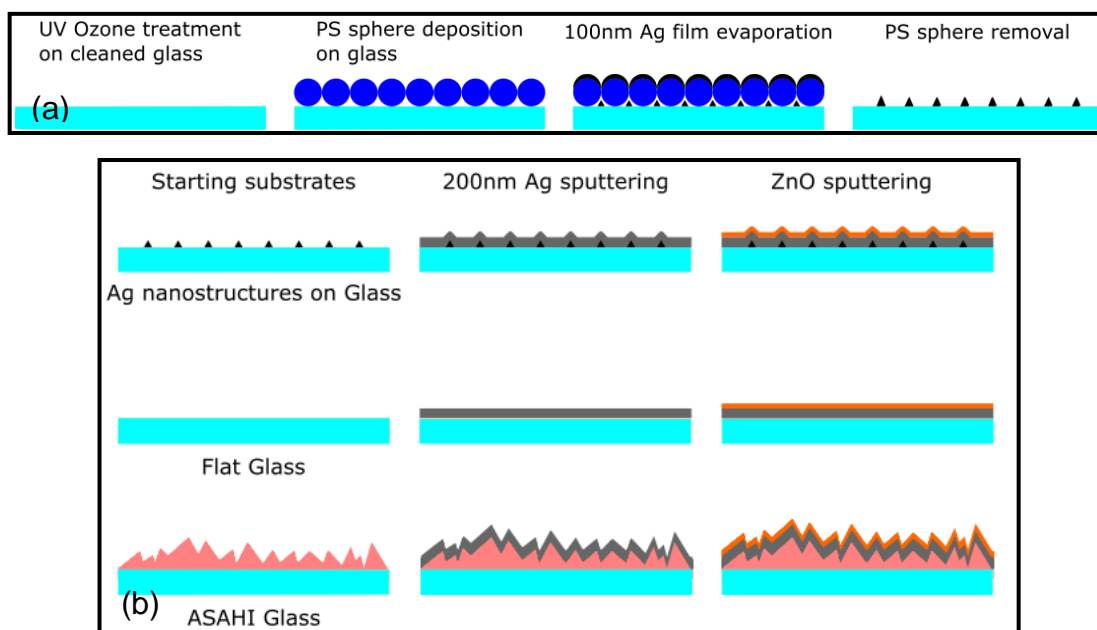


Figure 4.1: (a) Fabrication process for Ag nanostructure on glass.
(b) Fabrication process for back reflectors.

The PS spheres used in this work were an aqueous monodispersed suspension of 5 w.t. % obtained from microparticles GmbH with nominal diameters of 425 ± 10 nm, 607 ± 15 nm and 784 ± 23 nm (thereafter referred to as 400, 600 and 800 nm PS spheres). The solutions were uniformly mixed with methanol as the spreading agent in 1:1 volume ratio. Prior to the PS sphere monolayer transfer, Corning glass was cleaned with acetone, isopropanol and de-ionized (DI) water in ultrasonic bath, followed with a 10 min UV-Ozone treatment to keep the surface hydrophilic. After a monolayer of PS spheres had transferred on Corning glass using the floating transfer technique [183], a 100 nm layer of Ag was thermally evaporated on top. For a

complete PS sphere removal and yet to retain the Ag nanostructures formed on the glass, a low power ultrasonic bath in toluene was applied for 20 min, followed with 10 min isopropanol and DI water ultrasonic bath for a complete removal of any organic solvent residue. The overall fabrication process of Ag nanostructures is schematically shown in Fig. 4.1 (a).

After the above steps, a set of cleaned Ag nanostructures on glass, flat glass and ASAHI glass have been sputtered with 200 nm of Ag using an RF (13.56 MHz) magnetron system under the following process conditions at room temperature: argon flow rate of 41 sccm, RF power of 50 W and process pressure of 5.7×10^{-3} mbar. Without breaking the vacuum, 100 nm of ZnO:Al was sputtered under the following process conditions at room temperature: argon flow rate of 30 sccm, RF power of 250W and process pressure of 4.3×10^{-3} mbar. The fabrication process carried out on the three substrates is schematically shown in Fig.4.1 (b). The Ag layer is protected by ZnO during the sputtering process without breaking the vacuum, i.e. in a single pump down process. After the Ag/ZnO sputtering process, the substrate was transferred into the PECVD vacuum chamber for a-Si:H deposition. The ZnO layer is protected by the top a-Si:H layers without long exposure time in the ambient environment. ZnO is used as its material properties render it suitable as an optical spacer with appropriate n and k values, as well as an electrical spacer with lower contact resistance and good buffer between a-Si:H and the metallic surface. The flat and ASAHI glass substrates are used in our study as references for comparison with the performance of the PSP BRs substrates.

4.2.2 Silicon thin film solar cell

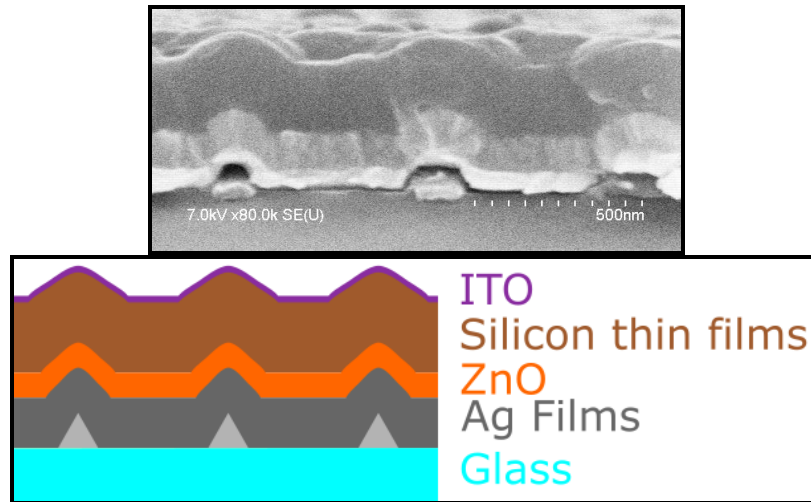


Figure 4.2: SEM image and schematic image of the cross section of a solar cell device.

Amorphous silicon thin films were deposited in a 13.56 MHz radio frequency (RF) PECVD system [228]. Three plasma chambers sharing the same vacuum pump were used for separate n-type, intrinsic and p-type a-Si:H deposition to avoid any cross contamination. Firstly, a 25 nm thick n-type microcrystalline silicon oxide layer was deposited on the BR [229]. Without breaking the vacuum, ~230 nm of intrinsic amorphous silicon layer has been deposited using a SiH_4/H_2 plasma, followed by a 25 nm thick p-type amorphous silicon carbide layer. Finally, a 80 nm thick indium tin oxide (ITO) was deposited to form the top contacts and to define cells with an area of 0.126 cm^2 . Such photovoltaic device is often referred to n-i-p solar cell [230]. A schematic image of the side view of the device and a corresponding SEM image acquired using Hitachi S-4700 Scanning Electron Microscope is shown in Fig.4. 2.

4.2.3 Characterization techniques

The current density-voltage (J - V) characteristics of the solar cells were measured under AM1.5G illumination with a commercial solar simulator (Oriel AAA), calibrated using a crystalline Si reference cell. Total and diffused reflectance was measured using a Perkin-Elmer Lambda 950 spectrometer with a 150 mm integrating sphere and an InGaAs detector.

4.3 Optical characterization of PS sphere patterned back reflectors

In this section, optical measurement results of pure Ag on glass, flat Ag/ZnO BR and polystyrene sphere patterned (PSP) BRs patterned using single PS sphere as well as double PS spheres will be discussed first. Following that, $J-V$, external quantum efficiency (EQE) and optical absorption ($1 - R_{total}$) results of the solar cells fabricated using different kinds of BRs will be compared and discussed. In addition, comparison between one of the PSP BR solar cells and solar cells fabricated using the commercial nanostructured ASAHI BR will be presented.

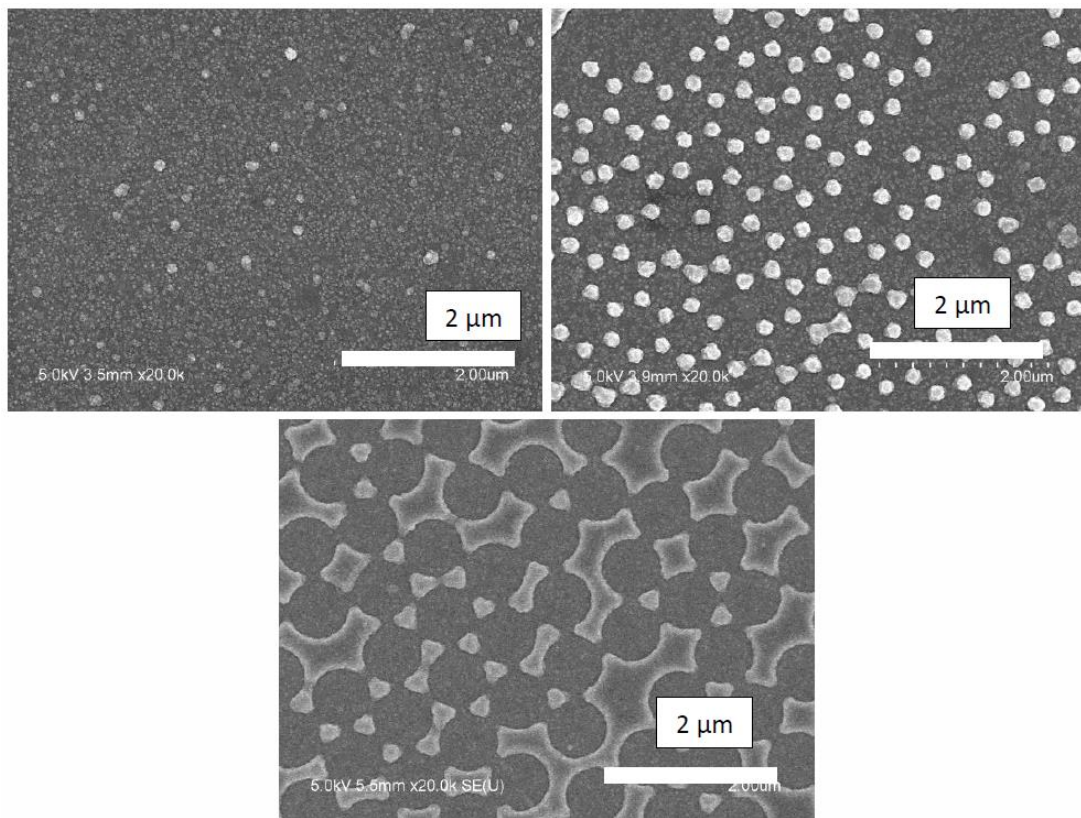


Figure 4.3: SEM images of 400, 600 and 800 Polystyrene Spheres assisted Patterned BRs.

Fig. 4.3 shows the SEM images of 400, 600 and 800 PSP BRs and Fig. 4.4 shows the total and diffused reflectance as well as reflectance HAZE of the BRs. The reflectance HAZE was calculated as the ratio of diffused reflectance to total reflectance.

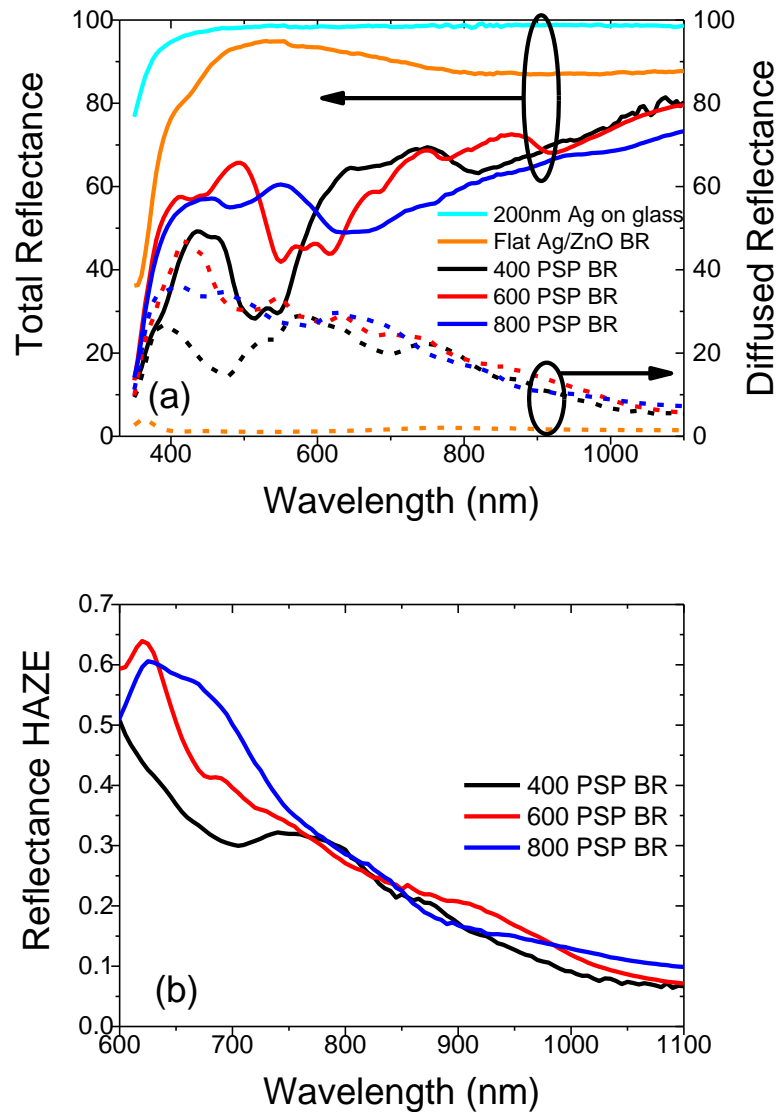


Figure 4.4: (a) Total and diffused reflectance and (b) reflectance HAZE results of 400, 600 and 800PSP BRs.

As one of the most important parameters to characterize the quality of a back reflector, total reflectance and diffused reflectance measurements were

carried out on the BRs prior to the silicon thin film deposition. In general a good BR should provide low optical/parasitic absorption, i.e. high in total reflectance and high scattering capability across the entire wavelength range where the solar cell is active. As expected, a pure 200 nm of Ag film on glass provides a highly reflective surface from 350 nm to 1100 nm wavelength range, with minimum absorption at shorter wavelength. From Fig. 4.4(a), we observe that when 100 nm ZnO were deposited on top of Ag, a strong absorption appears from 350 nm to 500 nm and a weak absorption also appears from 800 nm to 1100 nm. For the shorter wavelength case, this is due to the rough Ag/ZnO interface which introduces localized plasmonic absorption at the nano-protrusions on the Ag surface [231]. For the longer wavelength case, this is due to the free carrier absorption in the thick ZnO layer [232]. For flat Ag/ZnO back reflector, the diffused reflectance approaches zero, which indicates that there is no light trapping capability provided by such BR. For the PSP BRs the optical performances were more complex as presented below.

4.3.1 Single sphere size patterned back reflector

From Fig.4.3 we can clearly see an increasing size of Ag/ZnO nanostructures when larger PS spheres were used for patterning. In the ideal case, all PS spheres are closely packed; a larger sphere size will result in a larger sphere to sphere adjacent opening. Hence, larger Ag nanoparticles will be formed, as well as larger Ag/ZnO nanostructures after 200 nm Ag and 100 nm ZnO sputtering. From the total reflectance results in Fig.4.4(a), we observed that

with an increasing Ag/ZnO nanostructure size, localized BR reflectance minima red shift from 500-550 nm to 550-610 nm to 600-700 nm ranges. The observation is consistent with existing literature showing that the localized plasmonic absorption range of Ag nanoparticles depends on their size, which affects their light scattering properties as well [21]. By utilizing the Mie theory formalism, S. Morawiec *et al.* calculated the normalized scattering and absorption of a single Ag particle embedded in different media [233]. They predicted an increasing red shifting and broadening of the plasmonic modes of the Ag nanoparticles when embedded in glass/air, Air/ZnO and Si/ZnO effective medium. However, the same theory might not be appropriate to explain the optical properties of our PSP BRs. In S. Morawiec's work, they did not consider the inter-particle interactions on optical properties of the BRs. For our PSP BRs, with the close to visible wavelength inter-particle distance, as well as the semi-periodic arrangement of the metal/dielectric nanostructures, we would expect more light scattering in the system, hence a stronger light trapping capability of the PSP BR solar cells.

From Fig.4.4(a), we observe similar magnitude of the diffused reflectance but different optical absorption for three samples. It should be noted that due to high absorption, not only the total amount of reflected light is reduced, the amount of light that is been diffusively reflected is reduced as well. In addition, for a-Si:H solar cells, light trapping performance is more critical at longer wavelength range of 600 – 800 nm. In the above range, we observed that even though the 400 PSP BR has the lowest optical absorption, it also provides the lowest diffused reflectance, hence weakest light scattering. For

800 PSP BR, even with the highest optical absorption, still it provides the highest diffused reflectance, hence strongest light scattering. Reflectance HAZE plotted in Fig.4.4(b) from 600 nm wavelength onwards further magnifies the above description. We expect for the silicon thin film solar cells fabricated on 800 PSP BRs will have the best light trapping performance. Hence outperform solar cells fabricated on 400 PSP BRs and 600 PSP BRs.

4.3.2 Double sphere size patterned back reflector

To further improve our PSP BR substrates for light scattering, mixtures of two PS spheres sizes were used for patterning. By mixing PS spheres with two different sizes, we introduce a more random arrangement of Ag nanostructures. Intuitively, incoming photons would have a higher chance to be diffusively reflected. During the solution preparation, 400 nm and 600 nm PS spheres with 60 % : 40 %, 50 % : 50 % and 40 % : 60 % volume ratio mixtures, 600 nm 800 nm with 70 % : 30 % and 50 % : 50 % volume ratio mixtures and 400 nm and 800 nm PS spheres with 90 % : 10 % volume ratio mixtures were prepared and BRs were fabricated. They are referred as 4664, 4655, 4646, 6873, 6855 and 4891 PSP BR respectively. To characterize the PS assemble quality and morphology, Fig.4.5 shows the SEM images of different double PS sphere monolayers and 4655 PSP BR. We can see that homogenous mixtures of PS spheres can be obtained, especially when the two sizes are close to each other and when the mixture volume ratio is 50 % : 50 %. Any imbalance in volume ratio or sphere size leads to formation of

small domains of periodic packing of single size PS spheres, for example 6873 and 4891 monolayers.

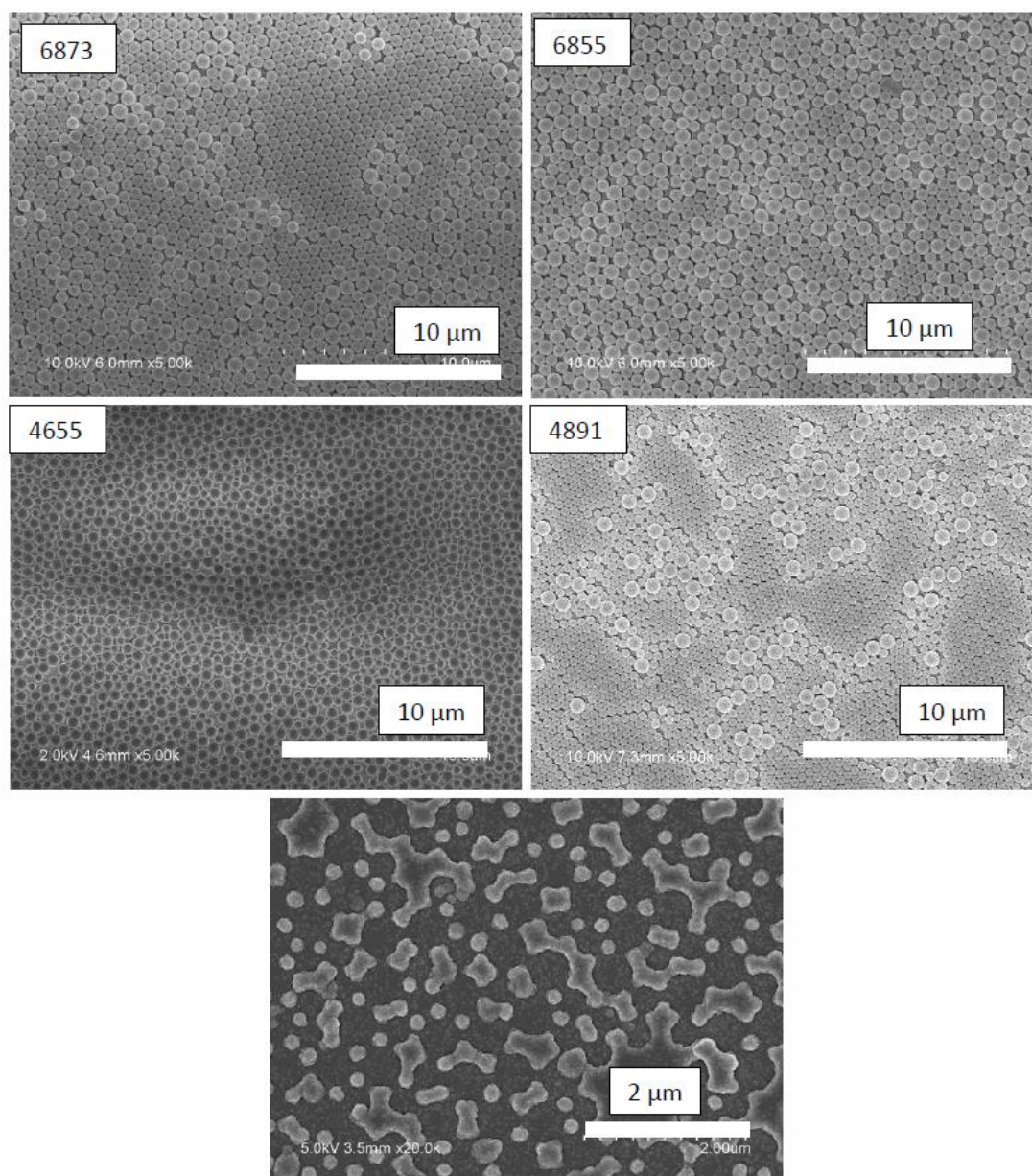


Figure 4.5: SEM images of double PS sphere monolayers and 4655 PSP BR

To characterize the impact of volume ratio of the two sphere sizes on the final BR performance, double sphere PSP BRs reflectance data are plotted in Fig.4.6.

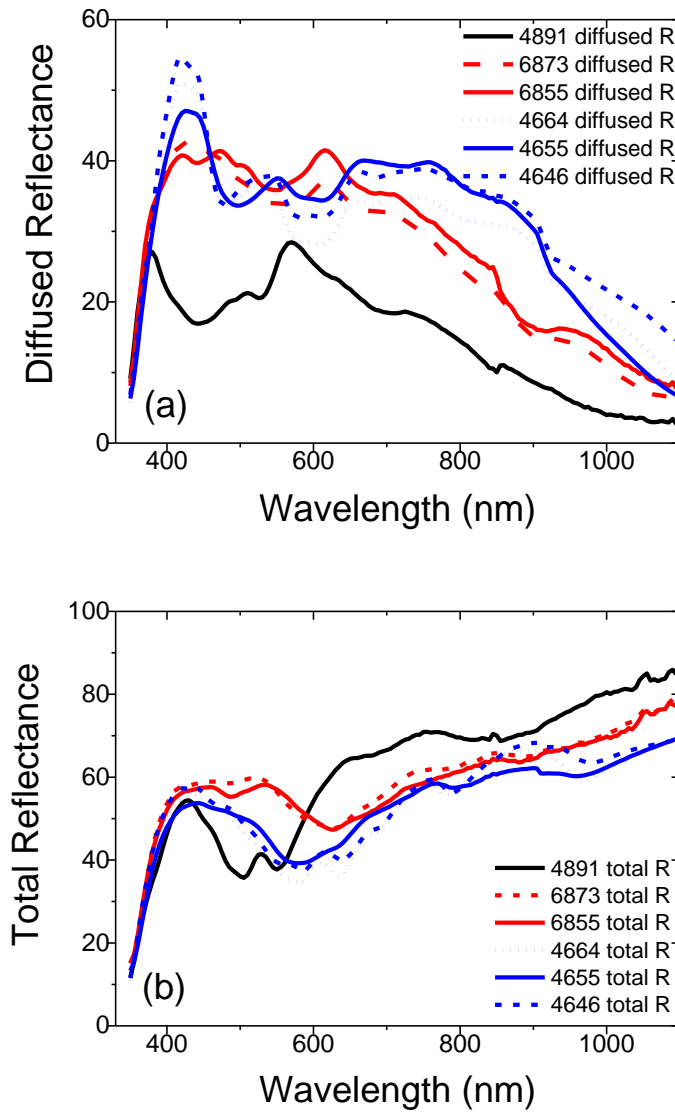


Figure 4.6: Diffused and total reflectance results of various double size PSP BRs.

With referring to Fig.4.4, double PSP BRs do not introduce further reduction in total reflectance as comparing to single PSP BRs. However, there is a significant improvement (on average over 10 % for the whole spectrum) of diffused reflectance for double PSP BRs over single PSP BRs, except for 4891 PSP BRs. The poorer performance of 4891 PSP BR might be due to the large size difference as well as the volume difference of the PS spheres, and

such double sphere mixture patterned BR will have scattering behavior following that of the 400 PSP BR. Hence it reveals a reduced light scattering capability similar to the 400 PSP BR as seen in Fig.4.4 (a). For the 400/600 nm mixtures and 600/800 nm mixtures, we observed a consistent enhanced diffused reflectance from 620 nm wavelength onwards. For 400/600 nm mixtures with different volume ratios, we see that a balanced 50 % to 50 % mixture outperforms other cases in the 550 nm to 800 nm wavelength range, even with only 10 % difference in volume ratio of 60 % to 40 % or 40 % to 60 % cases. With an average 40 % wide band diffused reflectance, this is one of the best performing BRs based on similar design approaches in existing literature [234]. A similar behavior can be seen for 6855 and 6873 PSP BRs. Based on these results we expect that 4655 PSP BRs would provide the best performance of the thin film solar cells, due to its highest diffused reflectance enhancement behavior.

4.4 PS sphere patterned back reflector solar cells performance

In the previous sections we have fabricated and compared the optical performance of different BRs. In this section, the J - V characteristics, EQE and optical absorptance ($1-R_{total}$) results of a-Si:H thin film solar cells fabricated using the various BRs are presented, compared and discussed.

4.4.1 Single size PS sphere patterned back reflector solar cells

The J - V characteristics of Flat BR, 400, 600 and 800 PSP BR solar cells are presented in Fig.4.7, with the corresponding photovoltaic parameters summarized in Table 4.1.

Device name	V _{oc} (V)	J _{sc} (mA/cm ²)	J _{sc} (EQE integrated)	FF (%)	PCE (%)	R _{oc} (Ohm.cm ²)	R _{sc} (Ohm.cm ²)
Flat BR solar cell	0.89	13.7	10.8	62.8	7.39	9.6	1412
400 PSP BR solar cell	0.87	13.3	12.2	59.6	6.83	7.5	438
600 PSP BR solar cell	0.87	15.4	13.1	58.6	7.82	6.3	434
800 PSP BR solar cell	0.86	17.2	13.4	57.9	8.64	5.3	371
4891 PSP BR solar cell	0.88	15.5	13.5	60.3	8.22	5.9	598
6855 PSP BR solar cell	0.87	15.8	13.5	60.7	8.31	6.2	534
4655 PSP BR solar cell	0.88	16.1	13.8	61.9	8.79	5.7	442
ASAHI BR solar cell	0.88	15.9	-	58.4	8.18	9.7	560

Table 4.1: Photovoltaic parameters for various BR solar cells.

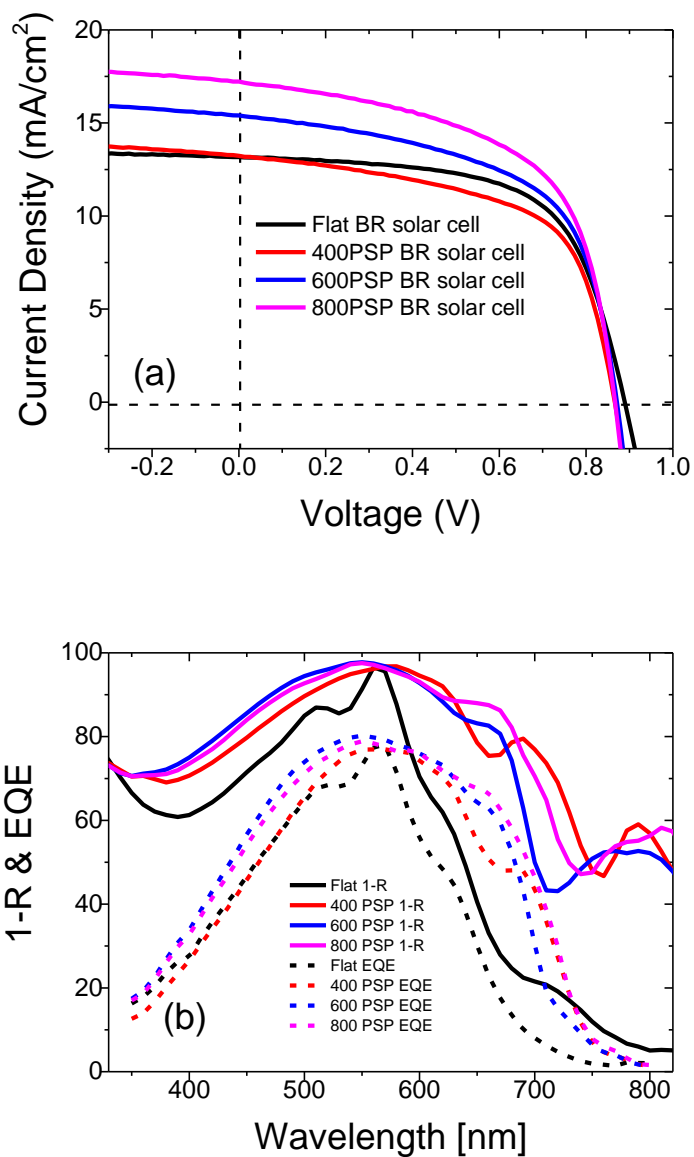


Figure 4.7: J - V , EQE and $1-R_{total}$ of flat, 400, 600 and 800 PSP BR solar cells.

We observe that for the solar cells incorporating 600 and 800 PSP BR, the short-circuit current density is significantly enhanced compared to the flat BR solar cells, while the open-circuit voltage of PSP BR solar cells is slightly compromised ($\sim 3\%$). This indicates a conformal thin film deposition process

over the nanostructured BRs and that our BR did not introduce any significant additional defects, e.g. metallic contamination. From the J - V curves we can easily identify that the increase in current contributes mostly to the performance improvement, which indicates an excellent light trapping enhancement effect. However, the J - V performance of 400 PSP BR solar cells is not as good as expected. From both the J - V and EQE data we observe an underestimation of the devices performance when compared with their $1-R_{total}$ data. This might due to the fact that during the fabrication, the 400 PSP BR was partially peeled off during the ultrasound cleaning, resulting in defective and low yielding 400 PSP BR solar cells.

From Fig.4.7(b), we observed good agreement between the EQE and $1-R_{total}$ results. The difference between EQE and $1-R_{total}$ indicates losses with respect to the total incident photons. At shorter wavelength (300 to 500 nm), ITO absorption, p-layer absorption and p-i interface carrier recombination contribute more significantly to the losses. On the other hand, at longer wavelength (600 to 800 nm), n-layer absorption, n-i interface carrier recombination, and BR substrate absorption contribute more significantly to the losses. Moreover, due to the defects in the intrinsic a-Si:H layer, bulk recombination losses will occur over the whole absorption spectrum, which will also contribute to the difference between EQE and $1-R_{total}$ [195]. In Table 4.1, we also calculated the short circuit current density from the integral of the EQE with respect to the AM1.5 spectrum. We observed a consistent gap between the J_{sc} from solar simulator and J_{sc} from EQE integration. This is due to the c-Si reference sample used during the solar simulator calibration

step. Due to the difference in absorption coefficient between c-Si and a-Si:H, over shooting of the lamp power are expected. On the other hand, under the strong light intensity from solar simulator, free carrier traps (due to defects) are likely to be occupied by the large number of generated electron/hole carriers. While under EQE, low light intensity with black back ground is used. Unoccupied carrier traps are likely to have higher impact on the carrier transfer process; hence a lower J_{sc} value is obtained.

To understand the J_{sc} improvement, i.e. improved photon absorption of the device, EQE as well as optical absorption can be used to provide more details as a function of the incident light wavelength. From the EQE results shown in Fig.4.7(b), we observe that absorption enhancement over the flat BR solar cell lies not only from 550 to 800 nm wavelength range, but also from 350 to 550 nm wavelength range. For shorter wavelength, we attribute the enhancement to Si surface nanostructures, as they can effectively forward scatter light into the active layer below [235]. From 350 to 550 nm, we observe that the 600 PSP BR solar cell performs the best, both from EQE and $1-R_{total}$ results. Given that the 400 PSP BR nanostructures are relatively small, a smoother 400 PSP BR solar cells surface will be formed after deposition. Hence the 400 PSP BR solar cells do not perform as well in the shorter wavelength range. On the other hand, the 800 PSP BR nanostructures are relatively large, and the Si nanostructures formed on the surface might be too large for the short wavelength light interaction.

For longer wavelengths (550 to 800 nm), light interaction mainly comes from the overall nanostructures and the BRs. In this range, EQE and $1-R_{total}$ data show that light trapping performance is the best for the 800 PSP BR solar cells. The 600 PSP BR solar cells follow the same pattern of 800 PSP BR solar cells but with lower performance. The 400 PSP BR solar cells performed well from 580 to 620 nm and from 700 to 750 nm light range, but low absorption from 620 nm to 700 nm is observed. Overall, the 800 PSP BR solar cells have the most enhanced short-circuit current i.e. light trapping performance and our results agree with the prediction that was made based on the optical study of 800 PSP BRs in the previous section.

For the optical absorption data beyond 800 nm, significant absorption of the BR solar cells is observed as well. For the flat BR solar cells, an absorption peak was observed at 960 nm, which is ascribed to Ag/ZnO interface roughness enhanced plasmonic absorption [236]. For our PSP BR solar cells, complex behavior in the $1-R_{total}$ results arise due to the semi-periodic arrangement of Ag/ZnO nanostructures. At around 960 nm, we observe more intense light interactions and multiple plasmonic peaks. The over 30% averaged enhanced diffused reflectance results confirmed the strong light scattering capability of our PSP BR solar cells from 800 to 1200 nm range. This is particularly relevant for $\mu\text{c-Si:H}$ solar cells [215], as this part of light scattering enhancement can contribute to the light trapping performance as well. We attribute two reasons to the significantly enhanced light scattering: on one hand with incorporated Ag/ZnO nanostructures, various plasmonic resonance modes are excited; on the other hand, the semi-periodic

nanostructures on BRs can be effectively treated as 3D light gratings with different diffraction orders. These gratings reflect light in different directions at off normal angles which extend the light travelling path significantly.

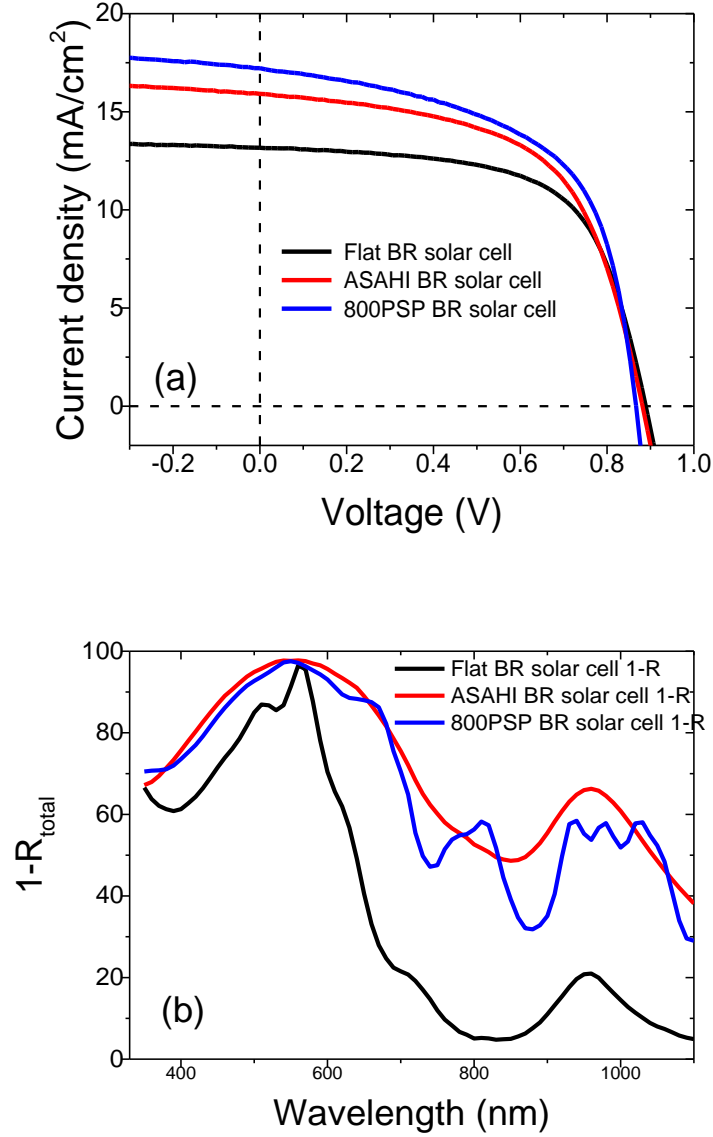


Figure 4.8: J - V and $1-R_{\text{total}}$ results of flat, ASAHI and 800PSP BR solar cells

A comparison between the flat, ASAHI and 800PSP BR solar cells is presented. The J - V , $1-R_{\text{total}}$ results shown in Fig.4.8 and the photovoltaic parameters are tabulated in Table 4.1. For the ASAHI BR solar cell, the 1 -

R_{total} behavior follows that of flat BR solar cell, but with much higher absorption, which indicates a much rougher Ag/ZnO interface as compared with flat BRs [231]. This can be easily understood since ASahi is a nanostructured substrate. We observe that our 800 PSP BR solar cell outperforms the ASahi BR solar cell from the J - V performance, but the $1-R_{total}$ result of the cells is similar. The optical losses associated with ASahi BR could be the reason that degrades the ASahi BR solar cell performance. Referring to table 4.1, we also observe that the fill factor of the double sphere PSP BR solar cells is better than that of the ASahi BR solar cell. This also indicates a smoother surface of our PSP BRs, compared to ASahi BRs, such that more a conformal silicon thin film deposition on our PSP BRs favors the fill factor improvements.

4.4.2 Double size PS sphere patterned back reflector solar cells

Based on the conclusions that we have drawn from the optical results of double PS sphere BRs, 4891, 6855 and 4655 BRs were used as the substrates for n-i-p solar cells. Fig.4.9(a) shows the J - V characteristic and Fig.4.9(b) shows the EQE and $1-R_{total}$ results of the solar cells.

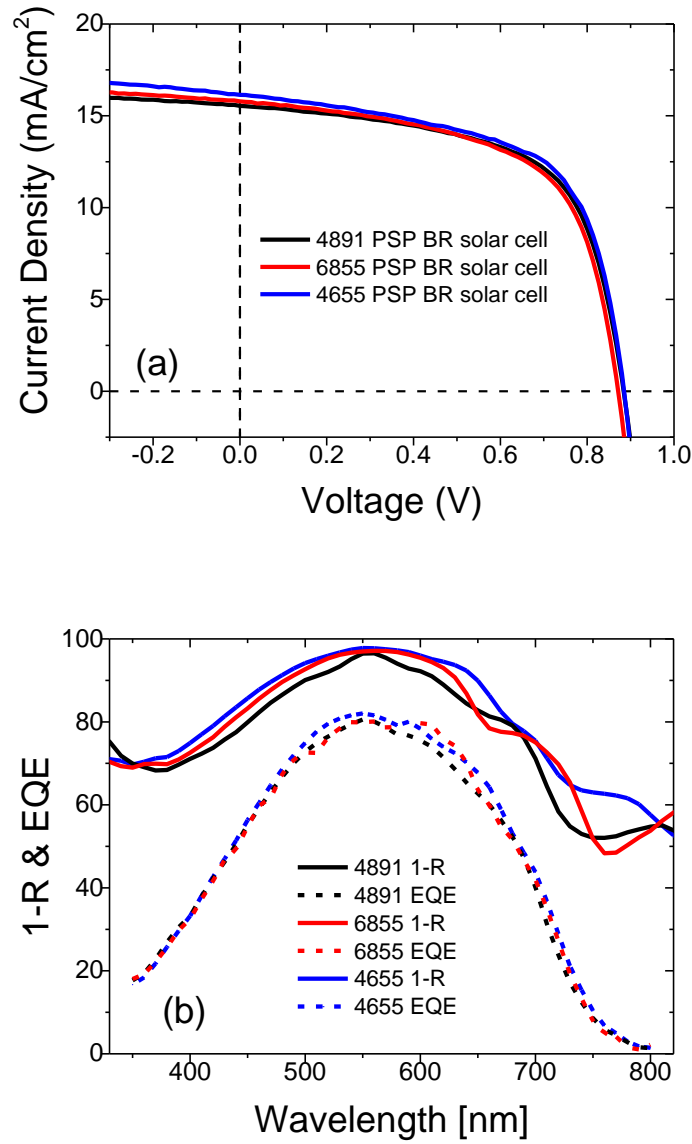


Figure 4.9: $J-V$, EQE and $1-R_{total}$ of 4891, 6855 and 4655 PSP BR solar cells.

Across the different double PSP BR solar cells, 4655 PSP BR solar cells outperform others consistently on $J-V$, EQE as well as $1-R_{total}$ results. Comparing with single size PSP BRs, we predicted that double size PSP BRs will have a more random distribution of Ag nanostructures. This will improve the diffused reflectance and lead to the enhanced light scattering capability of our double size PSP BR. This allows us to achieve a high initial PCE of 8.79% (see Table 4.1). The performance comparison between 4655 double

sphere BR solar cell with 400 and 600 PSP single sphere BR solar cells are plotted in Fig.4.10.

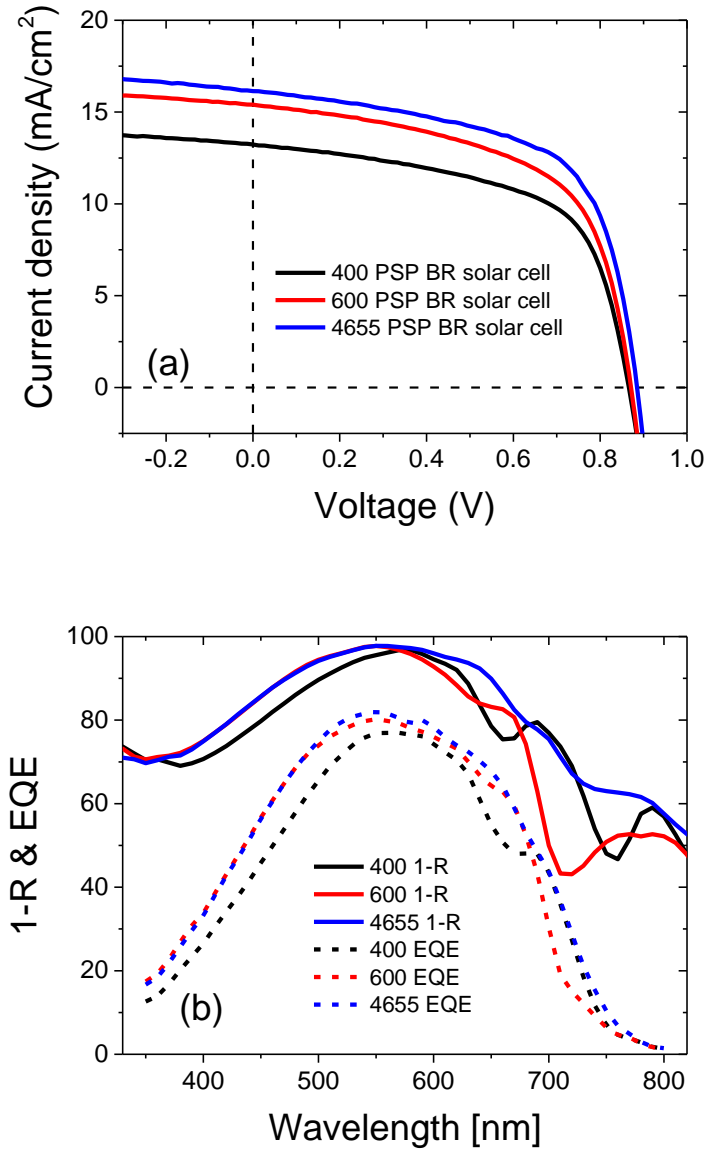


Figure 4.10: J - V and $1-R_{total}$, EQE results of 400, 600 PSP and 4655 PSP BR solar cells

We observe that, comparing 4655 PSP BR solar cell with 400/600 PSP BR solar cells, not only the J_{sc} and FF are improved from J - V curve from Fig.4.10(a), but also the EQE and $1-R_{total}$ are improved. We notices that from

the $1-R_{total}$ results, the local minimum at 650 nm for 400 PSP BR solar cell and 700 nm for 600 PSP BR solar cell are not present in 4655 PSP BR solar cell. Such behavior shows better light trapping performance of mixture sphere patterned device over single sphere patterned device.

4.5 Conclusion

In this chapter, we demonstrated a novel design and fabrication process for light trapping in thin film amorphous silicon solar cells. Both single and double sphere patterned BRs as well as corresponding solar cell devices were fabricated and tested. The double sphere patterned BR solar cells are proven to be more effective in light scattering, which lead to a better light trapping performance. Without impacting the open-circuit voltage, the PSP BR solar cells show an improved performance compared to the commercial ASAHI BR solar cells. Furthermore, this method can be applied on any substrate as long as their surface is hydrophilic. Moreover, this approach is not limited to a-Si:H solar cells, but can also be applied to the case of μ c-Si:H silicon thin film solar cells. As a low cost, robust and process compatible approach, this nanostructured BR approach is an effective candidate for improved light trapping performance of silicon thin film solar cells.

Chapter 5. Optical Study and Experimental Realization of Nanostructured Back Reflectors for Enhanced Light Trapping with Reduced Parasitic Losses in Silicon Thin Film Solar Cells

In this chapter, we study light trapping as well as parasitic losses in hydrogenated amorphous silicon thin film solar cells fabricated by plasma-enhanced chemical vapor deposition on nanostructured back reflectors. The back reflectors are patterned using polystyrene assisted lithography. By using O_2 plasma etching of the polystyrene spheres, we managed to fabricate hexagonal nanostructured back reflectors. Firstly, we will introduce various sources of the parasitic losses in silicon thin film solar cell and previous studies aimed at reducing those losses. A review of modelling of silicon thin film solar cells will be summarized. Secondly, the fabrication process of hexagonal nanostructured back reflectors and the corresponding solar cells will be introduced. After that, with the help of Bruggeman Effective Medium Approximation, we will present our simulation study of parasitic losses in flat Ag/ZnO back reflectors and random nanostructured Ag/ZnO ASAHI back reflectors. Following that, we will compare the light scattering properties of random nanostructured Ag/ZnO ASAHI back reflectors with our semi-periodic hexagonal nanostructured Ag/ZnO back reflectors. With the help of high frequency electromagnetic field simulator modelling, we will further investigate the corresponding optical losses in each layer separately. Last but not least, simulation results of a full device built upon the back reflector will be presented. Based on the simulation model, we fabricated and characterized

the silicon thin film solar cells. Experimental results will be presented and verified with the simulation results as well.

5.1 Introduction and objectives

As we discussed in Chapter 2 and Chapter 4, light trapping in silicon thin film solar cell are of extreme importance towards achieving high efficiency devices. Conventional light trapping is introduced by growing the silicon thin films on a rough or textured transparent conductive oxide (TCO) surface [237]. Such structure allows light to be scattered to the off normal angles at the rough interface between TCO and silicon. The scattering of light increases the optical path which leads to a higher absorption in the silicon layer. This will give rise to a higher photogenerated current, hence improved device performance [238]. This approach has been applied successfully in silicon thin film solar cell in both substrate (n-i-p) and superstrate (p-i-n) configurations [239].

More recently, nanostructured metal/dielectric back reflector (BR) with high reflection and strong far field scattering properties has been proposed for the substrate (n-i-p) configuration for its potential to further increase the short circuit current of silicon thin film solar cells [193], [215], [233]. However, there is a trade off between the design of the nanostructured BRs for enhanced light absorption and minimum parasitic losses which come from surface plasmonic absorption in the rough metallic/dielectric rough interface layer [240], [241]. To address and characterize such losses, Bruggeman Effective Medium

Approximation (BEMA) was previously studied by L. R. Dahal *et. al.* to study the parasitic losses due to a flat or “nanoscale roughness” Ag/ZnO and Al/ZnO interface [236]. Moreover, parasitic losses will be introduced not only from the BRs, but also from the other layers which do not contribute to photocurrent generation, e.g. TCO [242] and n/p doped layers [243], [244]. For a systematic study for an optimized overall design, the electromagnetic simulation was preferred. Not only it is a powerful tool for the interpretation of the light/nanostructures interactions, but also the absorption enhancement effect in the active layer or parasitic absorption in the non-active layers can be systematically studied and different mechanisms of the electric field enhancement in the system can be readily isolated [245], [246].

In our work, we first systematically study optical losses of flat Ag/ZnO BRs and random nanostructured Ag/ZnO ASAHl BRs with different ZnO thickness. With ZnO thickness as the variable, we assess the simulation accuracy of the proposed BEMA model by experimental results. The origin of the parasitic losses in random ASAHl nanostructured Ag/ZnO BRs is concluded. Following that, hexagonal nanostructured Ag/ZnO BRs are fabricated by using polystyrene assisted lithography [227]. Light scattering properties as well as optical losses of such BRs are compared with random nanostructured ASAHl BRs. Using high frequency electromagnetic field simulator (HFSS, <http://www.ansys.com/Products/Electronics/ANSYS-HFSS>), we further model and investigate the corresponding optical losses in each layer separately. We also simulate the performance of solar cells incorporated with the BR. Different light scattering modes and the parasitic losses in each layer are

extracted from the simulation results. Photo-generated current is calculated with respect to the AM1.5 solar spectrum. Based on the optical modelling results, we fabricated and characterized amorphous silicon thin film solar cells. The experimental and simulation results are compared and discussed.

5.2 Fabrication of hexagonal nanostructured Ag/ZnO back reflectors and back reflector solar cells

5.2.1 Hexagonal nanostructured Ag/ZnO back reflector

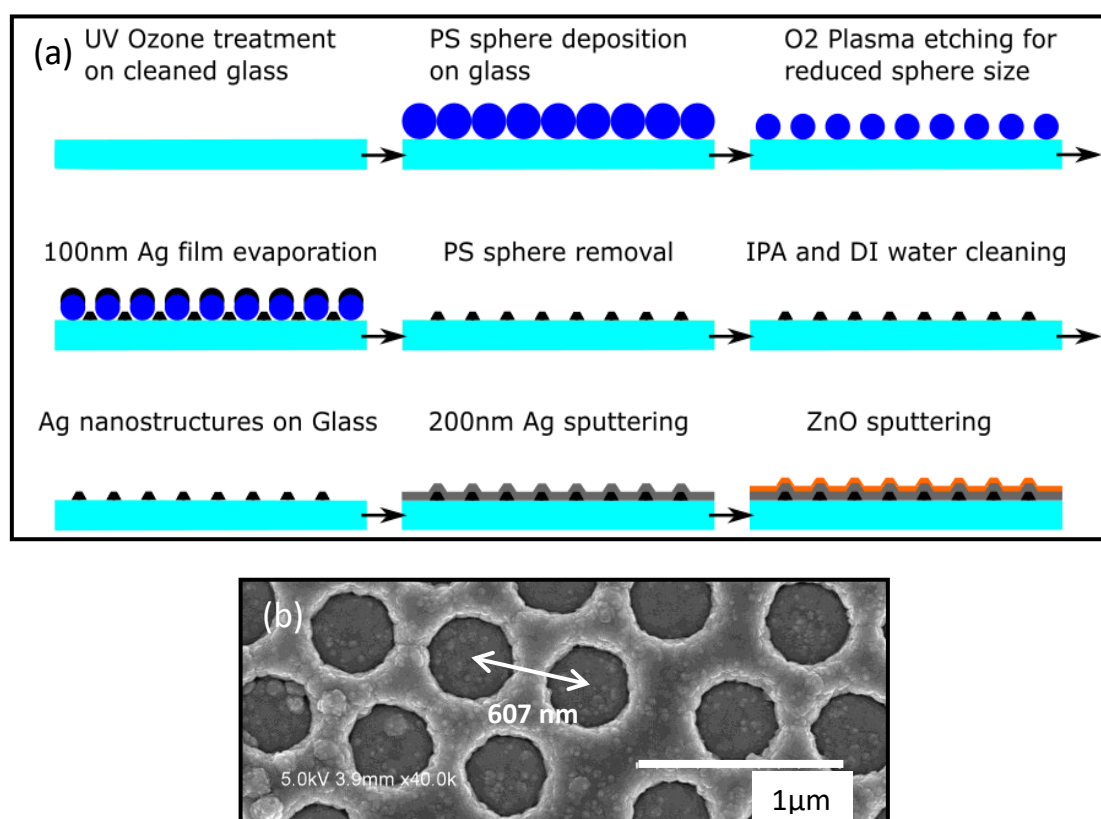


Figure 5.1: (a) Fabrication process and (b) top view SEM images of hexagonal back reflectors (pitch = 607 nm) taken after the process steps shown in Fig.5.1(a).

The PS spheres used in this work were a monodisperse suspension with 5 w.t. % in water, obtained from microparticles GmbH with nominal diameters of 607 ± 15 nm. We used methanol as the spreading agent and mixed in 1:1 volume ratio with the pristine PS solution. Prior to the PS sphere monolayer

transfer, Corning glasses were cleaned with acetone, isopropanol (IPA) and de-ionized (DI) water in ultrasonic bath, followed with a 10 min UV-Ozone treatment to keep the surface hydrophilic. We used the floating transfer technique for PS spheres monolayer deposition on Corning glass. After that, we used a well-controlled electron cyclotron resonance (ECR) reactive ion etching (RIE) oxygen plasma etching process for a uniform size reduction of the PS spheres [227]. For oxygen plasma etching condition, we used 40 sccm of O₂, pressure of 2 mTorr, 160 sec of etching time at 500 W of plasma power. After thermal evaporation of 100 nm Ag, the substrates were immersed in toluene and a 20 min low power ultrasonic bath in toluene was applied for a complete removal of remaining PS spheres. Another 10 min IPA and DI water ultrasonic bath was applied for a complete removal of any organic solvent residue. Finally, we used RF (13.56 MHz) sputtering system to coat a layer of 200 nm Ag onto the substrates at room temperature using RF power of 50 W, argon flow rate of 41 sccm and process pressure of 5.7×10^{-3} mbar. Without breaking the vacuum in the sputtering system, ZnO with different thickness was sputtered sequentially at room temperature using RF power of 250 W, argon flow rate of 30 sccm and process pressure of 4.3×10^{-3} mbar. Fig.5.1(b) shows the top view SEM image of the hexagonal BR fabricated.

5.2.2 Silicon thin film solar cell

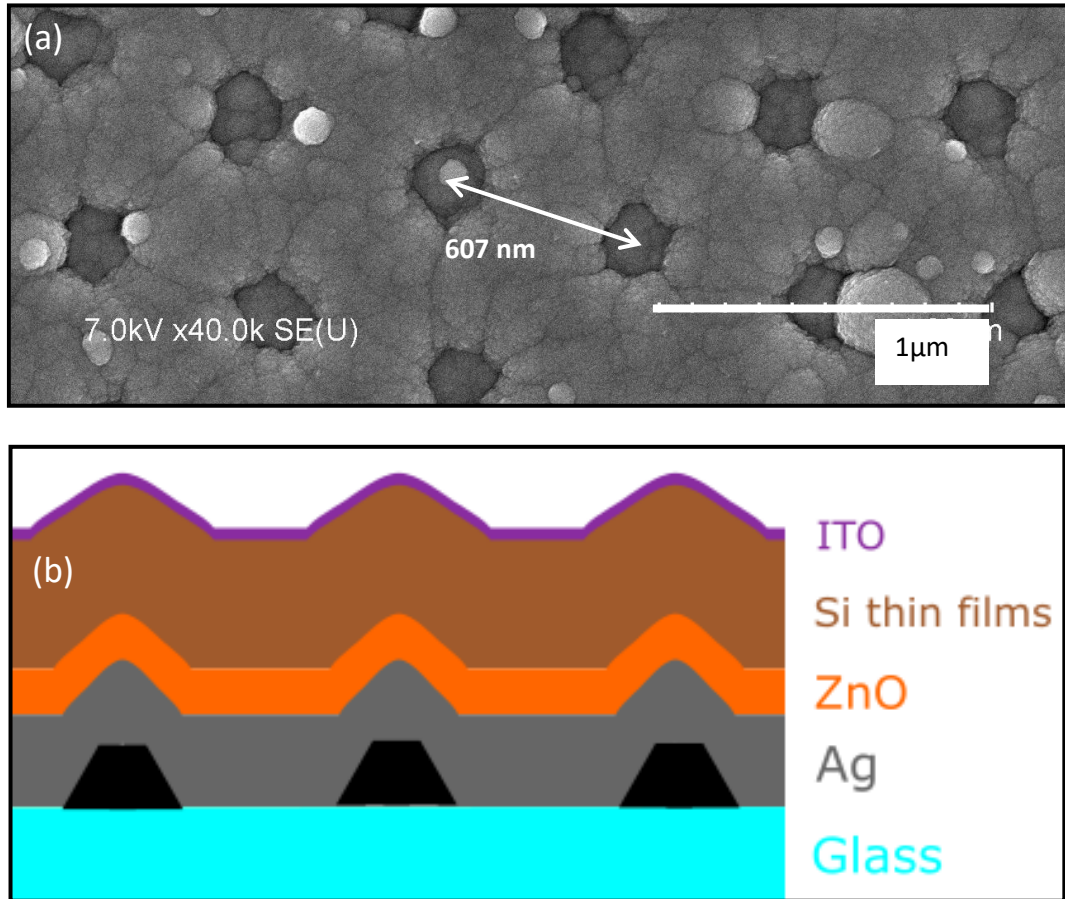


Figure 5.2: (a) Top view SEM image, taken after full device fabrication, and (b) schematic cross section of a hexagonal back reflector solar cell.

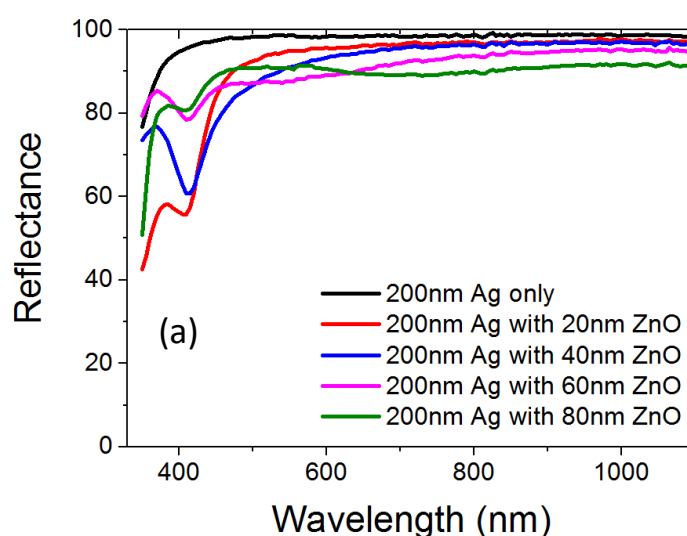
Amorphous silicon thin films were deposited in a 13.56 MHz radio frequency (RF) PECVD system [247]. Three plasma chambers sharing the same vacuum pump were used to separate n-type, intrinsic and p-type a-Si:H deposition to avoid any cross contamination. Firstly, a 25 nm thick n-type microcrystalline silicon oxide layer was deposited on the BR [248]. Without breaking the vacuum, ~230 nm of intrinsic amorphous silicon layer has been deposited using SiH₄ plasma, followed by a 25 nm thick p-type amorphous silicon carbide layer. Lastly, 80 nm thick indium tin oxide (ITO) have been deposited to form the top contacts and to define a cell with an area of 0.126 cm². Such photovoltaic device was often referred to n-i-p solar cell [239]. A

schematic image of the side view of the device and a corresponding SEM image acquired using Hitachi S-4700 Scanning Electron Microscope is shown in Fig.5.2. The current density-voltage (J - V) characteristics of the solar cells were measured under AM1.5G illumination with a commercial solar simulator (Oriel AAA), calibrated using a crystalline Si reference cell. Total and diffused reflectance were measured using a Perkin-Elmer Lambda 950 spectrometer from 350 nm to 1100 nm wavelength range with a 150 mm integrating sphere and an PbS detector.

5.3 Optical characterization of flat and ASahi back reflectors

Before we proceed to study the optical properties of our nanostructured BRs, reference flat Ag/ZnO on glass substrates were fabricated and its reflectance was measured. Fig.5.3 shows the reflectance data from sputtered ZnO (0 to 160 nm) on 200 nm sputtered Ag on the glass. Figure 5.4 shows the reflectance data of ASahi BR with 0, 50 and 100 nm of ZnO. Figure 5.5 (a) shows the BEMA simulation model we used. Fig.5.5 (b) and (c) show the simulated results for various thicknesses of the rough interface layer L2 between ZnO and Ag.

5.3.1 Total reflectance from flat and ASahi back reflectors



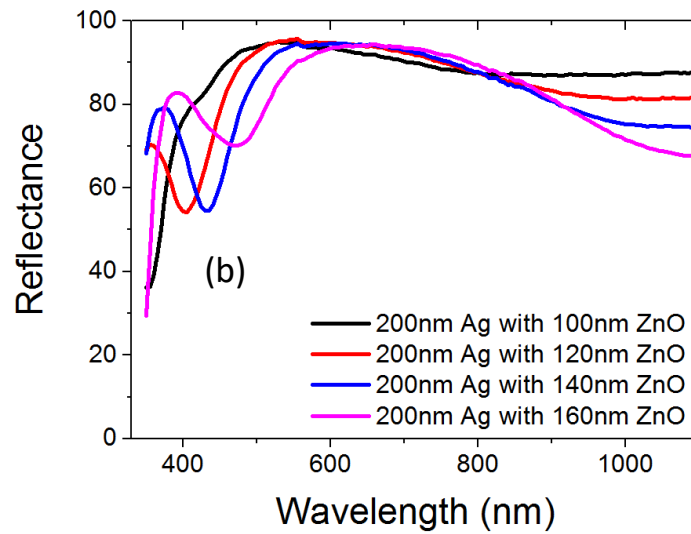


Figure 5.3: Total reflectance measured on a glass substrate coated with 200 nm Ag and various thicknesses of ZnO (0 – 160 nm).

As expected, a pure 200 nm of Ag film on glass provides a highly reflective surface from 350 nm to 1100 nm wavelength range, with minimum absorption at shorter wavelength. In Fig.5.3(a), we observed that when a thin ZnO was deposited on top of Ag, with increasing thickness from 20 nm to 100 nm, the local reflectance minimum at 415 ~ 420 nm diminishes. D. Sainju [231] concluded that the rough Ag/ZnO interface introduces localized plasmonic absorption at the nano-protrusions on the Ag surface at around 2.9 eV, which exactly corresponds to local reflectance minimum at 420 nm observed in Fig.5.3(a). With increasing ZnO thickness, such reflectance minimum becomes less significant. Previous study has shown that with increasing ZnO thickness, its refractive index will decrease [249]. It was argued that when an interference minimum in reflectance matches the plasmon energy of the rough Ag/ZnO interface, this will lead to a strong coupling of the energy from the optical field into the plasmon mode [250]. With increased film thickness, not

only the interference minimum shifts away from 420 nm, but also the refractive index of the top ZnO layer decreases. The combined two effects have led to decreased plasmon absorption, hence a weaker local reflectance minimum at 420 nm is observed. The effect of interference minimum is more prominent as seen in Fig.5.3(b). When thicker ZnO was deposited on top of Ag, with increasing thickness from 120 nm to 140 nm to 160 nm, reflectance minimum shifts correspondingly from 400 nm to 430 nm to 470 nm. By using the refractive index of 139 nm thick ZnO [249], we can calculate the condition of destructive interference using:

$$\lambda_{destructive} = \frac{2 \times n_{ZnO} \times t_{ZnO} \times \cos(7^\circ)}{m - \frac{1}{2}}$$

where n_{ZnO} is the ZnO refractive index at the targeted wavelength, t_{ZnO} is the ZnO thickness, $\cos(7^\circ)$ is included in the equation due to the 7 degrees angle of incident under which the reflectance data was measured. Integers $m = 1$ and 2 account for the 1st and the 2nd destructive interference respectively. At 120 nm ZnO thickness, by using $n_{ZnO} = 2.5$ at 400 nm wavelength [249] (where we presume 400 nm is the 2nd destructive inference), the calculated $\lambda_{2nd\ destructive}$ at $m = 2$ is 397 nm. The above calculation matches the observation of the reflectance minima and such minima will red shift with increasing ZnO thickness. The 1st destructive interference wavelength $\lambda_{1st\ destructive}$ is calculated to be 953 nm, by using $n_{ZnO} = 2$ (refractive index around 900 nm) and $m = 1$. This further explains the minor reduced reflectance for the wavelength range of 800 nm and beyond as seen in Fig.5.3.(b). Other than the above, the increased free carrier absorption of a thicker ZnO layer will also play a role in the overall optical performance [251]. From the

experimental data, to avoid parasitic absorption by the BRs in the longer wavelength range, 100 nm of ZnO might be more desirable when compared with thicker ZnO cases. As the thickness of ZnO determines the absorption behavior of flat Ag/ZnO BRs, special care should be taken on the choice of ZnO thickness when BRs are nanostructured.

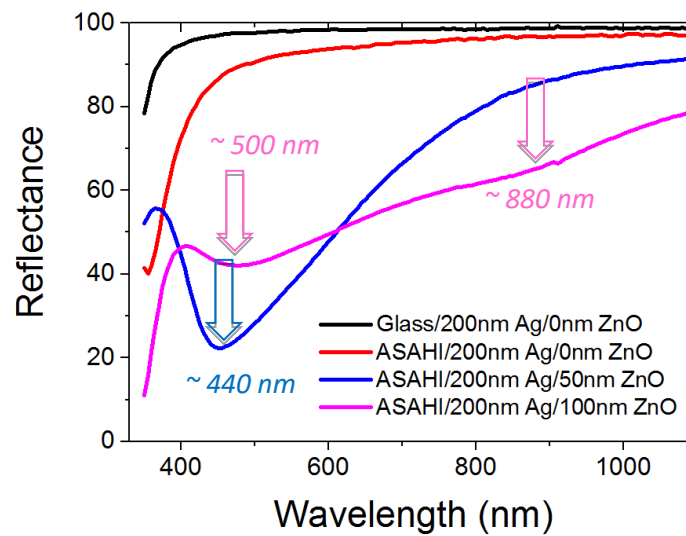


Figure 5.4: Total reflectance measured on ASAHI substrate coated with 200 nm Ag and with 0, 50 and 100 nm of ZnO.

With the above understanding of flat Ag/ZnO BRs performance in mind, the reflectance results from ASAHI BRs will be presented. In Fig.5.4, 200 nm of Ag sputtered on rough ASAHI substrate shows lower reflectance compared with 200 nm of Ag sputtered on flat glass substrate. This is simply due to higher plasmonic absorption on a rough Ag surface [252]. With 50 nm of sputtered ZnO on top, significant absorption is observed for all wavelengths with local reflectance minimum at around 440 nm. With 100 nm of sputtered ZnO on top, reflectance further reduces from 600 to 1100 nm wavelength range but partially recovers from 400 to 600 nm range. Two local minima at

around 500 and 880 nm are observed. Such large difference in optical performance between flat BR and ASahi BR shall be fully understood before we proceed to study the more complex hexagonal nanostructured Ag/ZnO BRs.

5.3.2 Bruggeman effective medium approximation simulation

In this section, we use Bruggeman Effective Medium Approximation (BEMA) method to estimate the optical performance of the rough and random nanostructured ASahi Ag/ZnO BRs. BEMA is a fast simulation method for the macroscopic properties of composite materials, where in our case it will be Ag and ZnO composition in the BRs. With a 35 nm r.m.s. roughness on ASahi substrate surface [253], one would expect less than 35 nm surface roughness at Ag/ZnO interface with added smoothing effect of the sputtered Ag layer [254]. To estimate the Ag/ZnO interface roughness and to correlate between interface roughness and the optical performance, BEMA simulation is used to study the random nanostructure ASahi Ag/ZnO BRs. In the simulation, we used the generalized anisotropic Bruggeman EMA to model the effective medium layers. This model can be derived from the generalized form of Maxwell Garnett's EMA using the expression for the polarizability of ellipsoidal particles,

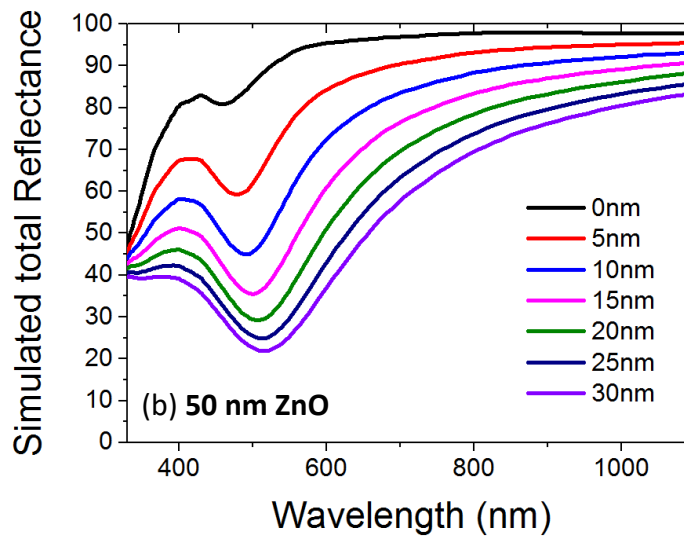
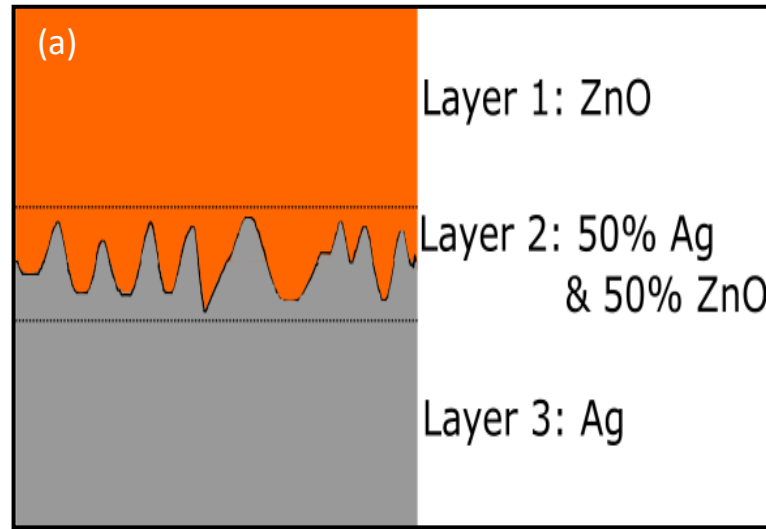
$$\frac{\epsilon_{eff} - \epsilon_0}{\epsilon_0 + L(\epsilon_{eff} - \epsilon_0)} = \sum_{i=1}^M f_i \frac{\epsilon_i - \epsilon_0}{\epsilon_0 + L(\epsilon_i - \epsilon_0)},$$

Where ϵ_{eff} is the effective medium permittivity, ϵ_0 is the permittivity of the host medium, and ϵ_i and f_i are the permittivity and volume fraction of each of the

M materials. The depolarization factor L depends upon the shape of the ellipsoids and the direction of the electric field. In our case, we simplified our model into a 50% to 50% volume ratio of Ag and ZnO in the form of highly ablute ellipsoids aligned along the z direction $L_x = L_y = 0, L_z = 1$. In this case, the permittivity reduced to:

$$\varepsilon_x = \varepsilon_y = (1 - f)\varepsilon_0 + f\varepsilon_1; \varepsilon_z = [(1 - f)\varepsilon_0^{-1} + f\varepsilon_1^{-1}]^{-1}$$

Where ε_0 and ε_1 are permittivity of Ag and ZnO respectively and $f = 0.5$.



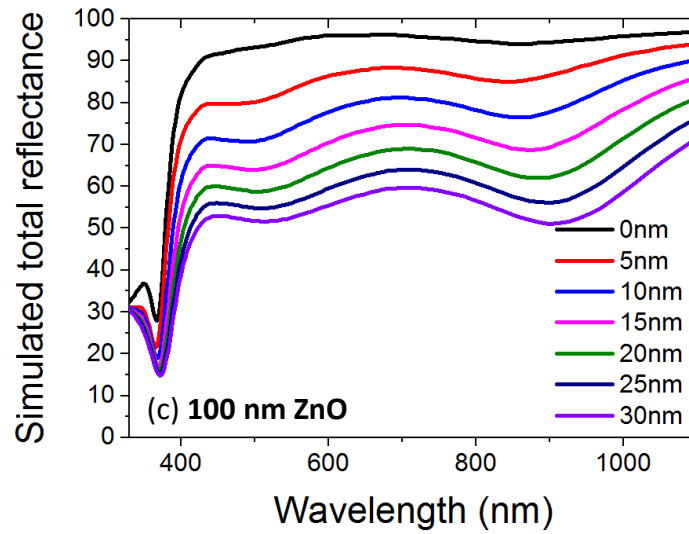


Figure 5.5: (a) Bruggeman effective medium approximation model applied for the Ag/ZnO BR study; (b) & (c) Simulated total reflectance of 50 and 100 nm ZnO (layer 1) with 0 to 30 nm of Ag/ZnO interface (layer 2) thickness.

Fig.5.5(a) shows the BEMA simulation model used. We designed our simulation model such that the Ag/ZnO interface roughness is modelled as a thin film layer (L2) composed of 50 % Ag and 50 % ZnO, in between the pure ZnO layer (L1) and pure 200nm Ag layer (L3). By assuming a uniform Ag surface roughness and also a conformal coating of the ZnO on top, 50 % to 50 % composition ratio of the two materials and 0 % void can be a good approximation to model the interface roughness layer. Fig.5.5(b) and Fig.5.5(c) show the simulated reflectance with 50 and 100 nm of ZnO layer respectively. The interface roughness, i.e. thickness of L2, changes from 0 to 30 nm with a step of 5 nm.

With 50 nm of ZnO, comparing between the experimental results in Fig.5.5.(a) and simulation results in Fig.5.5(b), we can see that in terms of the absolute

magnitude, the reflectance from ASAHI BRs is close to the case of simulated 25 nm interface roughness. However, in terms of the position of the local reflectance minima, the reflectance from ASAHI BRs is close to the case of simulated 10 nm interface roughness. Similarly, under the 100 nm ZnO condition, simulated 25 nm interface roughness shows closer results in absolute magnitude, but simulated 10 nm interface roughness shows a closer result to experiment data in reflectance local minima. The above observations can be explained by considering that with increasing Ag/ZnO interface layer thicknesses, the effective overall ZnO thickness will be increased. The red shift of the reflectance minima is due to the increased ZnO thickness. In order to design our simulation model to be best fitted to the experimental data, ZnO layer thickness should be adjusted.

From the simulation results above, we can observe that ZnO thickness (L1) determines the shape of the reflectance curve, while Ag/ZnO interface thickness (L2) determines the magnitude of the reflectance value. We proposed the explanation that the top ZnO (L1) governs the interference behavior of the incident light. Ag/ZnO interface (L2) on one hand could absorb light which reduces the overall reflectance, and on the other hand could be effectively treated as an antireflection layer in between the ZnO and bulk Ag. Such antireflection effect allows more light to be incident from top ZnO (L1) into bottom bulk Ag (L3), hence more Ag absorptions which turn out to be unwanted parasitic BRs absorptions. From Fig.5.5(b & c), with increasing L2 thickness, we observe a uniform reflectance reduction in wavelength range around 1000 nm to 1100 nm and a saturating reflectance reduction in

wavelength range around 500 nm. This difference can be explained by the antireflection effect, which saturates with increasing L2 thickness. The saturation in absorption loss of the BRs had been observed by *J. Springer et al.* [240], while we propose a new possibility to explain such behavior using BEMA approximation.

Our model predicts that such BR has an interface thickness of 25 nm. Surprisingly if we compare the simulated 5 nm interface roughness (100 nm ZnO layer 1) with 100 nm ZnO on 200 nm Ag reflectance data in Fig.5.3, we can also observe a similar reflectance magnitude and local minima position. Hence, from the perspective of our simulation results, the nominally flat Ag/ZnO BR also has a 5 nm Ag/ZnO interface thickness. The ZnO/air surface roughness has been investigated as well, and no significant changes in the reflectance behavior are observed.

5.4 Experiment and simulation results on hexagonal Ag/ZnO nanostructured back reflectors

In previous sections, we have presented the study on the flat and random nanostructured ASAHI BRs. Their optical loss mechanisms were investigated and correlated with the thickness of ZnO layer as well as Ag/ZnO interface layer. In this section, hexagonal nanostructured BRs are studied. Fig.5.6 shows the top view of the BRs with different O₂ plasma etching times (see Fig.5.1(a) for the process flow).

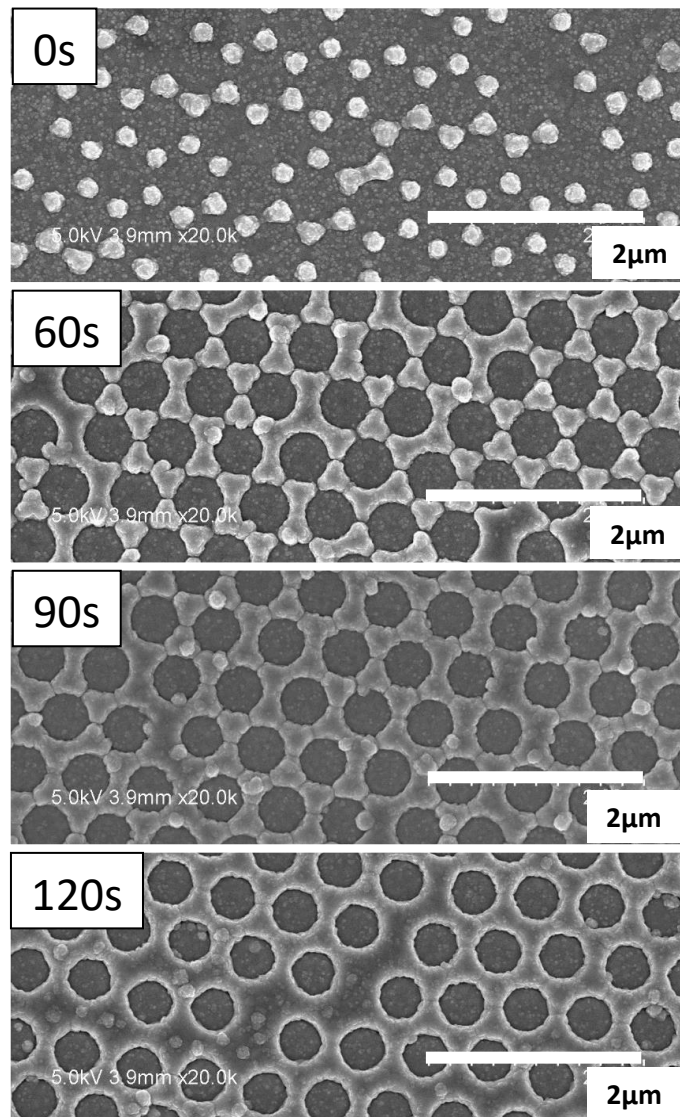


Figure 5.6: SEM images of hexagonal Ag/ZnO back reflectors obtained with 0, 60, 90 and 120 s of O₂ plasma treatment of polystyrene spheres.

BEMA is not appropriate to describe the optical behavior of our hexagonal nanostructured BRs. For such BRs, with a semi-periodic arrangement of the metal/dielectric nanostructures and close-to-visible wavelength inter-nanostructure distance, we would expect more plasmonic modes to be present in the system, hence higher optical losses of the hexagonal nanostructured BRs compared with random ASAHI BRs. However, a higher optical loss of the nanostructured BR might not necessarily mean a poorer substrate for solar cell application. For the nanostructured BRs, light scattering capability is another figure of merits that might be more crucial for one to take into consideration. The diffused reflectance is an indirect way to characterize the scattering capability of the BRs [234]. To further investigate, not only the total reflectance but also the diffused reflectance data were collected.

5.4.1 Total and diffused reflectance of hexagonal Ag/ZnO nanostructured back reflectors

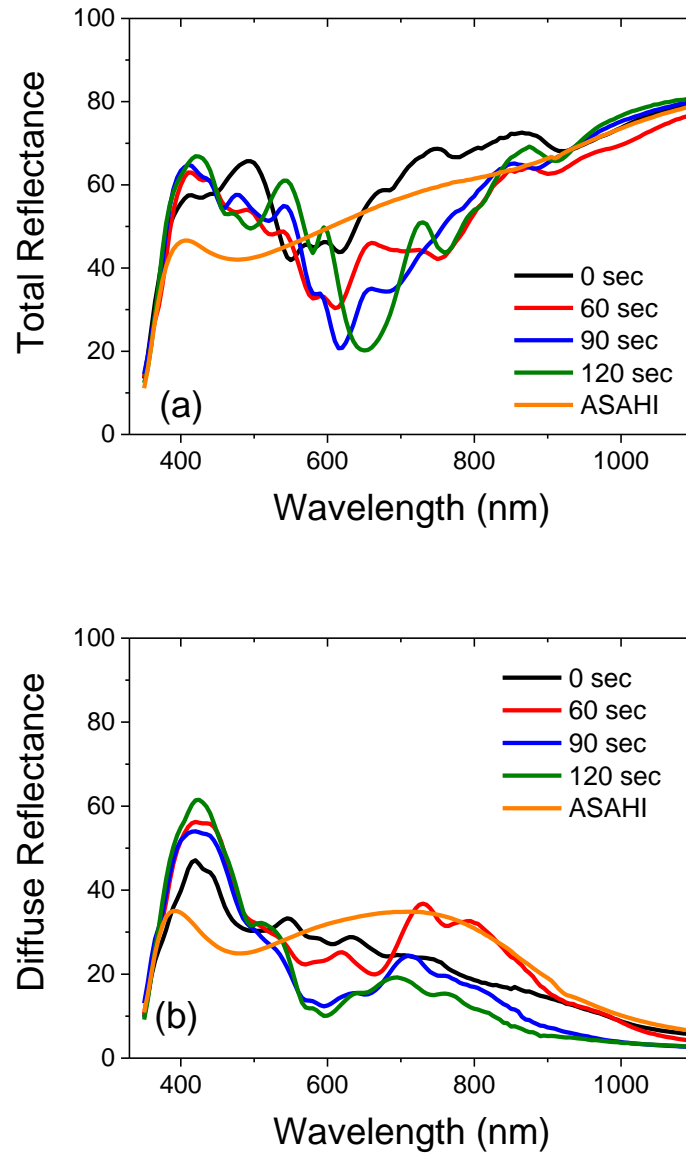


Figure 5.7: (a) Total and (b) diffused reflectance of hexagonal Ag/ZnO BRs and ASAHI BR with 100 nm ZnO.

Fig.5.7 (a) and (b) show the total and diffused reflectance of the hexagonal nanostructured BRs and ASAHI BR with 100 nm ZnO (see Fig.5.6 for SEM images). Similar optical performances with different etching time are observed.

Comparing with ASAHI BR, we observe higher total reflectance as well as higher diffuse reflectance from ~ 370 nm to ~ 570 nm wavelength range. This shows that over this range, hexagonal nanostructured BRs not only have a lower optical loss but also a stronger light scattering capability. However, from ~ 570 nm to ~ 840 nm range, which is more critical for light trapping in silicon thin film solar cell, the total reflectance of the hexagonal nanostructured BRs are significantly lower than that of ASAHI BR, especially for the BRs fabricated using O_2 plasma etching. This indicates that, other than Ag/ZnO interface roughness, additional absorptions are present in the hexagonal nanostructured BRs. Due to such significant additional absorptions, the amount of light that is been diffusively reflected is been reduced as well. Hence, for around 570 nm to 700 nm, the diffuse reflectance of hexagonal nanostructured BRs are lower than ASAHI BR. Surprisingly for 60 sec hexagonal nanostructured BR case, from 700 to 900 nm range, a comparable or even higher diffuse reflectance compared to ASAHI BR are observable (Fig.5.7(b)), regardless of the observed higher optical losses of the 60 sec hexagonal nanostructured BR. Furthermore, with the increasing etching time, we notice a decrease in the diffused reflectance, and a red shift in the total reflectance. To understand the source of the reduced reflectance at different local minima and the effect of the etching time for the losses in total reflectance, HFSS model was designed and the simulation results obtained are compared with the experiment results.

5.4.2 Simulated absorption of hexagonal Ag/ZnO nanostructured back reflectors

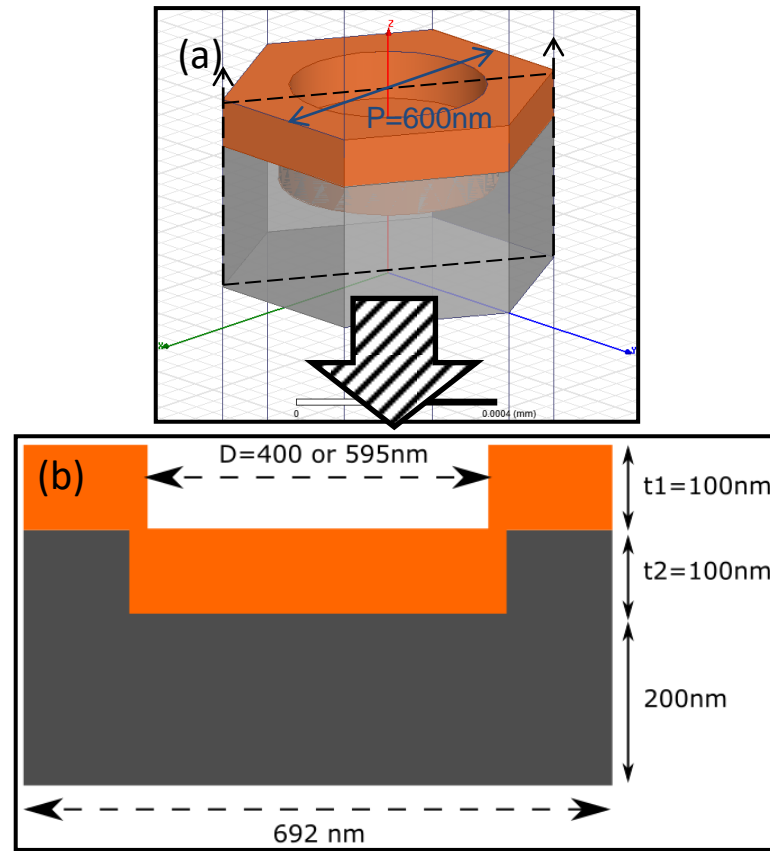


Figure 5.8: Simulated hexagonal nanostructured back reflector, (a) HFSS unit cell in the simulation model and (b) corresponding cross sectional view.

Fig.5.8(a) and (b) show the unit cell in the simulation model and the corresponding cross sectional view of the BRs. Due to the periodic boundary conditions placed onto the six sides of the unit cell, an infinitely large area is simulated by repeating the unit cells next to each other. Such hexagonal nanostructure has a fixed periodicity of 600 nm (P), which is the diameter of the PS spheres we used for the fabrication. The opening of the nanostructures (D) is set to be either 595 nm or 400 nm . At $D = 595\text{ nm}$, the opening of the nanostructure is close to the initial diameter of the PS sphere.

We use such condition to model BR with no etching performed. For 120 sec etched BR case, the opening diameter is measured from the SEM image and is approximately 400 nm. Hence $D = 400$ nm condition is used for to model the BR with etching time of 120 sec. The ZnO thickness t_1 was set at 100 nm, while the Ag hexagonal nanostructures thickness t_2 was set at 100 nm. The bottom bulk Ag thickness was set at 200 nm.

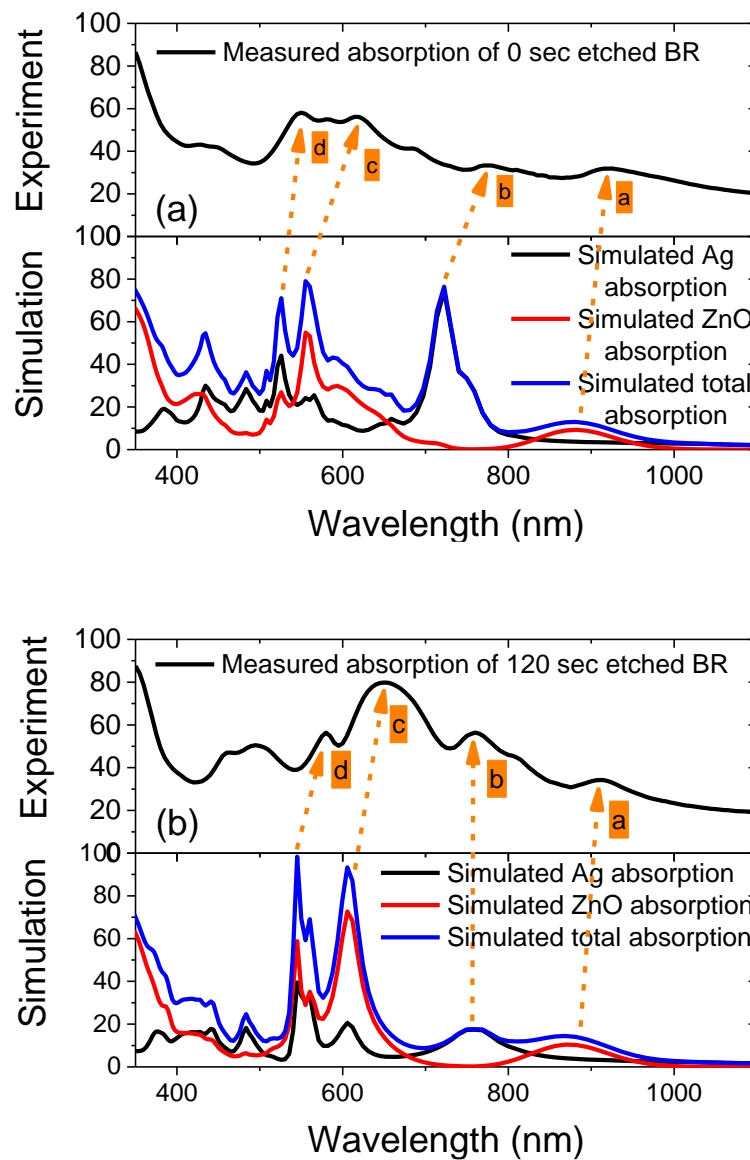


Figure 5.9: (a) 0 sec etched BR measured absorption (top) compared with simulated absorption under 595 nm opening ($D=595$ nm) simulation condition.

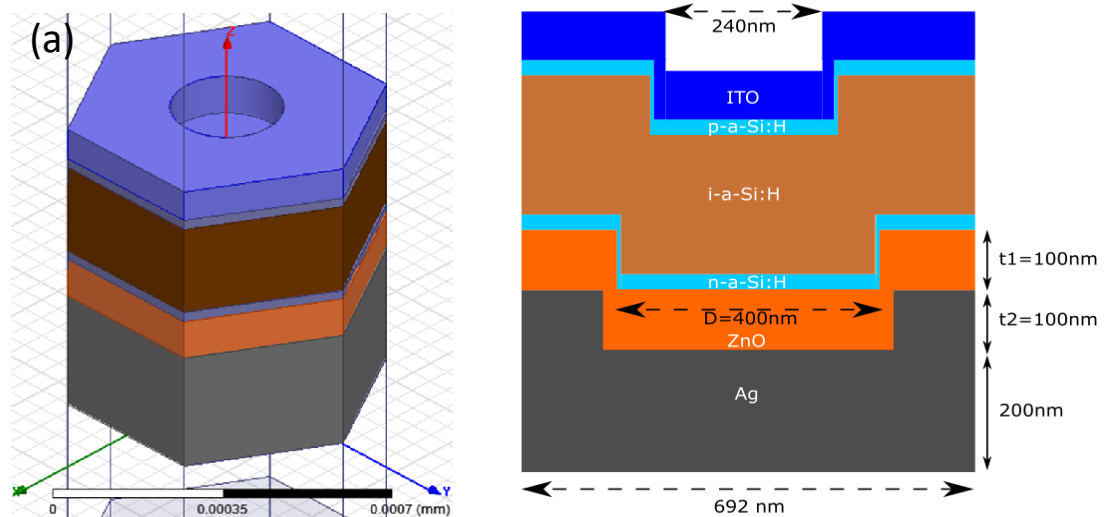
(b) 120 sec etched BR measured absorption (top) compared with simulated absorption under 400 nm opening ($D=400$ nm) simulation condition.

Fig.5.9 shows the comparison of the measured total reflectance of the 0 and 120 sec etched BRs and the corresponding simulated absorption of each layer. Other than the absorption of ZnO at its optical band gap around 360 nm, four distinctive absorption peaks (*a-d* highlighted in yellow) are observed in both the experimental and simulation results. The peak *a* in Fig.5.9 is attributed to the ZnO bulk absorption [251], while peak *b* is ascribed to the Ag plasmonic resonance absorption which shifts with the opening size. However this peak does contribute to overall BR absorption significantly. This may be due to the fact that in real devices, the semi-periodic nanostructures did not produce strong plasmonic effect as compared with the periodic simulation model. Peaks *c* and *d* near 500 – 600 nm are mainly ZnO absorption which is enhanced by the nanostructured Ag below [255]. A consistent red shift of the experimental results with respect to simulation results is observed. This might be due to the minor difference in ZnO film thickness between experiment device and the simulation model.

With the help of HFSS simulation, we managed to assign each of the optical losses in the periodical hexagonal nanostructured Ag/ZnO BR. Other than the rough Ag/ZnO interface absorption as modelled by BEMA method, ZnO absorption enhanced by the bottom Ag nanostructure also contributes significantly to the BR absorption. Surprisingly, Ag plasmonic absorption does not contribute significantly to overall BR absorption in the experiment results.

5.5 Experiments and simulation results of hexagonal Ag/ZnO back reflector solar cells

To investigate the potential parasitic losses from the BRs in solar cell devices as well as to understand different light scattering modes that appeared due to such nanostructures, 25 nm n-type amorphous silicon, 230 nm intrinsic amorphous silicon, 25 nm p-type amorphous silicon as well as 80 nm top ITO are added on top of the 400 nm opening BR. This model simulates the 120 sec O_2 plasma etched BR and its corresponding solar cell. Due to additional layers added in the model, parasitic losses will be introduced not only by the BRs, but also from ITO and the carriers recombination in highly n/p doped layers. Indeed, those layers will also absorb light but will not contribute to photo-current generation.



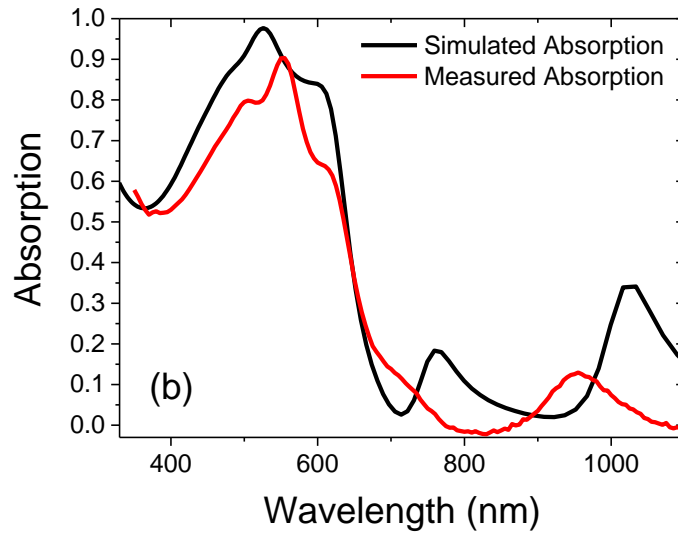


Figure 5.10: (a) HFSS simulation model for hexagonal BR solar cell; (b) Simulated and measured absorption of the flat Ag/ZnO BR solar cell.

Fig.5.10(a) shows the unit cell and the corresponding cross section of the simulation model of a hexagonal BR solar cell. The overall absorption and individual layers' absorption are simulated. To validate our simulation results, simulated overall absorption and measured absorption ($1 - \text{measured reflectance}$) of the flat Ag/ZnO BR solar cell device are plotted in Fig.5.10(b). We observe similar absorption trend between the simulation and experimental results. The experimental results are again slightly red shifted, due to difference in the film thickness (including ITO, ZnO and silicon thin films) between the actual cells and simulation model. Based on the validation results above, we conclude that the setting of simulation parameters can effectively represent the real device conditions. In next section, we will present the simulation results of hexagonal nanostructured Ag/ZnO BR solar cells.

5.5.1 Parasitic losses and absorption enhancement analysis

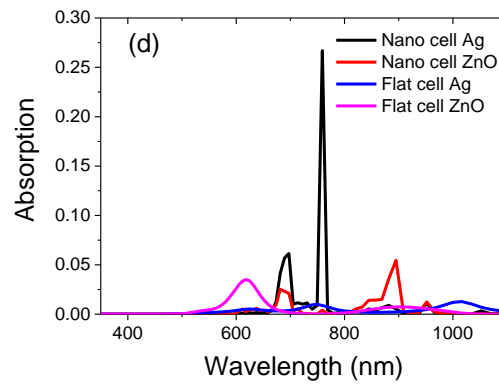
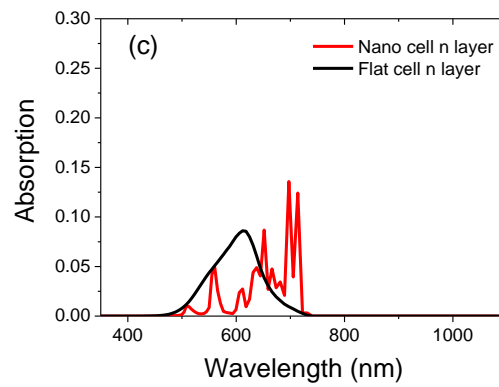
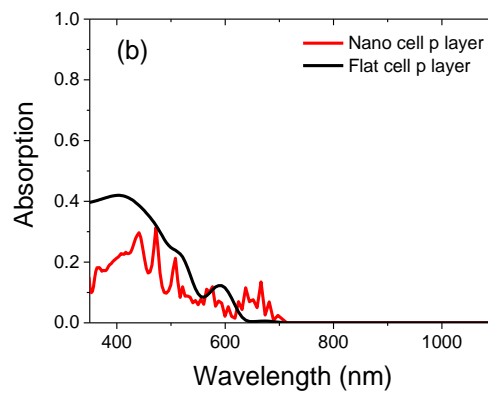
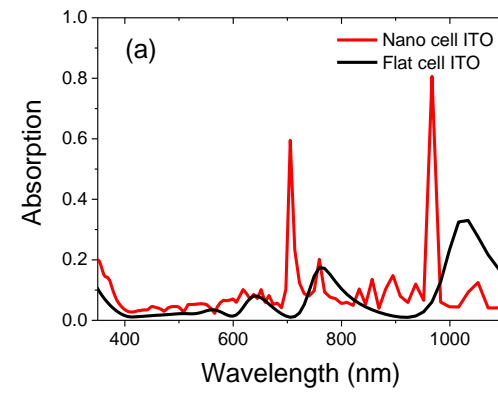


Figure 5.11: (a) ITO absorption; (b) p layer absorption; (c) n layer absorption; (d) Ag/ZnO BR absorption.

To analyze the parasitic losses in the different layers, the absorption enhancement in the intrinsic silicon layer, and the presence of light scattering mode, the base line for us to compare is the simulated flat device. Fig.5.11 (a-d) show the simulated ITO, p-type silicon, n-type silicon, and BR absorption for both flat and nanostructured solar cells. From the results we can see that after the solar cells are nanostructured, the absorption in ITO is greatly enhanced, the p layer absorption is reduced, while the n layer absorption is reduced from 500 to 650 nm but enhanced from 650 to 720 nm range. For the Ag and ZnO layers, our results show that for planar BR solar cell, the Ag almost does not absorb any light and a minimum absorption around 620 nm is observed for ZnO. For the nanostructured BR solar cell, ZnO absorption is reduced and red shifted to 690 nm. Two peaks at 700 and 760 nm are observed for Ag, which will contribute to parasitic absorption as well. These two peaks are mainly due to plasmonic absorption of the Ag. Unlike the above results where high absorption is observed for the BRs in air medium, when silicon active layers are deposited on top, BR parasitic absorption is less important as compared to the top ITO parasitic absorption.

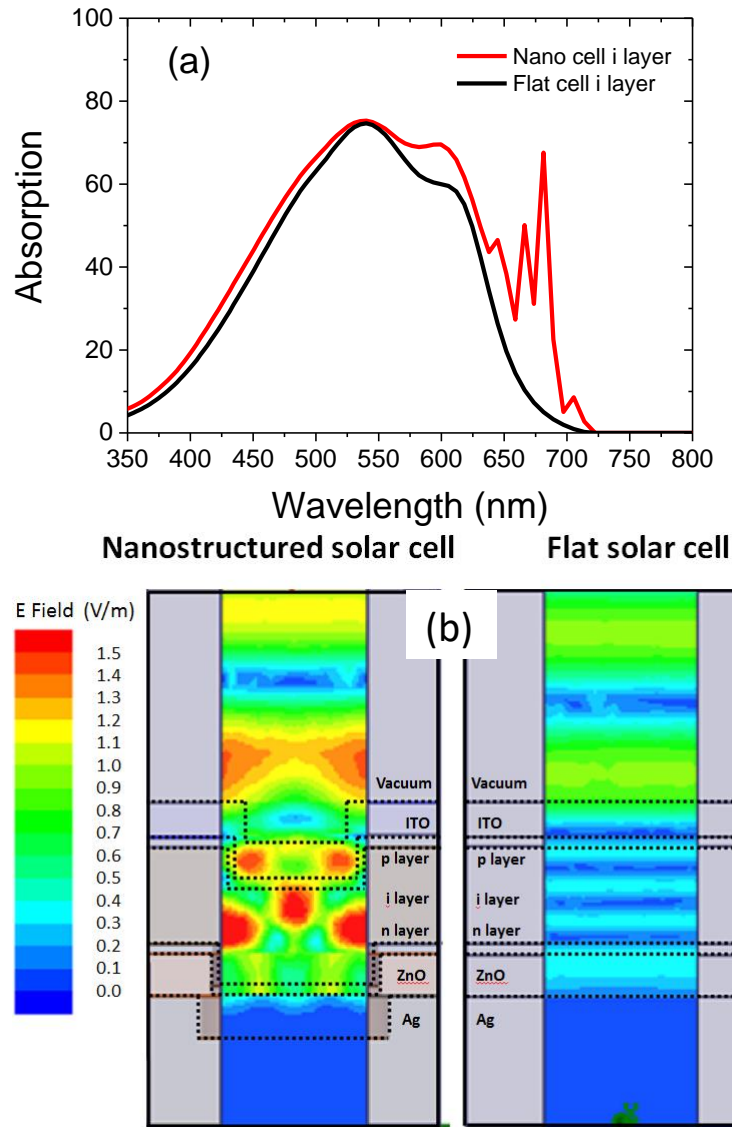


Figure 5.12: (a) Simulated intrinsic amorphous silicon absorption; (b) E field distribution of nanostructured and flat solar cell at 670 nm.

To study the absorption enhancement effect, intrinsic amorphous silicon absorption is plotted in Fig.5.12(a) for flat and nanostructured cases. We observe that the absorption in the intrinsic layer for the nanostructured solar cell is significantly enhanced not only for shorter wavelength range (350 – 520 nm) but also for longer wavelength range (550 – 720 nm). We use Eq (5.2) to determine the current density J_{sc} of the solar cell [256], where $I(\lambda)$ is the spectral irradiance of the standard AM1.5G solar spectrum, $A(\lambda)$ is the

absorption in the active absorber layer and $E(\lambda)$ is the corresponding photon energy. By using a band gap of $E_g = 1.71$ eV band gap of amorphous silicon and the AM1.5G solar spectrum, we calculated the generated J_{sc} of 18.3 mA/cm^2 and 15.0 mA/cm^2 for a nanostructured and flat solar cell respectively.

$$J_{sc} = \int_{300nm}^{1200nm} \frac{E_g I(\lambda) A(\lambda)}{E(\lambda)} d\lambda$$

To characterize the light resonance mode for the nanostructured solar cell, we selected 670 nm where a sharp absorption enhancement peak is observed in Fig.5.12(a) and we compared the electric field distribution in the nanostructured and flat solar cell. Fig.5.12(b) shows the electric field distribution at 670 nm incident wavelength. The light trapping effect of the nanostructured solar cell can be clearly see as multiple “hot spots” are induced. The generation of those “hot spots”, i.e. high electric field strength regions, is due to the localized light resonance modes in the nanostructures. Strong resonance modes are induced inside the intrinsic layer, resulting in greatly enhanced absorption.

5.5.2 Experiment results

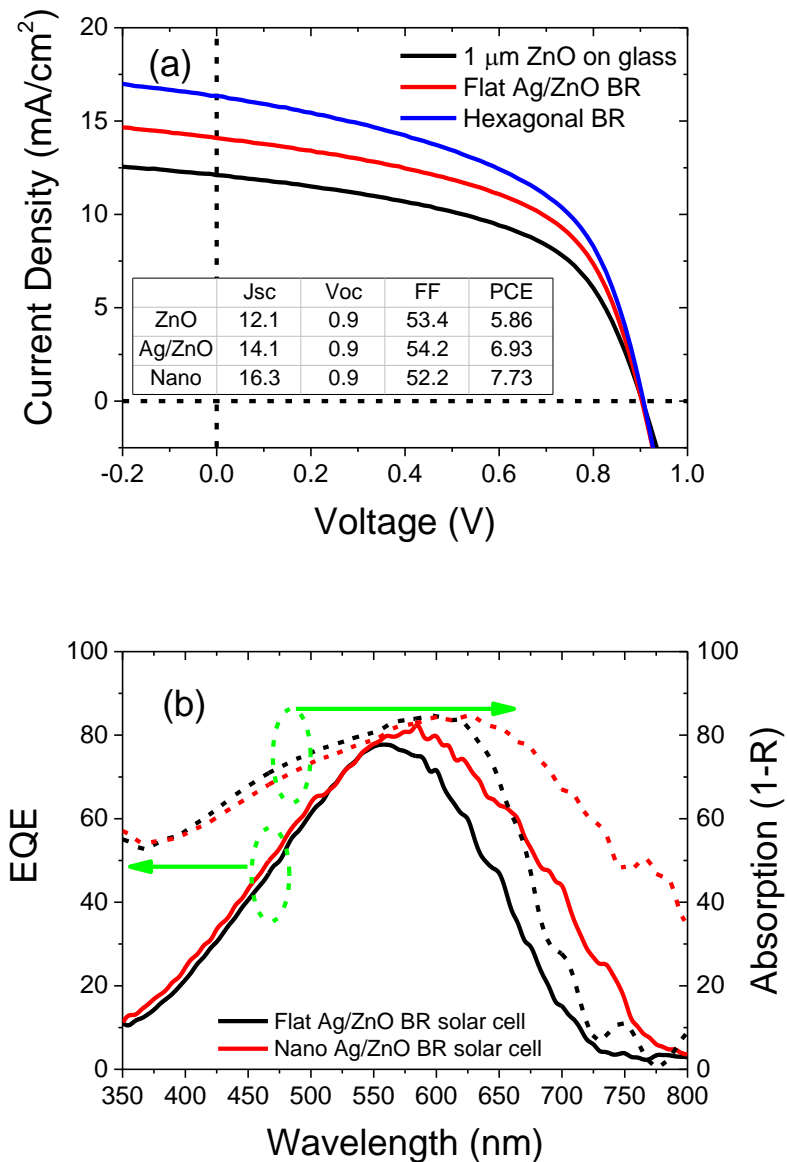


Figure 5.13: (a) J-V and solar cell parameters of different solar cells; (b) EQE and absorption ($1 - R_{total}$) of flat and nanostructured Ag/ZnO BR solar cells.

We fabricated solar cells using conventional 1 μm ZnO on glass substrates, Ag/ZnO flat BR substrates and hexagonal nanostructured Ag/ZnO BR substrates. The experimental results are compared and analyzed. Fig.5.13(a) shows the J - V characteristic and a summary of the photovoltaic parameters.

Fig.5.13(b) shows the EQE and optical absorption data ($1 - \text{total reflectance}$) of the flat Ag/ZnO BR and hexagonal nanostructured Ag/ZnO BR solar cell.

From Fig.5.13(a), we observe an increasing short-circuit current density of the three samples. With the incorporation of flat Ag/ZnO BR, 2.0 mA/cm^2 of current are gained compared to the transparent ZnO on glass substrate. Current collection is enhanced by 16.5 %. With the incorporation of hexagonally nanostructured Ag/ZnO BR, not only the open-circuit voltage is not compromised and also the short-circuit current is further enhanced by 2.2 mA/cm^2 . The total J_{sc} enhancement compared to the reference transparent flat ZnO substrate is as high as 34.7 %. Notably, for the flat Ag/ZnO BR substrate we find good agreement between the measured short-circuit current density and the simulated short-circuit current (6 % difference). However, our simulation predicted an 18.3 mA/cm^2 short-circuit current for the hexagonal nanostructured solar cell, while experimentally we only obtained 16.3 mA/cm^2 (10.9 % difference). Such difference is expected, as in our ideal simulation model, the structure is assumed to be periodic and strong resonances at specific wavelengths contribute significantly to the collected current. In our real devices, the resonance modes are broadened due to the semi-periodic arrangement of the nanostructures. Hence strong light trapping effects are observable at off resonance wavelength as well. Other than that, electrical resistivity, defects in the n/i interface, i/p interface, as well as bulk defect in intrinsic layer are not considered in the simulation model and besides, the internal quantum efficiency (IQE) is assumed to be 100% in the simulation. Hence a lower short circuit current in experiments for the hexagonal solar cell

is expected. Furthermore, the nanostructure solar cells have a larger contact area compared to the flat solar cells. Hence we would expect more interface defects, which leads to a larger difference for the nanostructured solar cell.

As for the EQE of the solar cell, we find good agreement with the simulated intrinsic silicon absorption. From 550 nm wavelength onwards, effective light trapping in our nanostructured BR solar cells can be observed. Also as we explained above, neither EQE nor absorption in our hexagonal nanostructured solar cell shows a strong resonance at specific wavelengths. Instead, a smooth and continuous light trapping effect from 550 nm to 750 nm is observed. By definition, the difference between the absorption and EQE is the parasitic absorption, assuming 100% IQE. With reference to the systematic parasitic loss analysis study by simulation in above sections, we identified that most of the parasitic losses at a wavelength range from 350 to 800 nm comes from ITO and the top p layer.

5.6 Conclusion

In this work, we demonstrated a novel hexagonal nanostructured design and fabrication process for light trapping in thin film amorphous silicon solar cells. The hexagonal nanostructured back reflectors and their corresponding solar cell were modeled by finite element method in simulation and verified with experimental data. The parasitic loss in the back reflector mainly comes from rough Ag/ZnO interface plasmonic absorption and enhanced ZnO absorption by Ag nanostructures. High frequency electromagnetic field simulator was proven to be an effective tool for modeling our hexagonal nanostructured back reflectors and solar cells. The simulation results show similar trend with the experimental data. From simulation, parasitic losses in our nanostructured solar cells mainly come from p doped layer and ITO top contact layer, and back reflector parasitic losses become less significant. The experimental and simulated ideal short-circuit currents are close to each other, with 6.0 % and 10.9 % difference for the flat and nanostructured solar cell respectively. Such difference is attributed to certain parameters that were not considered in the simulation, such as electrical resistivity, defects in the bulk and interfaces. Furthermore, our fabrication approach is not limited to a-Si:H silicon thin film solar cells, but can also be applied to μ c-Si:H or even c-Si:H silicon thin film solar cells. If the active material were silicon rather than hydrogenated amorphous silicon, we would expect that a thicker silicon active layer is not needed for an effective absorption, especially for the red-shifted absorption spectrum which normally will require a thicker active layer for a decent

absorption. Such application will further reduce the material cost and we would expect even lower solar power price.

As a low cost, robust and process compatible method, this nanostructured BR method is an effective candidate for improved light trapping performance of silicon thin film solar cells. Our simulation modeling method can be a powerful tool for any pre-fabrication design and optimization.

Chapter 6. Conclusion and future works

6.1 Conclusion

In this project, nanostructured silicon thin film solar cells have been fabricated, characterized and simulated. The etching behavior of polystyrene (PS) spheres under electron cyclotron resonance (ECR) generated oxygen plasmas have also been studied. Various nanostructured Ag/ZnO back reflectors (BRs) patterned by single or double PS sphere sizes have been fabricated and their optical performance has been characterized and correlated with the corresponding solar cell performance. Hexagonal nanostructured Ag/ZnO back reflectors and their corresponding nanostructured silicon thin film solar cells have been simulated and verified against experimental results. The parasitic losses in the device have been investigated.

In chapter three, the etching behavior of polystyrene (PS) spheres under electron cyclotron resonance (ECR) generated oxygen plasma has been studied. The PS spheres were melted and wet the silicon substrate under continuously applied high plasma power. This effect could be mitigated by reducing the plasma power, using plasma cycling mode, or by using a Faraday cage for ion shielding. We concluded that the energetic ion bombardment is the main reason for PS spheres heating and melting. A hexagonal shape was observed at the early stages of the etching process, regardless of the plasma conditions used. This is attributed to the shadowing

effect on oxygen radical diffusion. An oblate spheroidal shape was also observed from SEM side view images, presumably due to a higher vertical etching rate as compared to the side etching rate. We concluded that oxygen radicals are the main reason for PS spheres etching. By using a cycling etching mode and a lower plasma power, we successfully reduced the diameter of the PS spheres to less than 10 % of their original diameter. This was achieved without losing the patterning capability of the PS sphere arrays. By pushing the limit of the dimension of etched PS spheres relative to its original size, along with the added controllability on the periodicity and density of the PS spheres, various applications such as point contact solar cells can be realized.

In chapter four, we demonstrated a novel design and fabrication process for light trapping in amorphous silicon thin film solar cells. Both single and double sphere patterned BRs as well as corresponding solar cell devices were fabricated and tested. The double sphere patterned BR solar cells are proven to be more effective in light scattering, which lead to a better light trapping performance. As a result, a remarkable 8.79% power conversion efficiency (PCE) has been obtained for the 400 and 600 nm PS sphere mixture patterned BR solar cells. Without impacting the open-circuit voltage, the PS sphere patterned BR solar cells have shown an improved performance compared to the commercial ASAHI BR solar cells.

In chapter five, the hexagonal nanostructured back reflectors and their corresponding solar cell were modeled using a finite element method and

verified with experimental data. The parasitic loss in the back reflector mainly comes from plasmonic absorption at the rough Ag/ZnO interface and enhanced ZnO absorption by Ag nanostructures. A high frequency electromagnetic field simulator was proven to be an effective tool for modeling our hexagonal nanostructured back reflectors and solar cells. The simulation results have revealed similar trends as the experimental data. From the simulation study, it is discovered that the parasitic losses in our nanostructured solar cells mainly come from the p-type doped layer and ITO top contact layer, while BR parasitic losses are less significant. The experimental and simulated short-circuit current density are close to each other, with 6.0 % and 10.9 % difference for the flat and nanostructured solar cell respectively. Such difference is attributed to certain parameters that were not considered in the simulation, such as electrical resistivity, defects in the bulk and interfaces. Our simulation modeling method can be a powerful tool for any pre-fabrication design and optimization.

6.2 Recommendation for future research

There are several aspects of the present research work that could be further investigated.

6.2.1 Fabrication of nanostructured microcrystalline silicon thin film solar cell

In both chapter four and five, we have fabricated and simulated nanostructured silicon thin film solar cells based on hydrogenated silicon (a-

Si:H) material. However, our fabrication approach is not limited to a-Si:H thin film solar cells, but can also be applied to microcrystalline silicon ($\mu\text{c-Si:H}$) thin film solar cells. It is attractive due to two reasons. Firstly, the band gap of $\mu\text{c-Si:H}$ is similar to that of crystalline silicon (~ 1.1 eV) [257], which extends the absorption spectrum up to 1100 nm. Secondly, $\mu\text{c-Si:H}$ films are more stable under illumination than a-Si:H, as they suffer from lower light induced degradation [258]. Key challenges lie in controlling the film quality during the $\mu\text{c-Si:H}$ film growth, proposing different design for the BRs, as well as adjusting the PS sphere assisted lithography to achieve best performance for the $\mu\text{c-Si:H}$ solar cells. Due to the typical device thickness of around 1~2 μm for $\mu\text{c-Si:H}$ thin film solar cells, a larger inter nanostructure distance on the BRs is expected for the best light trapping performance. We can consider using a larger PS sphere (~ 1 μm) for the patterning of nanostructured BRs.

6.2.2 Fabrication of $\mu\text{c-Si:H/a-Si:H}$ tandem silicon thin film solar cell based on PS sphere assisted lithography and route to scale up

Since $\mu\text{c-Si:H}$ has about the same bandgap as crystalline silicon, which is ~ 1.12 eV, it can be combined with a-Si:H thin films, creating a layered, tandem cell. The top cell based on a-Si:H absorbs the visible light and leaves the infrared part of the spectrum for the bottom $\mu\text{c-Si:H}$ cell. Key challenges lie in optimizing the fabrication processes and conditions to achieve a good performing tandem silicon thin film solar cell. In terms of route to scale up for a successful integration of nano-structuring technique into the mass production favored roll-to-roll process, PS sphere assisted lithography might not be the best choice. However, PS sphere assisted lithography have the

potential to scale-up by applying Langmuir Blodgett system. But in terms of the roll-to-roll process, nano spray of the PS solution onto the substrate, formation of the single sphere packed thin aquatics film, followed by low temperature fast drying could be a solution.

6.2.3 Simulation optimization of the silicon thin film solar cell for the best performing fabrication parameter

In chapter 5, we presented simulation results of hexagonal nanostructured silicon thin film solar cells which were found to be consistent with the experimental results. The device optimization can be carried out, for example, by varying the device structure, film properties in the simulation etc. The corresponding experimental processes can be adjusted in accordance to the simulation parameters to achieve the best light trapping performance.

6.2.4 Nano-structuring technique by top down etching of silicon material

The silicon nano-hole structures based on top down etching can be fabricated with the help of PS sphere assisted lithography. Such devices can be achieved by firstly depositing n-type layer and intrinsic absorber layer on the substrate; secondly depositing protective Al nano-mesh layer using PS assisted lithography with oxygen plasma etching; thirdly, fluorine based plasma etching on the samples for nano-hole structures in intrinsic layers; last but not least, Al layer removal with KOH solution and p doped layer and transparent conductive oxide (TCO) deposition for the complete device formation. This is attractive because the nanostructure formation at the surface is independent of the nanostructure formed at the bottom of the cell.

Hence, we can have double side nanostructures for stronger light scattering properties within the active layer. Under the context of a tandem $\mu\text{c-Si:H/a-Si:H}$ solar cell, the combination of large nanostructures at the bottom (on the BRs) and small nano-holes at the surface, light trapping performance of double surface nanostructured device are expected to be better than single surface nanostructured device.

Reference

- [1] W. Cramer *et al.*, "Global response of terrestrial ecosystem structure and function to CO₂ and climate change: results from six dynamic global vegetation models," *Glob. Chang. Biol.*, vol. 7, no. 4, pp. 357–373, 2001.
- [2] BP, "Renewable energy - BP Statistical Review of World Energy 2017," *Bp*, vol. 66th, no. June, p. 11, 2017.
- [3] "BP: World Reserves of Fossil Fuels," 2017. [Online]. Available: <https://knoema.com/infographics/smsfgud/bp-world-reserves-of-fossil-fuels>.
- [4] "Research Opportunities and Challenges in the Energy Sector," in *Energy and Transportation : Challenges for the Chemical Sciences in the 21st Century*, Washington, D.C.: National Academies Press, 2003, p. 13.
- [5] B. M. French, S. P. Maran, and E. Chipman, "The Nature of the Sun," in *A meeting with the universe : science discoveries from the space program*, Washington, D.C. : National Aeronautics and Space Administration, 1981., 1981.
- [6] D. M. Chapin, C. S. Fuller, and G. L. Pearson, "A new silicon p-n junction photocell for converting solar radiation into electrical power [3]," *J. Appl. Phys.*, vol. 25, no. 5, pp. 676–677, 1954.
- [7] S. Xiao and S. Xu, "High-Efficiency Silicon Solar Cells—Materials and Devices Physics," *Crit. Rev. Solid State Mater. Sci.*, vol. 39, no. 4, pp. 277–317, 2014.
- [8] "PHOTOVOLTAICS REPORT," 2017. [Online]. Available: www.ise.fraunhofer.de.
- [9] BP, "Renewable energy - BP Statistical Review of World Energy 2017," *Bp*, vol. 66th, no. June, p. 11, 2017.
- [10] KANEKA CORPORATION, "New World Record Established for Conversion Efficiency in a Crystalline Silicon Solar Cell," 2017. [Online]. Available: <http://www.kaneka.co.jp/en/service/news/nr201708252/>.
- [11] M. A. Green *et al.*, "Solar cell efficiency tables (version 50)," *Prog. Photovoltaics Res. Appl.*, 2017.
- [12] REN21, *Renewables 2017: global status report*, vol. 72, no. October 2016. 2017.
- [13] M. A. Green, "Photovoltaics: Technology overview," *Energy Policy*, vol. 28, no. 14, pp. 989–998, 2000.
- [14] M. Izu and T. Ellison, "Roll-to-roll manufacturing of amorphous silicon alloy solar cells with in situ cell performance diagnostics," *Sol. Energy Mater. Sol. Cells*, vol. 78, no. 1–4, pp. 613–626, 2003.
- [15] V. E. Ferry, M. A. Verschuuren, H. B. T. Li, R. E. I. Schropp, H. A. Atwater, and A. Polman, "Improved red-response in thin film a-Si:H solar cells with soft-imprinted plasmonic back reflectors," *Appl. Phys.*

- Lett.*, vol. 95, no. 18, p. 183503, Nov. 2009.
- [16] Z. Ouyang, X. Zhao, S. Varlamov, Y. Tao, J. Wong, and S. Pillai, "Nanoparticle-enhanced light trapping in thin-film silicon solar cells," *Prog. Photovoltaics Res. Appl.*, vol. 19, no. 8, pp. 917–926, Dec. 2011.
 - [17] H. A. Atwater and A. Polman, "Plasmonics for improved photovoltaic devices," *Nat. Mater.*, vol. 9, no. 10, pp. 865–865, 2010.
 - [18] M. Stuckelberger, R. Biron, N. Wyrsh, F.-J. Haug, and C. Ballif, "Review : Progress in solar cells from hydrogenated amorphous silicon," *Renew. Sustain. Energy Rev.*, vol. 76, no. November, pp. 1–27, 2016.
 - [19] Y. H. Jang, Y. J. Jang, S. Kim, L. N. Quan, K. Chung, and D. H. Kim, "Plasmonic Solar Cells: From Rational Design to Mechanism Overview," *Chem. Rev.*, vol. 116, no. 24, pp. 14982–15034, 2016.
 - [20] V. E. Ferry, J. N. Munday, and H. A. Atwater, "Design considerations for plasmonic photovoltaics," *Adv. Mater.*, vol. 22, no. 43, pp. 4794–4808, 2010.
 - [21] X. Chen *et al.*, "Broadband enhancement in thin-film amorphous silicon solar cells enabled by nucleated silver nanoparticles," *Nano Lett.*, vol. 12, no. 5, pp. 2187–2192, 2012.
 - [22] G. Zhang and D. Wang, "Colloidal lithography - The art of nanochemical patterning," *Chemistry - An Asian Journal*. 2009.
 - [23] S. M. Yang, S. G. Jang, D. G. Choi, S. Kim, and H. K. Yu, "Nanomachining by colloidal lithography," *Small*. 2006.
 - [24] P. Colson, C. Henrist, and R. Cloots, "Nanosphere lithography: A powerful method for the controlled manufacturing of nanomaterials," *J. Nanomater.*, vol. 2013, 2013.
 - [25] D. Bratton, D. Yang, J. Dai, and C. K. Ober, "Recent progress in high resolution lithography," *Polym. Adv. Technol.*, 2006.
 - [26] T. Itani, W. Wakamiya, J. Cashmore, and M. Gower, "157-nm lithography with high numerical aperture lens for sub-70 nm node," in *Microelectronic Engineering*, 2003.
 - [27] M. J. Mendes, S. Morawiec, F. Simone, F. Priolo, and I. Crupi, "Colloidal plasmonic back reflectors for light trapping in solar cells," *Nanoscale*, vol. 6, no. 9, pp. 4796–4805, 2014.
 - [28] M. a. Green, "Third generation photovoltaics: Ultra-high conversion efficiency at low cost," *Prog. Photovoltaics Res. Appl.*, vol. 9, no. 2, pp. 123–135, 2001.
 - [29] S. Bowden and C. Honsberg., "No Title," *PVCDROM*, 2012. [Online]. Available: <http://pveducation.org/pvcdrom>.
 - [30] S. Bowden and C. Honsberg., "No Title," *PVCDROM*, 2012. .
 - [31] "PHOTOVOLTAICS REPORT," 2017. .
 - [32] T. Saga, "Advances in crystalline silicon solar cell technology for industrial mass production," *NPG Asia Mater.*, vol. 2, no. 3, pp. 96–102, 2010.
 - [33] K. Yoshikawa *et al.*, "Silicon heterojunction solar cell with interdigitated

- back contacts for a photoconversion efficiency over 26%," *Nat. Energy*, vol. 2, no. 5, 2017.
- [34] T. Dullweber *et al.*, "Towards 20% efficient large-area screen-printed rear-passivated silicon solar cells," in *Progress in Photovoltaics: Research and Applications*, 2012, vol. 20, no. 6, pp. 630–638.
 - [35] T. Mishima, M. Taguchi, H. Sakata, and E. Maruyama, "Development status of high-efficiency HIT solar cells," in *Solar Energy Materials and Solar Cells*, 2011, vol. 95, no. 1, pp. 18–21.
 - [36] C. Gong *et al.*, "Screen-printed aluminum-alloyed P+ emitter on high-efficiency N-type interdigitated back-contact silicon solar cells," *IEEE Electron Device Lett.*, vol. 31, no. 6, pp. 576–578, 2010.
 - [37] A. A. Al-Shouq and A. B. Gougam, "Review of interdigitated back contacted full heterojunction solar cell (IBC-SHJ): A simulation approach," in *3D Stacked Chips: From Emerging Processes to Heterogeneous Systems*, 2016.
 - [38] J. Zhao, A. Wang, and M. A. Green, "24.5% Efficiency silicon PERT cells on MCZ substrates and 24.7% efficiency PERL cells on FZ substrates," *Prog. Photovoltaics Res. Appl.*, 1999.
 - [39] A. Ur Rehman and S. H. Lee, "Advancements in n-type base crystalline silicon solar cells and their emergence in the photovoltaic industry," *The Scientific World Journal*. 2013.
 - [40] S. P. Group, "International Technology Roadmap for Photovoltaic—," *Itrpv*, no. March, pp. 1–37, 2013.
 - [41] O. a. Abdulrazzaq, V. Saini, S. Bourdo, E. Dervishi, and A. S. Biris, "Organic Solar Cells: A Review of Materials, Limitations, and Possibilities for Improvement," *Part. Sci. Technol.*, vol. 31, no. 5, pp. 427–442, 2013.
 - [42] T. Ameri, P. Khoram, J. Min, and C. J. Brabec, "Organic ternary solar cells: A review," *Adv. Mater.*, vol. 25, no. 31, pp. 4245–4266, 2013.
 - [43] M. C. Scharber and N. S. Sariciftci, "Efficiency of bulk-heterojunction organic solar cells," *Prog. Polym. Sci.*, vol. 38, no. 12, pp. 1929–1940, 2013.
 - [44] Y. Park, V. Choong, Y. Gao, B. R. Hsieh, and C. W. Tang, "Work function of indium tin oxide transparent conductor measured by photoelectron spectroscopy," *Appl. Phys. Lett.*, vol. 68, no. 19, pp. 2699–2701, 1996.
 - [45] M. C. Scharber and N. S. Sariciftci, "Efficiency of bulk-heterojunction organic solar cells," *Prog. Polym. Sci.*, vol. 38, no. 12, pp. 1929–1940, 2013.
 - [46] C. J. Brabec, N. S. Sariciftci, and J. C. Hummelen, "Plastic Solar Cells," *Adv. Funct. Mater.*, vol. 11, no. 1, pp. 15–26, 2001.
 - [47] K. Wang, C. Liu, T. Meng, C. Yi, and X. Gong, "Inverted organic photovoltaic cells," *Chem. Soc. Rev.*, vol. 45, no. 10, pp. 2937–2975, 2016.
 - [48] K. Wang, C. Liu, T. Meng, C. Yi, and X. Gong, "Inverted organic

- photovoltaic cells," *Chem. Soc. Rev.*, vol. 45, no. 10, pp. 2937–2975, 2016.
- [49] C. Wehrenfennig, G. E. Eperon, M. B. Johnston, H. J. Snaith, and L. M. Herz, "High charge carrier mobilities and lifetimes in organolead trihalide perovskites," *Adv. Mater.*, 2014.
 - [50] D. W. DeQuilettes *et al.*, "Impact of microstructure on local carrier lifetime in perovskite solar cells," *Science (80-.)*, 2015.
 - [51] S. D. Stranks *et al.*, "Electron-hole diffusion lengths exceeding 1 micrometer in an organometal trihalide perovskite absorber," *Science (80-.)*, 2013.
 - [52] Q. Dong *et al.*, "Electron-hole diffusion lengths > 175 μm in solution-grown $\text{CH}_3\text{NH}_3\text{PbI}_3$ single crystals," *Science (80-.)*, 2015.
 - [53] G. Xing *et al.*, "Long-range balanced electron-and hole-transport lengths in organic-inorganic $\text{CH}_3\text{NH}_3\text{PbI}_3$," *Science (80-.)*, 2013.
 - [54] L. Cai, L. Liang, J. Wu, B. Ding, L. Gao, and B. Fan, "Large area perovskite solar cell module," *J. Semicond.*, 2017.
 - [55] S. Yang, W. Fu, Z. Zhang, H. Chen, and C.-Z. Li, "Recent advances in perovskite solar cells: efficiency, stability and lead-free perovskite," *J. Mater. Chem. A*, vol. 5, no. 23, pp. 11462–11482, 2017.
 - [56] M. Wright and A. Uddin, "Organic-inorganic hybrid solar cells: A comparative review," *Sol. Energy Mater. Sol. Cells*, vol. 107, pp. 87–111, 2012.
 - [57] M. Wright and A. Uddin, "Organic-inorganic hybrid solar cells: A comparative review," *Sol. Energy Mater. Sol. Cells*, vol. 107, pp. 87–111, 2012.
 - [58] K. Sun *et al.*, "Review on application of PEDOTs and PEDOT:PSS in energy conversion and storage devices," *J. Mater. Sci. Mater. Electron.*, pp. 4438–4462, 2015.
 - [59] K. Sun *et al.*, "Review on application of PEDOTs and PEDOT:PSS in energy conversion and storage devices," *J. Mater. Sci. Mater. Electron.*, pp. 4438–4462, 2015.
 - [60] W. Shockley and H. J. Queisser, "Detailed balance limit of efficiency of p-n junction solar cells," *J. Appl. Phys.*, vol. 32, no. 3, pp. 510–519, 1961.
 - [61] R. Liu, S.-T. Lee, and B. Sun, "13.8% Efficiency Hybrid Si/Organic Heterojunction Solar Cells with MoO_3 Film as Antireflection and Inversion Induced Layer," *Adv. Mater.*, vol. 2, p. n/a-n/a, 2014.
 - [62] L. Hong *et al.*, "High efficiency silicon nanohole/organic heterojunction hybrid solar cell," *Appl. Phys. Lett.*, vol. 104, no. 5, 2014.
 - [63] M. Sharma, P. R. Pudasaini, F. Ruiz-Zepeda, D. Elam, and A. a Ayon, "Ultrathin, flexible organic-inorganic hybrid solar cells based on silicon nanowires and PEDOT:PSS," *ACS Appl. Mater. Interfaces*, vol. 6, no. 6, pp. 4356–63, 2014.
 - [64] S. Thiyaagu, C.-C. Hsueh, C.-T. Liu, H.-J. Syu, T.-C. Lin, and C.-F. Lin,

- “Hybrid organic-inorganic heterojunction solar cells with 12% efficiency by utilizing flexible film-silicon with a hierarchical surface,” *Nanoscale*, vol. 6, no. 6, pp. 3361–6, 2014.
- [65] M. Junghanns, J. Plentz, G. Andrä, A. Gawlik, I. Höger, and F. Falk, “PEDOT:PSS emitters on multicrystalline silicon thin-film absorbers for hybrid solar cells,” *Appl. Phys. Lett.*, vol. 106, no. 8, p. 083904, 2015.
 - [66] J. He *et al.*, “Realization of 13.6% Efficiency on 20 μm Thick Si/Organic Hybrid Heterojunction Solar Cells via Advance Nanotexturing and Surface Recombination Suppression,” *ACS Nano*, no. 6, pp. 6522–6531, 2015.
 - [67] M. Pietsch, S. Jäckle, and S. Christiansen, “Interface investigation of planar hybrid n-Si/PEDOT:PSS solar cells with open circuit voltages up to 645 mV and efficiencies of 12.6 %,” *Appl. Phys. A Mater. Sci. Process.*, vol. 115, no. 4, pp. 1109–1113, 2014.
 - [68] J. P. Thomas and K. T. Leung, “Defect-minimized PEDOT:PSS/planar-si solar cell with very high efficiency,” *Adv. Funct. Mater.*, vol. 24, no. 31, pp. 4978–4985, 2014.
 - [69] L. Hong, X. C. Wang, H. Y. Zheng, H. Wang, and H. Y. Yu, “Design Guidelines for Si (1 1 1) Inclined Nanohole Arrays in Thin-Film Solar Cells,” *IEEE Trans. Nanotechnol.*, vol. 13, no. 3, pp. 431–436, 2014.
 - [70] L. Hong *et al.*, “Optical absorption enhancement in a Si nanohole structure with hexagonal unit cell for solar cell application,” *Nanotechnology*, vol. 25, no. 41, p. 415303, 2014.
 - [71] L. Hong *et al.*, “Light trapping in hybrid nanopyramid and nanohole structure silicon solar cell beyond the Lambertian limit,” *J. Appl. Phys.*, vol. 116, no. 7, p. 074310, 2014.
 - [72] S. Jäckle *et al.*, “Junction formation and current transport mechanisms in hybrid n-Si/PEDOT:PSS solar cells,” *Sci. Rep.*, 2015.
 - [73] D. Zielke, A. Pazidis, F. Werner, and J. Schmidt, “Organic-silicon heterojunction solar cells on n-type silicon wafers: The BackPEDOT concept,” *Sol. Energy Mater. Sol. Cells*, 2014.
 - [74] D. Zielke, C. Niehaves, W. L??venich, A. Elschner, M. H??rteis, and J. Schmidt, “Organic-silicon Solar Cells Exceeding 20% Efficiency,” *Energy Procedia*, vol. 77, pp. 331–339, 2015.
 - [75] D. Zielke, C. Niehaves, W. L??venich, A. Elschner, M. H??rteis, and J. Schmidt, “Organic-silicon Solar Cells Exceeding 20% Efficiency,” *Energy Procedia*, vol. 77, pp. 331–339, 2015.
 - [76] L. He, C. Jiang, H. Wang, H. Lei, D. Lai, and Rusli, “11.3% efficient planar Si-PEDOT: PSS hybrid solar cell with a thin interfacial oxide,” in *Conference Record of the IEEE Photovoltaic Specialists Conference*, 2012, pp. 2785–2787.
 - [77] L. He, C. Jiang, H. Wang, D. Lai, and Rusli, “High efficiency planar Si/organic heterojunction hybrid solar cells,” *Appl. Phys. Lett.*, vol. 100, no. 7, pp. 6–9, 2012.
 - [78] J. Sheng *et al.*, “Improvement of the SiO_x Passivation Layer for High-

- Efficiency Si/PEDOT:PSS Heterojunction Solar Cells.," *ACS Appl. Mater. Interfaces*, vol. 6, no. 18, pp. 16027–34, 2014.
- [79] J. Sheng *et al.*, "Improvement of the SiO_x Passivation Layer for High-Efficiency Si/PEDOT:PSS Heterojunction Solar Cells.," *ACS Appl. Mater. Interfaces*, vol. 6, no. 18, pp. 16027–34, 2014.
- [80] J. Y. Chen, C. Con, M. H. Yu, B. Cui, and K. W. Sun, "Efficiency enhancement of PEDOT:PSS/Si hybrid solar cells by using nanostructured radial junction and antireflective surface," *ACS Appl. Mater. Interfaces*, vol. 5, no. 15, pp. 7552–7558, 2013.
- [81] R. C. Chittick, J. H. Alexander, and H. F. Sterling, "The Preparation and Properties of Amorphous Silicon," *J. Electrochem. Soc.*, 1969.
- [82] D. L. Carlson, D. E.; Wronski, C. R.; Pankove, J. I.; Zanzucchi, P. J.; Staebler, "Properties of amorphous silicon and a-Si solar cells," *RCA Rev.*, vol. 38, pp. 211–225, 1977.
- [83] A. Catalano, A. ; D'Aiello, R.V. ; Dresner, J. ; Faughnan, B. ; Firester, A. ; Kane, J. ; Schade, H. ; Schwartz, G. ; Smith, Z.E. ; Triano, "Attainment of 10% conversion efficiency in amorphous silicon solar cells," in *Proceedings of the 16th IEEE Photovoltaic Specialists Conference*, 1982, pp. 1421–1422.
- [84] D. L. Staebler and C. R. Wronski, "Reversible conductivity changes in discharge-produced amorphous Si," *Appl. Phys. Lett.*, 1977.
- [85] S. Vepřek and V. Mareček, "The preparation of thin layers of Ge and Si by chemical hydrogen plasma transport," *Solid. State. Electron.*, 1968.
- [86] S. Usui and M. Kikuchi, "Properties of heavily doped GDSi with low resistivity," *J. Non. Cryst. Solids*, vol. 34, no. 1, pp. 1–11, 1979.
- [87] J. Meier *et al.*, "On the Way Towards High Efficiency Thin Film Silicon Solar Cells by the 'Micromorph' Concept," *MRS Proc.*, 1996.
- [88] H. Sai, T. Matsui, and K. Matsubara, "Stabilized 14.0%-efficient triple-junction thin-film silicon solar cell," *Appl. Phys. Lett.*, vol. 109, no. 18, 2016.
- [89] B. Yan, G. Yue, L. Sivec, J. Yang, S. Guha, and C. S. Jiang, "Innovative dual function nc-SiO_x:H layer leading to a > 16 efficient multi-junction thin-film silicon solar cell," *Appl. Phys. Lett.*, vol. 99, no. 11, 2011.
- [90] D. H. Neuhaus and A. Münzer, "Industrial silicon wafer solar cells," *Adv. Optoelectron.*, vol. 2007, 2007.
- [91] Johannes Bernreuter, "EU PVSEC: New efficiency record of GCL-Si paves the way for black-silicon cells," 2017. [Online]. Available: <https://www.pv-tech.org/news/eu-pvsec-new-efficiency-record-of-gcl-si-paves-the-way-for-black-silicon-ce>.
- [92] X. Liu, P. R. Coxon, M. Peters, B. Hoex, J. M. Cole, and D. J. Fray, "Black silicon: fabrication methods, properties and solar energy applications," *Energy Environ. Sci.*, vol. 7, no. 10, pp. 3223–3263, 2014.
- [93] R. Bilyalov, L. Stalmans, and J. Poortmans, "Comparative Analysis of Chemically and Electrochemically Formed Porous Si Antireflection Coating for Solar Cells," *J. Electrochem. Soc.*, 2003.

- [94] Z. Huang, N. Geyer, P. Werner, J. De Boor, and U. Gösele, "Metal-assisted chemical etching of silicon: A review," *Adv. Mater.*, vol. 23, no. 2, pp. 285–308, 2011.
- [95] G. Fischer, E. Drahi, M. Foldyna, T. A. Germer, and E. V. Johnson, "Plasma nanotexturing of silicon surfaces for photovoltaics applications: influence of initial surface finish on the evolution of topographical and optical properties," *Opt. Express*, vol. 25, no. 24, pp. 1057–1071, 2017.
- [96] R. Dussart, T. Tillocher, P. Lefauchaux, and M. Boufnichel, "Plasma cryogenic etching of silicon: From the early days to today's advanced technologies," *Journal of Physics D: Applied Physics*. 2014.
- [97] X. Liu, P. R. Coxon, M. Peters, B. Hoex, J. M. Cole, and D. J. Fray, "Black silicon: fabrication methods, properties and solar energy applications," *Energy Environ. Sci.*, vol. 7, no. 10, pp. 3223–3263, 2014.
- [98] J. Oh, H.-C. Yuan, and H. M. Branz, "An 18.2%-efficient black-silicon solar cell achieved through control of carrier recombination in nanostructures," *Nat. Nanotechnol.*, vol. 7, no. September, pp. 743–748, 2012.
- [99] H.-P. Wang *et al.*, "Photon management in nanostructured solar cells," *J. Mater. Chem. C*, vol. 2, no. 17, p. 3144, 2014.
- [100] B. Hua, Q. Lin, Q. Zhang, and Z. Fan, "Efficient photon management with nanostructures for photovoltaics," *Nanoscale*, vol. 5, no. 15, pp. 6627–6640, 2013.
- [101] S. Misra, L. Yu, M. Foldyna, and P. Roca I Cabarrocas, "New approaches to improve the performance of thin-film radial junction solar cells built over silicon nanowire arrays," *IEEE J. Photovoltaics*, vol. 5, no. 1, pp. 40–45, 2015.
- [102] S. Misra, L. Yu, M. Foldyna, and P. Roca I Cabarrocas, "High efficiency and stable hydrogenated amorphous silicon radial junction solar cells built on VLS-grown silicon nanowires," *Sol. Energy Mater. Sol. Cells*, vol. 118, pp. 90–95, 2013.
- [103] A. S. Togonal *et al.*, "Core–Shell Heterojunction Solar Cells Based on Disordered Silicon Nanowire Arrays," *J. Phys. Chem. C*, vol. 120, no. 5, pp. 2962–2972, 2016.
- [104] L. Yu, B. O'Donnell, M. Foldyna, and P. Roca I Cabarrocas, "Radial junction amorphous silicon solar cells on PECVD-grown silicon nanowires," *Nanotechnology*, vol. 23, no. 19, 2012.
- [105] L. Yu *et al.*, "Assessing individual radial junction solar cells over millions on VLS-grown silicon nanowires," *Nanotechnology*, vol. 24, no. 27, 2013.
- [106] S. Misra, L. Yu, W. Chen, M. Foldyna, and P. Roca I Cabarrocas, "A review on plasma-assisted VLS synthesis of silicon nanowires and radial junction solar cells," *Journal of Physics D: Applied Physics*, vol. 47, no. 39. 2014.
- [107] L. Yu *et al.*, "Bismuth-catalyzed and doped silicon nanowires for one-pump-down fabrication of radial junction solar cells," *Nano Lett.*, vol. 12,

no. 8, pp. 4153–4158, 2012.

- [108] E. Garnett and P. Yang, “Light trapping in silicon nanowire solar cells,” *Nano Lett.*, vol. 10, no. 3, pp. 1082–1087, 2010.
- [109] M. Foldyna, A. S. Togonal, Rusli, and P. Roca i Cabarrocas, “Optimization and optical characterization of vertical nanowire arrays for core-shell structure solar cells,” *Sol. Energy Mater. Sol. Cells*, vol. 159, pp. 640–648, 2017.
- [110] O. L. Muskens, J. G. Rivas, R. E. Algra, E. P. a M. Bakkers, and A. Lagendijk, “Design of light scattering in nanowire materials for photovoltaic applications,” *Nano Lett.*, vol. 8, no. 9, pp. 2638–2642, 2008.
- [111] S. E. Han and G. Chen, “Optical absorption enhancement in silicon nanohole arrays for solar photovoltaics,” *Nano Lett.*, vol. 10, no. 3, pp. 1012–1015, 2010.
- [112] T. G. Chen *et al.*, “Characteristics of large-scale nanohole arrays for thin-silicon photovoltaics,” *Prog. Photovoltaics Res. Appl.*, vol. 22, no. 4, pp. 452–461, 2014.
- [113] S. Jeong, M. D. McGehee, and Y. Cui, “All-back-contact ultra-thin silicon nanocone solar cells with 13.7% power conversion efficiency,” *Nat. Commun.*, vol. 4, no. May, p. 2950, 2013.
- [114] Y. Cho, M. Gwon, H.-H. Park, J. Kim, and D.-W. Kim, “Wafer-scale nanoconical frustum array crystalline silicon solar cells: promising candidates for ultrathin device applications,” *Nanoscale*, vol. 6, pp. 9568–73, 2014.
- [115] H. Jeong *et al.*, “Enhanced light absorption of silicon nanotube arrays for organic/inorganic hybrid solar cells,” *Adv. Mater.*, vol. 26, pp. 3445–3450, 2014.
- [116] Q. Lin *et al.*, “Inverted nanocone-based thin film photovoltaics with omnidirectionally enhanced performance,” *ACS Nano*, vol. 8, no. 6, pp. 6484–6490, 2014.
- [117] A. Mavrokefalos, S. E. Han, S. Yerci, M. S. Branham, and G. Chen, “Efficient light trapping in inverted nanopyramid thin crystalline silicon membranes for solar cell applications,” *Nano Lett.*, vol. 12, pp. 2792–2796, 2012.
- [118] L. Li *et al.*, “Broadband optical absorption enhancement in silicon nanofunnel arrays for photovoltaic applications,” *Appl. Phys. Lett.*, vol. 100, no. 2012, pp. 3–7, 2012.
- [119] F. Toor, H. M. Branz, M. R. Page, K. M. Jones, and H. C. Yuan, “Multi-scale surface texture to improve blue response of nanoporous black silicon solar cells,” *Appl. Phys. Lett.*, vol. 99, no. 2011, pp. 2009–2012, 2011.
- [120] H. C. Yuan, V. E. Yost, M. R. Page, P. Stradins, D. L. Meier, and H. M. Branz, “Efficient black silicon solar cell with a density-graded nanoporous surface: Optical properties, performance limitations, and design rules,” *Appl. Phys. Lett.*, vol. 95, no. 2009, pp. 2–5, 2009.

- [121] D. A. R. Barkhouse, O. Gunawan, T. Gokmen, T. K. Todorov, and D. B. Mitzi, "Characteristics of large-scale nanohole arrays for thin-silicon photovoltaics," *Prog. Photovoltaics Res. Appl.*, vol. 22, no. October 2012, pp. 452–461, 2012.
- [122] J. Ji, H. Zhang, Y. Qiu, L. Wang, Y. Wang, and L. Hu, "Fabrication and photoelectrochemical properties of ordered Si nanohole arrays," *Appl. Surf. Sci.*, vol. 292, pp. 86–92, 2014.
- [123] D. Brodoceanu *et al.*, "Dense Arrays of Uniform Submicron Pores in Silicon and Their Applications," *ACS Appl. Mater. Interfaces*, vol. 7, no. 2, pp. 1160–1169, 2015.
- [124] J. Li *et al.*, "Si nanopillar array optimization on Si thin films for solar energy harvesting," *Appl. Phys. Lett.*, vol. 95, no. 3, 2009.
- [125] J. Li *et al.*, "Design guidelines of periodic Si nanowire arrays for solar cell application," *Appl. Phys. Lett.*, vol. 95, no. 24, pp. 2–5, 2009.
- [126] F. Wang, H. Yu, J. Li, X. Sun, X. Wang, and H. Zheng, "Textured-Silicon Thin Film for Photovoltaic Application," *Opt. Lett.*, vol. 35, no. 1, pp. 40–42, 2010.
- [127] J. Li, H. Yu, S. M. Wong, G. Zhang, G.-Q. Lo, and D.-L. Kwong, "Si nanocone array optimization on crystalline Si thin films for solar energy harvesting," *J. Phys. D: Appl. Phys.*, vol. 43, no. 25, p. 255101, 2010.
- [128] F. Wang *et al.*, "Design guideline of high efficiency crystalline Si thin film solar cell with nanohole array textured surface," *J. Appl. Phys.*, vol. 109, no. 8, 2011.
- [129] Y. Chen, W. Han, and F. Yang, "Enhanced optical absorption in nanohole-textured silicon thin-film solar cells with rear-located metal particles," *Opt. Lett.*, vol. 38, no. 19, pp. 3973–5, 2013.
- [130] X. Zhang, Y. Yu, J. Xi, T. Liu, and X.-H. Sun, "The plasmonic enhancement in silicon nanocone hole solar cells with back located metal particles," *J. Opt.*, vol. 17, no. 1, p. 015901, 2015.
- [131] Q. G. Du, C. H. Kam, H. V. Demir, H. Y. Yu, and X. W. Sun, "Enhanced optical absorption in nanopatterned silicon thin films with a nano-cone-hole structure for photovoltaic applications," *Opt. Lett.*, vol. 36, no. 9, pp. 1713–1715, 2011.
- [132] N. A. Yahaya, N. Yamada, Y. Kotaki, and T. Nakayama, "Characterization of light absorption in thin-film silicon with periodic nanohole arrays," *Opt. Express*, vol. 21, no. 5, pp. 5924–5930, 2013.
- [133] W. Wang, J. S. Zhang, Y. Zhang, Z. Xie, and G. G. Qin, "Optical absorption enhancement in submicrometre crystalline silicon films with nanotexturing arrays for solar photovoltaic applications," *J. Phys. D: Applied Phys.*, vol. 46, p. 6, 2013.
- [134] Z. Xie, W. Wang, L. X. Qin, W. J. Xu, and G. G. Qin, "Optical absorption characteristics of nanometer and submicron a-Si:H solar cells with two kinds of nano textures," *Opt. Express*, vol. 21, no. 15, pp. 18043–18052, 2013.
- [135] C. Lin and M. L. Povinelli, "Optical absorption enhancement in silicon

- nanowire arrays with a large lattice constant for photovoltaic applications,” *Opt. Express*, vol. 17, no. 22, pp. 19371–19381, 2009.
- [136] Z. Xiong, F. Zhao, J. Yang, and X. Hu, “Comparison of optical absorption in Si nanowire and nanoporous Si structures for photovoltaic applications,” *Appl. Phys. Lett.*, vol. 96, no. 18, 2010.
- [137] R. Y. Zhang, B. Shao, J. R. Dong, J. C. Zhang, and H. Yang, “Absorption enhancement analysis of crystalline Si thin film solar cells based on broadband antireflection nanocone grating,” *J. Appl. Phys.*, vol. 110, no. 11, 2011.
- [138] C. Il Yeo, Y. Min Song, S. Jun Jang, and Y. Tak Lee, “Optimal design of nano-scale surface light trapping structures for enhancing light absorption in thin film photovoltaics,” *J. Appl. Phys.*, vol. 114, no. 2, pp. 10–16, 2013.
- [139] P. Wangyang, Q. Wang, X. Wan, K. Hu, and K. Huang, “Optical absorption enhancement in silicon square nanohole and hybrid square nanowire-hole arrays for photovoltaic applications,” *Opt. Commun.*, vol. 294, pp. 377–383, 2013.
- [140] L. Hu and G. Chen, “Analysis of optical absorption in silicon nanowire arrays for photovoltaic applications,” *Nano Lett.*, vol. 7, no. 11, pp. 3249–3252, 2007.
- [141] O. Ozgun, R. Mittra, and M. Kuzuoglu, “General-Purpose Characteristic Basis Finite Element Method for Multi-Scale Electrostatic and Electromagnetic Problems,” *Electromagnetics*, vol. 30, no. 1–2, pp. 205–221, 2010.
- [142] “ANSYS HFSS,” 2014. [Online]. Available: <http://www.ansys.com/Products/Simulation+Technology/Electronics/Signal+Integrity/ANSYS+HFSS>.
- [143] J. M. Jin, *The Finite Element Method in Electromagnetics*. Wiley, 2014.
- [144] C. Haginoya, M. Ishibashi, and K. Koike, “Nanostructure array fabrication with a size-controllable natural lithography,” *Appl. Phys. Lett.*, vol. 71, no. 20, pp. 2934–2936, 1997.
- [145] L. Li, T. Zhai, H. Zeng, X. Fang, Y. Bando, and D. Golberg, “Polystyrene sphere-assisted one-dimensional nanostructure arrays: synthesis and applications,” *J. Mater. Chem.*, 2011.
- [146] X. Ye and L. Qi, “Two-dimensionally patterned nanostructures based on monolayer colloidal crystals: Controllable fabrication, assembly, and applications,” *Nano Today*. 2011.
- [147] J. Zhang, Y. Li, X. Zhang, and B. Yang, “Colloidal self-assembly meets nanofabrication: From two-dimensional colloidal crystals to nanostructure arrays,” *Advanced Materials*. 2010.
- [148] Y. Zhao *et al.*, “Metamaterial study of quasi-three-dimensional bowtie nanoantennas at visible wavelengths,” *Sci. Rep.*, vol. 7, p. 41966, Feb. 2017.
- [149] A. Plettl *et al.*, “Non-Close-Packed crystals from self-assembled polystyrene spheres by isotropic plasma etching: adding flexibility to

- colloid lithography," *Adv. Funct. Mater.*, vol. 19, no. 20, pp. 3279–3284, 2009.
- [150] D. F. Liu *et al.*, "Periodic ZnO nanorod arrays defined by polystyrene microsphere self-assembled monolayers," *Nano Lett.*, 2006.
 - [151] D. Leroose, M. Bechelany, L. Philippe, J. Michler, and S. Christiansen, "Ordered arrays of epitaxial silicon nanowires produced by nanosphere lithography and chemical vapor deposition," *J. Cryst. Growth*, 2010.
 - [152] K. Kempa *et al.*, "Photonic crystals based on periodic arrays of aligned carbon nanotubes," *Nano Lett.*, 2003.
 - [153] H. Wang, J. Wang, and Rusli, "Hybrid Si nanocones/PEDOT:PSS solar cell," *Nanoscale Res. Lett.*, 2015.
 - [154] W. Li, L. Xu, W. M. Zhao, P. Sun, X. F. Huang, and K. J. Chen, "Fabrication of large-scale periodic silicon nanopillar arrays for 2D nanomold using modified nanosphere lithography," *Appl. Surf. Sci.*, 2007.
 - [155] S. L. Cheng *et al.*, "Fabrication of size-tunable, periodic Si nanohole arrays by plasma modified nanosphere lithography and anisotropic wet etching," *Appl. Surf. Sci.*, 2012.
 - [156] S. Zhou *et al.*, "Wafer-Scale Integration of Inverted Nanopyramid Arrays for Advanced Light Trapping in Crystalline Silicon Thin Film Solar Cells," *Nanoscale Res. Lett.*, 2016.
 - [157] Y. Li *et al.*, "Periodic TiO₂ nanorod arrays with hexagonal nonclose-packed arrangements: excellent field emitters by parameter optimization," *Adv. Funct. Mater.*, 2009.
 - [158] W. Y. Fu, K. K. Y. Wong, and H. W. Choi, "Room temperature photonic crystal band-edge lasing from nanopillar array on GaN patterned by nanosphere lithography," in *Journal of Applied Physics*, 2010.
 - [159] Y. Li, T. Sasaki, Y. Shimizu, and N. Koshizaki, "Hexagonal-close-packed, hierarchical amorphous TiO₂ nanocolumn arrays: Transferability, enhanced photocatalytic activity, and superamphiphilicity without UV irradiation," *J. Am. Chem. Soc.*, 2008.
 - [160] H. L. Chen, S. Y. Chuang, C. H. Lin, Y. H. Lin, and S. Y. C. H. L. Chen^{1*} C. H. Lin², and Y. H. Lin¹, "Using colloidal lithography to fabricate and optimize sub-wavelength pyramidal and honeycomb structures in solar cells," *Opt. Soc. Am.*, 2007.
 - [161] J. Xiong, S. N. Das, B. Shin, J. P. Kar, J. H. Choi, and J. M. Myoung, "Biomimetic hierarchical ZnO structure with superhydrophobic and antireflective properties," *J. Colloid Interface Sci.*, 2010.
 - [162] C. H. Hsu *et al.*, "Low cost local contact opening by using polystyrene spheres spin-coating method for PERC solar cells," *Materials (Basel)*, 2016.
 - [163] C. W. Kuo, J. Y. Shiu, Y. H. Cho, and P. Chen, "Fabrication of large-area periodic nanopillar arrays for nanoimprint lithography using polymer colloid masks," *Advanced Materials*. 2003.

- [164] Y. Yu *et al.*, "Distorted colloidal arrays as designed template.," *Nanotechnology*, 2015.
- [165] F. F. Chen, *Introduction to Plasma Physics and Controlled Fusion*, no. 第 1 卷. Springer, 1984.
- [166] J. WANG, "Novel concepts in the PECVD of silicon thin films: from plasma chemistry to photovoltaic device applications," L'UNIVERSITE PARIS-SACLAY, 2017.
- [167] P. Bulkin, R. Brenot, B. Drévillon, and R. Vanderhaghen, "Structure and transport properties of integrated distributed electron cyclotron resonance grown micro-crystalline silicon," *J. Non. Cryst. Solids*, 1998.
- [168] P. Bulkin, N. Bertrand, and B. Drevillon, "Deposition of SiO₂ in integrated distributed electron cyclotron resonance microwave reactor," *Thin Solid Films*, 1997.
- [169] F. F. Chen, *Introduction to Plasma Physics and Controlled Fusion*, no. 第 1 卷. Springer, 1984.
- [170] S. Matsuo and M. Kiuchi, "Low temperature chemical vapor deposition method utilizing an electron cyclotron resonance plasma," *Jpn. J. Appl. Phys.*, 1983.
- [171] T. Unagami and T. Takeshita, "High-performance poly-Si TFTs with ECR-plasma hydrogen passivation," *IEEE Trans. Electron Devices*, vol. 36, no. 3, pp. 529–533, 1989.
- [172] W. Varhue, J. Burroughs, and W. Mlynko, "Electron cyclotron resonance plasma etching of photoresist at cryogenic temperatures," *J. Appl. Phys.*, 1992.
- [173] C. H. Hsu *et al.*, "Morphology control of silicon nanotips fabricated by electron cyclotron resonance plasma etching," *J. Vac. Sci. Technol. B Microelectron. Nanom. Struct.*, 2006.
- [174] T. Ohmori, M. Kashibe, S. Une, K. Yamamoto, D. Shiraishi, and S. Inoue, "Correlational Study between SiN Etch Rate and Plasma Impedance in Electron Cyclotron Resonance Plasma Etcher for Advanced Process Control," *IEEE Trans. Semicond. Manuf.*, 2015.
- [175] J. H. Xia, Rusli, S. F. Choy, R. Gopalakrishan, C. C. Tin, and J. Ahn, "The role of oxygen in electron cyclotron resonance etching of silicon carbide," *Microelectron. Eng.*, 2006.
- [176] A. Lacoste, T. Lagarde, S. B chu, Y. Arnal, and J. Pelletier, "Multi-dipolar plasmas for uniform processing: physics, design and performance," *Plasma Sources Sci. Technol.*, 2002.
- [177] S. Béchu *et al.*, "Multi-dipolar microwave plasmas and their application to negative ion production," *Phys. Plasmas*, 2013.
- [178] D. Daineka, P. Bulkin, G. Girard, J. E. Bouree, and B. Drevillon, "High density plasma enhanced chemical vapor deposition of optical thin films," *Eur. Phys. Journal-Applied Phys.*, 2004.
- [179] J. Chen *et al.*, "Controllable fabrication of 2D colloidal-crystal films with polystyrene nanospheres of various diameters by spin-coating," *Appl.*

Surf. Sci., 2013.

- [180] D. Nagao, R. Kameyama, Y. Kobayashi, and M. Konno, "Multiformity of particle arrays assembled with a simple dip-coating," *Colloids Surfaces A Physicochem. Eng. Asp.*, 2007.
- [181] R. Micheletto, H. Fukuda, and M. Ohtsu, "A Simple Method for the Production of a Two-Dimensional, Ordered Array of Small Latex Particles," *Langmuir*, 1995.
- [182] J. R. Oh, J. H. Moon, S. Yoon, C. R. Park, and Y. R. Do, "Fabrication of wafer-scale polystyrene photonic crystal multilayers via the layer-by-layer scooping transfer technique," *J. Mater. Chem.*, 2011.
- [183] Z. Yi, "Synthesis of One-Dimensional Silicon Nanopillar Arrays Assisted by Polystyrene Spheres," City University of Hong Kong, 2012.
- [184] J. Yu, Q. Yan, and D. Shen, "Co-self-assembly of binary colloidal crystals at the air - Water interface," *ACS Appl. Mater. Interfaces*, 2010.
- [185] N. Li *et al.*, "Fabrication of a resist pattern based on plasma-polystyrene interactions," *RSC Adv.*, vol. 6, no. 18, pp. 14948–14951, 2016.
- [186] S. Guruvenket, G. M. Rao, M. Komath, and A. M. Raichur, "Plasma surface modification of polystyrene and polyethylene," *Appl. Surf. Sci.*, vol. 236, no. 1, pp. 278–284, 2004.
- [187] C. Byeong-Ok, H. Sung-Wook, R. Jung-Hyun, and H. M. Sang, "More vertical etch profile using a Faraday cage in plasma etching," *Rev. Sci. Instrum.*, 1999.
- [188] T. Shikama, H. Kitaoka, and M. Hasuo, "Detection of electron energy distribution function anisotropy in a magnetized electron cyclotron resonance plasma by using a directional Langmuir probe," *Phys. Plasmas*, vol. 21, no. 7, 2014.
- [189] Y. Yu *et al.*, "Distorted colloidal arrays as designed template," *Nanotechnology*, vol. 26, no. 3, 2015.
- [190] G. Masmitja, P. Ortega, I. Martín, G. López, C. Voz, and R. Alcubilla, "IBC c-Si(n) Solar Cells Based on Laser Doping Processing for Selective Emitter and Base Contact Formation," in *Energy Procedia*, 2016.
- [191] Alexander Fridman, "Plasma Chemistry," Cambridge university press, 2008, p. 637.
- [192] F.-G. Hsieh, H.-Y. Xiao, J.-L. Lee, C.-H. Wang, P.-C. Tseng, "Size controllable sub-nanostructures on fluorescent polystyrene beads by plasma etching for 3D particle tracking and raman sensing in living cell," in *15th International Conference on Miniaturized Systems for Chemistry and Life Sciences 2011, MicroTAS 2011*, 2011, vol. 3, pp. 1767–1769.
- [193] V. E. Ferry, M. A. Verschuuren, H. B. T. Li, R. E. I. Schropp, H. A. Atwater, and A. Polman, "Improved red-response in thin film a-Si:H solar cells with soft-imprinted plasmonic back reflectors," *Appl. Phys. Lett.*, vol. 95, no. 18, p. 183503, Nov. 2009.
- [194] Z. Ouyang, X. Zhao, S. Varlamov, Y. Tao, J. Wong, and S. Pillai, "Nanoparticle-enhanced light trapping in thin-film silicon solar cells,"

- Prog. Photovoltaics Res. Appl.*, vol. 19, no. 8, pp. 917–926, Dec. 2011.
- [195] A. V Shah *et al.*, “Thin-film Silicon Solar Cell Technology,” *Photovolt Res. Appl.*, vol. 12, no. November 2003, pp. 113–142, 2004.
 - [196] M. Berginski *et al.*, “The effect of front ZnO:Al surface texture and optical transparency on efficient light trapping in silicon thin-film solar cells,” *J. Appl. Phys.*, vol. 101, no. 7, 2007.
 - [197] S. Pillai, K. R. Catchpole, T. Trupke, and M. A. Green, “Surface plasmon enhanced silicon solar cells,” *J. Appl. Phys.*, vol. 101, no. 9, 2007.
 - [198] K. R. Catchpole and A. Polman, “Design principles for particle plasmon enhanced solar cells,” *Appl. Phys. Lett.*, 2008.
 - [199] A. B. Roy, S. Das, and A. Kundu, “c-Si/n-ZnO-based flexible solar cells with silica nanoparticles as a light trapping metamaterial,” *Phys. Chem. Chem. Phys.*, vol. 19, pp. 12838–12844, 2017.
 - [200] O. Sanchez-Sobrado *et al.*, “Colloidal-lithographed TiO₂ photonic nanostructures for solar cell light trapping,” *J. Mater. Chem. C*, vol. 212, p. 140, 2017.
 - [201] A. Banerjee and S. Guha, “Study of back reflectors for amorphous silicon alloy solar cell application,” *J. Appl. Phys.*, vol. 69, no. 2, pp. 1030–1035, 1991.
 - [202] S. V Boriskina *et al.*, “Diffuse reflectors for improving light management in solar cells : a review and outlook,” *J. Opt.*, 2016.
 - [203] B. M. Curtin, “Photonic crystal back-reflectors for light management and enhanced absorption in a-Si : H solar cells by,” 2009.
 - [204] V. E. Ferry, L. A. Sweatlock, D. Pacifici, and H. A. Atwater, “Plasmonic nanostructure design for efficient light coupling into solar cells,” *Nano Lett.*, 2008.
 - [205] V. E. Ferry, M. A. Verschuuren, M. C. Van Lare, R. E. I. Schropp, H. A. Atwater, and A. Polman, “Optimized spatial correlations for broadband light trapping nanopatterns in high efficiency ultrathin film a-Si:H solar cells,” *Nano Lett.*, vol. 11, no. 10, pp. 4239–4245, 2011.
 - [206] V. E. Ferry, A. Polman, and H. A. Atwater, “Modeling light trapping in nanostructured solar cells,” *ACS Nano*, vol. 5, no. 12, pp. 10055–10064, 2011.
 - [207] M. Theuring *et al.*, “Comparison of Ag and SiO₂ Nanoparticles for Light Trapping Applications in Silicon Thin Film Solar Cells,” *J. Phys. Chem. Lett.*, vol. 5, no. 19, pp. 3302–3306, 2014.
 - [208] C. E. R. Disney, S. Pillai, C. M. Johnson, and M. A. Green, “Self-Assembled Nanostructured Rear Reflector Designs for Thin-Film Solar Cells,” *ACS Photonics*, vol. 2, no. 8, pp. 1108–1116, 2015.
 - [209] C. Van Lare, F. Lenzmann, M. A. Verschuuren, and A. Polman, “Dielectric Scattering Patterns for Efficient Light Trapping in Thin-Film Solar Cells,” *Nano Lett.*, vol. 15, no. 8, pp. 4846–4852, 2015.
 - [210] L. Van Dijk, J. Van De Groep, L. W. Veldhuizen, M. Di Vece, A. Polman,

- and R. E. I. Schropp, "Plasmonic Scattering Back Reflector for Light Trapping in Flat Nano-Crystalline Silicon Solar Cells," *ACS Photonics*, vol. 3, no. 4, pp. 685–691, 2016.
- [211] S. K. Ram *et al.*, "High-efficiency p–i–n superstrate amorphous Si solar cells on SiO_x periodic arrays of three-dimensional microstructure prepared by soft imprinting," 1882.
- [212] C. Niikura, A. Chowdhury, B. Janthong, P. Sichanugrist, and M. Konagai, "High-efficiency p–i–n superstrate amorphous Si solar cells on SiO_x periodic arrays of three-dimensional microstructure prepared by soft imprinting," *Appl. Phys. Express*, vol. 9, no. 4, p. 042301, Apr. 2016.
- [213] J. Springer, A. Poruba, L. Müllerova, M. Vanecek, O. Kluth, and B. Rech, "Absorption loss at nanorough silver back reflector of thin-film silicon solar cells," *J. Appl. Phys.*, vol. 95, no. 3, pp. 1427–1429, 2004.
- [214] Z. Ouyang, X. Zhao, S. Varlamov, Y. Tao, J. Wong, and S. Pillai, "Nanoparticle - enhanced light trapping in thin - film silicon solar cells," *Prog. Photovoltaics Res. Appl.*, 2011.
- [215] J. Kim, J. Wang, D. Daineka, and E. V. Johnson, "Improvement of near-infrared diffuse reflectance of silver back reflectors through Ag₂O formation by a UV-ozone exposure process," *Sol. Energy Mater. Sol. Cells*, vol. 170, no. May, pp. 114–119, 2017.
- [216] P. Spinelli *et al.*, "Plasmonic light trapping in thin-film Si solar cells," *J. Opt.*, vol. 14, no. 2, p. 024002, 2012.
- [217] S. Morawiec *et al.*, "Broadband photocurrent enhancement in a-Si:H solar cells with plasmonic back reflectors," *Opt. Express*, 2014.
- [218] S. Morawiec *et al.*, "Experimental quantification of useful and parasitic absorption of light in plasmon-enhanced thin silicon films for solar cells application.," *Sci. Rep.*, vol. 6, no. February, p. 22481, 2016.
- [219] R. A. Pala, J. White, E. Barnard, J. Liu, and M. L. Brongersma, "Design of plasmonic thin-film solar cells with broadband absorption enhancements," *Adv. Mater.*, vol. 21, no. 34, pp. 3504–3509, 2009.
- [220] M. A. Green and S. Pillai, "Harnessing plasmonics for solar cells," *Nat. Photonics*, vol. 6, no. 3, pp. 130–132, 2012.
- [221] P. Mandal and S. Sharma, "Progress in plasmonic solar cell efficiency improvement: A status review," *Renewable and Sustainable Energy Reviews*. 2016.
- [222] H. A. Atwater and A. Polman, "Plasmonics for improved photovoltaic devices," *Nat. Mater.*, vol. 9, no. 10, pp. 865–865, 2010.
- [223] S. Eustis and M. a el-Sayed, "Why gold nanoparticles are more precious than pretty gold: noble metal surface plasmon resonance and its enhancement of the radiative and nonradiative properties of nanocrystals of different shapes.," *Chem. Soc. Rev.*, vol. 35, no. 3, pp. 209–217, 2006.
- [224] M. Theuring *et al.*, "Comparison of Ag and SiO₂ Nanoparticles for Light Trapping Applications in Silicon Thin Film Solar Cells," *J. Phys. Chem.*

- Lett.*, vol. 5, no. 19, pp. 3302–3306, 2014.
- [225] D. M. Callahan, J. N. Munday, and H. A. Atwater, “Solar cell light trapping beyond the ray optic limit,” *Nano Lett.*, 2012.
 - [226] D. H. Lee, J. Y. Kwon, S. Maldonado, A. Tuteja, and A. Boukai, “Extreme light absorption by multiple plasmonic layers on upgraded metallurgical grade silicon solar cells,” *Nano Lett.*, vol. 14, no. 4, pp. 1961–1967, 2014.
 - [227] R. Khoury, Z. Li, P. Bulkin, Rusli, P. Roca I Cabarrocas, and E. V. Johnson, “Detailed study of electron cyclotron resonance oxygen plasma etching of polystyrene nanosphere arrays.”
 - [228] P. Roca i Cabarrocas, J. B. Chévrier, J. Huc, A. Lloret, J. Y. Parey, and J. P. M. Schmitt, “A fully automated hot-wall multiplasma-monochamber reactor for thin film deposition,” *J. Vac. Sci. Technol. A Vacuum, Surfaces, Film.*, vol. 9, no. 4, pp. 2331–2341, 1991.
 - [229] Abolmasov, S.N. *et al.*, “Substrate and p-layer effects on polymorphous silicon solar cells,” *EPJ Photovolt.*, vol. 5, p. 55206, 2014.
 - [230] K. H. Kim, S. Kasouit, E. V. Johnson, and P. Roca I Cabarrocas, “Substrate versus superstrate configuration for stable thin film silicon solar cells,” *Sol. Energy Mater. Sol. Cells*, vol. 119, pp. 124–128, Dec. 2013.
 - [231] D. Sainju, “Spectroscopic ellipsometry studies of Ag and ZnO thin films and their interfaces for thin film photovoltaics,” 2015.
 - [232] J. I. Owen, *Growth, Etching, and Stability of Sputtered ZnO:Al for Thin-Film Silicon Solar Cells*. Forschungszentrum Jülich.
 - [233] S. Morawiec *et al.*, “Experimental quantification of useful and parasitic absorption of light in plasmon-enhanced thin silicon films for solar cells application,” *Sci. Rep.*, vol. 6, no. February, p. 22481, 2016.
 - [234] M. J. Mendes, S. Morawiec, F. Simone, F. Priolo, and I. Crupi, “Colloidal plasmonic back reflectors for light trapping in solar cells,” *Nanoscale*, vol. 6, no. 9, pp. 4796–4805, 2014.
 - [235] V. E. Ferry, A. Polman, and H. A. Atwater, “Modeling light trapping in nanostructured solar cells,” *ACS Nano*, vol. 5, no. 12, pp. 10055–10064, 2011.
 - [236] L. R. Dahal, D. Sainju, N. J. Podraza, S. Marsillac, and R. W. Collins, “Real time spectroscopic ellipsometry of Ag/ZnO and Al/ZnO interfaces for back-reflectors in thin film Si:H photovoltaics,” *Thin Solid Films*, 2011.
 - [237] J. Müller, B. Rech, J. Springer, and M. Vanecek, “TCO and light trapping in silicon thin film solar cells,” *Sol. Energy*, 2004.
 - [238] B. P. Rand, J. Genoe, P. Heremans, and J. Poortmans, “Solar Cells Utilizing Small Molecular Weight Organic Semiconductors,” *Prog. Photovolt Res. Appl.*, vol. 15, no. February 2013, pp. 659–676, 2007.
 - [239] K. H. Kim, S. Kasouit, E. V. Johnson, and P. Roca I Cabarrocas, “Substrate versus superstrate configuration for stable thin film silicon solar cells,” *Sol. Energy Mater. Sol. Cells*, vol. 119, pp. 124–128, Dec.

2013.

- [240] J. Springer, A. Poruba, L. Müllerova, M. Vanecek, O. Kluth, and B. Rech, "Absorption loss at nanorough silver back reflector of thin-film silicon solar cells," *J. Appl. Phys.*, 2004.
- [241] F. J. Haug, T. Söderström, O. Cubero, V. Terrazzoni-Daudrix, and C. Ballif, "Plasmonic absorption in textured silver back reflectors of thin film solar cells," *J. Appl. Phys.*, 2008.
- [242] T. Koida, H. Fujiwara, and M. Kondo, "Reduction of optical loss in hydrogenated amorphous silicon/crystalline silicon heterojunction solar cells by high-mobility hydrogen-doped in ZnO transparent conductive oxide," *Appl. Phys. Express*, 2008.
- [243] R. Biron, C. Pahud, F. J. Haug, J. Escarré, K. Söderström, and C. Ballif, "Window layer with p doped silicon oxide for high V_{oc} thin-film silicon n-i-p solar cells," *J. Appl. Phys.*, 2011.
- [244] K. Nakada, S. Miyajima, and M. Konagai, "Application of n-type microcrystalline silicon oxide as back reflector of crystalline silicon heterojunction solar cells," *Jpn. J. Appl. Phys.*, 2015.
- [245] M. Zeman, O. Isabella, S. Solntsev, and K. Jäger, "Modelling of thin-film silicon solar cells," *Sol. Energy Mater. Sol. Cells*, 2013.
- [246] O. Isabella, S. Solntsev, D. Caratelli, and M. Zeman, "3-D optical modeling of thin-film silicon solar cells on diffraction gratings," *Prog. Photovoltaics Res. Appl.*, vol. 21, no. 1, pp. 94–108, 2013.
- [247] P. Roca i Cabarrocas, J. B. Chévrier, J. Huc, A. Lloret, J. Y. Parey, and J. P. M. Schmitt, "A fully automated hot-wall multiplasma-monochamber reactor for thin film deposition," *J. Vac. Sci. Technol. A Vacuum, Surfaces, Film.*, vol. 9, no. 4, pp. 2331–2341, 1991.
- [248] Abolmasov, S.N. *et al.*, "Substrate and p-layer effects on polymorphous silicon solar cells," *EPJ Photovolt.*, vol. 5, p. 55206, 2014.
- [249] E. S. Tüzemen, S. Eker, H. Kavak, and R. Esen, "Dependence of film thickness on the structural and optical properties of ZnO thin films," *Appl. Surf. Sci.*, 2009.
- [250] D. Sainju *et al.*, "Origin of optical losses in Ag/ZnO back-reflectors for thin film Si photovoltaics," in *Conference Record of the 2006 IEEE 4th World Conference on Photovoltaic Energy Conversion, WCPEC-4*, 2007, vol. 2, pp. 1732–1735.
- [251] J. I. Owen, *Growth, Etching, and Stability of Sputtered ZnO:Al for Thin-Film Silicon Solar Cells*. Forschungszentrum Jülich.
- [252] K. M. McPeak *et al.*, "Plasmonic films can easily be better: Rules and recipes," *ACS Photonics*, vol. 2, no. 3, pp. 326–333, 2015.
- [253] J. Wienke, B. van der Zanden, M. Tijssen, and M. Zeman, "Performance of spray-deposited ZnO:In layers as front electrodes in thin-film silicon solar cells," *Sol. Energy Mater. Sol. Cells*, 2008.
- [254] V. Jovanov *et al.*, "Influence of interface morphologies on amorphous silicon thin film solar cells prepared on randomly textured substrates," *Sol. Energy Mater. Sol. Cells*, vol. 112, pp. 182–189, 2013.

- [255] Y. H. Ko and J. S. Yu, "Optical absorption enhancement of embedded Ag nanoparticles with ZnO nanorod arrays," *Phys. status solidi*, vol. 208, no. 12, pp. 2778–2782, 2011.
- [256] T. Tiedje, E. Yablonovitch, G. D. Cody, and B. G. Brooks, "Limiting Efficiency of Silicon Solar Cells," *IEEE Trans. Electron Devices*, 1984.
- [257] A. V. Shah *et al.*, "Material and solar cell research in microcrystalline silicon," *Sol. Energy Mater. Sol. Cells*, 2003.
- [258] F. Finger, R. Carius, T. Dylla, S. Klein, S. Okur, and M. Günes, "Stability of microcrystalline silicon for thin film solar cell applications," *IEE Proc. - Circuits, Devices Syst.*, 2003.

Author's publications

Journal:

1. **Zeyu Li**, Rusli, Martin Foldyna, Junkang Wang, Wanghua Chen, Ari Bimo Prakoso, Chenjin Lu, Pere Roca i Cabarrocas, "Nanostructured back reflectors produced using polystyrene assisted lithography for enhanced light trapping in silicon thin film solar cells," *Sol. Energy*, vol. 167, no. March, pp. 108–115, 2018.
2. **Zeyu Li**, Rusli, Chenjin Lu, Ari Bimo Prakoso, Martin Foldyna, Rasha Khoury, Pavel Bulkin, Junkang Wang, Wanghua Chen, Erik Johnson, Pere Roca i Cabarrocas, "Optical Study and Experimental Realization of Nanostructured Back Reflectors with Reduced Parasitic Losses for Silicon Thin Film Solar Cells," *Nanomaterials*, vol. 8, no. 8, pp. 626, 2018.
3. Rasha Khoury, **Zeyu Li**, Pavel Bulkin, Rusli, Pere Roca i Cabarrocas, and Erik Johnson, "Detailed study of electron cyclotron resonance oxygen plasma etching of polystyrene nanosphere arrays," has submitted to Journal of Physics D: Applied Physics.
4. Ari Bimo Prakoso, Rusli, **Zeyu Li**, Chenjin Lu, and Changyun Jiang, "Design guideline for Si/organic hybrid solar cell with interdigitated back contact structure," *Semicond. Sci. Technol.*, vol. 33, no. 3, 2018.
5. Ari Bimo Prakoso, Chenjin Lu, **Zeyu Li**, Changyun Jiang, and Rusli, "High efficiency planar front junction n-Si/PEDOT:PSS hybrid solar cell with ARC compensated layer," has been submitted to Energy Technology.

6. Chenjin Lu, Rusli, Ari Bimo Prakoso, **Zeyu Li**, "Carrier Selective Solution-Deposited Molybdenum Oxide on n-type Crystalline Silicon Heterojunction Solar Cells," submitted to Journal of Photovoltaics.
7. Ari Bimo Prakoso, Lin Ke, Jianxiong Wang, **Zeyu Li**, Changyun Jiang, and Rusli, "Reverse recovery transient characteristic of PEDOT:PSS/n-Si hybrid organic-inorganic heterojunction," accepted 11 December 2016, Organic Electronics, vol. 42, pp. 269-274 (2017).
8. Nastiti Puspitosari, Christophe Longeaud, Raphael Lachaume, **Zeyu Li**, Rusli, and Pere Roca i Cabarrocas, "Comparison of FTPS Performed on Thin Films and Solar Cells," accepted 27 July 2017, Physica Status Solidi C: Current Topics in Solid State Physics, vol. 14, 1700165.

Conference:

1. **Li Zeyu**, Rusli, Ari Bimo Prakoso, Hong Lei and Pere Roca i Cabarrocas, "12.5% Silicon Nanohole/PEDOT:PSS hybrid solar cell with simple solution based surface treatment", 32nd European Photovoltaic Solar Energy Conference and Exhibition (EU PVSEC 2016), Germany, June 2016.
2. **Li Zeyu**, Rusli, Ari Bimo Prakoso and Pere Roca i Cabarrocas, "Si/PEDOT:PSS hybrid solar cell based on random Si nanowires in periodic Si nanoholes structure," Hybrid and Organic Photovoltaic 2016, Swansea, UK, June 2016.
3. **Li Zeyu**, Rusli, Lu Chenjin, Ari Bimo Prakoso, Martin Foldyna and Pere Roca i Cabarrocas, "Nanostructured Back Reflectors for a-Si:H Thin

Film Solar Cells by Polystyrene Sphere Assisted Lithography", Nano Science & Technology 2017, Fukuoka, Japan, Oct 2017. (invited)

4. Ari Bimo Prakoso, Lin Ke, Jianxiong Wang, **Zeyu Li**, Changyun Jiang, Rusli, "Study of PEDOT:PSS/n-Si hybrid organic-inorganic heterojunction", Materials Science-2017, Valencia, Spain, Sep 2017. (invited)